Stony Brook University

The official electronic file of this thesis or dissertation is maintained by the University Libraries on behalf of The Graduate School at Stony Brook University.

Quantum transport in ballistic graphene devices

A Dissertation Presented

by

Piranavan Kumaravadivel

to

The Graduate School

in Partial Fulfillment of the Requirements

for the Degree of

Doctor of Philosophy

in

Physics

Stony Brook University

December 2015

Stony Brook University

The Graduate School

Piranavan Kumaravadivel

We, the dissertation committee for the above candidate for the

Doctor of Philosophy degree, hereby recommend

acceptance of this dissertation.

Xu Du – Dissertation Adviser
Associate Professor, Department of Physics and Astronomy

Philip B. Allen – Chairperson of the defense
Professor, Department of Physics and Astronomy

Harold J. Metcalf – Committee member
Distinguished Teaching Professor, Department of Physics and Astronomy

Matthew Dawber– Committee member
Associate Professor, Department of Physics and Astronomy

Fernando E. Camino – External committee member
Staff scientist, Brookhaven National Laboratory

This dissertation is accepted by the Graduate School

Charles Taber
Dean of the Graduate School

Abstract of the Dissertation

Quantum transport in ballistic graphene devices

by

Piranavan Kumaravadivel

Doctor of Philosophy

in

Physics

Stony Brook University

2015

Graphene is a zero gap 2-D semiconductor having chiral charge carriers described by the massless relativistic Dirac-like Hamiltonian. In this thesis, unique transport properties that emerge from this energy spectrum are studied by using ballistic graphene and coupling its charge carriers with superconducting pair potentials and electrostatic gates.

Superconducting correlations can be induced in graphene by bringing it in contact with a superconductor. This superconducting proximity effect (PE) provides a way of exploring transport phenomena such as pseudo-diffusive behavior of ballistic carriers, specular Andreev reflections and unconventional quantum Hall effect with Andreev edge states. Hitherto, experimental realizations were limited by diffusive devices coupled to superconductors with low critical fields. In the first part of this work, in order to study these phenomena, we develop ballistic suspended graphene (G)-Niobium type–II superconductor(S) Josephson junctions. Our devices exhibit long mean free paths, small potential fluctuations near the charge neutrality point (CNP) and transparent SG interfaces that support ballistic supercurrents. In such a device, when the gate voltage is tuned very close to the CNP, unlike in diffusive junctions, we observe a strong density dependence of the multiple Andreev reflection features and normalized excess current. The observations qualitatively agree with a longstanding theoretical prediction for emergence of evanescent mode mediated pseudo diffusive transport. Next studying magneto-transport in these devices we find that PE is suppressed at very low fields even as the contacts remain superconducting. Further study reveals that distribution of vortices in the superconducting contacts affects the strength of the PE at the S-G interface.

The final part of the thesis searches for analogues of Klein tunneling in ballistic graphene by studying charge transport through an electrostatically created potential barrier. To this end, different device fabrication methods are developed to create ballistic heterojunctions on suspended graphene and graphene on hexagonal boron nitride using contactless 'air' local gates.

To my parents….

Table of Contents

List of Figures

Acknowledgements

First and foremost, I would like to thank my advisor, Xu Du, for his advice, support and guidance throughout the past five years. Being one of his first students, I had the great fortune to learn directly from him many of the skills that were essential in developing this thesis. Working with him in setting up the lab, building, maintaining and troubleshooting equipment was a valuable experience. Thank you for listening to my ideas, opinions and concerns with patience and for motivating me to push forward during troubled times.

I would also like to thank my committee members for their time and effort in reviewing my work and faculty members of the department who supported me at various junctures in this journey. I owe special thanks to professors Matthew Dawber, Marivi Fernandez Serra, Harold Metcalf, Philip Allen, Kostya Likharev, Dmitri Kharzeev and Laszlo Mihaly.

I had some wonderful time working with my group members Fen, Humed, Heli, Yan, Peter, Naomi, Mike, Sid and Rick. Thank you all for the unforgettable memories and providing a lively working environment. Bent Nielson has been a constant source of support from the time I joined the lab. His knowledge of the resources in the department has been invaluable. And when assistance was hard to find, he was always there to lend a hand. Thanks Bent for all your help.

I would like to acknowledge the support provided by the machine shop for their assistance in building some of the equipment used in this work and the departmental staff, especially, Sara and Pernille for their assistance in administrative matters and paperwork.

I had the good fortune to make some new friends and meet some great people at Stony Brook. Thank you all for making my life at Stony Brook an enjoyable and worthwhile experience.

Finally I would like to thank my parents: Kumaravadivel (Appa) and Rajini (Amma) and my brothers, Guruparan and Niruththan. Needless to say, without their love, support and understanding this journey would have been difficult.

Chapter 1

Introduction

1.1. Overview and outline of the thesis

Research in graphene has broadened in scope since the first experiments were reported in 2004-5[1, 2]. There is now a great interest in graphene optoelectronics[3] and plasmonics. Together with electronic properties, the thermal and mechanical properties of graphene have inspired possibilities for diverse applications ranging from mobile phones, energy storage[4, 5] to cancer treatment[6] and bio sensing[7]. Despite all this commercial prowess, the appeal of this material, for me, is its relatively simple structure and the capability it provides in studying relativistic quantum phenomena in benchtop experiments. So as a graduate student starting research in 2010 (coincidently the year in which the Nobel prize was awarded for the discovery of graphene) my natural choice was to work on projects that directly probe the fundamental properties of the Dirac fermions in graphene.

Unlike semiconductor 2D electron gas systems (2DEGs) and other Dirac materials, the massless Dirac charge carriers in graphene are easily accessible to experiments. It is convenient to tune graphene's carrier density and switch the carrier type by designing electrostatic gate potentials. The electrons in graphene can also be directly coupled to a wide range of materials, from metals to layered semiconductors [8-10]. But to study the intrinsic electronic properties arising from its gapless relativistic-like spectrum requires disorder-free samples with low energy fluctuations. One of the major steps in achieving this is by suspending graphene and relieving it from the coarse substrate (silicon dioxide) that it sits on[11, 12]. Still, maintaining these qualities while coupling it to various materials and electrostatic potentials, is technically challenging. The very fact of the ease in accessibility of the electrons also makes it vulnerable to even the slightest of extrinsic charges and impurities.

This theses work is on overcoming these challenges to study ballistic quantum transport of Dirac fermions in graphene when 1) in contact with a superconductor and 2) under the influence of engineered electrostatic barriers. In both these cases the process that reveals the interesting physics involves electron-hole conversion. In the first case, the conversion occurs when scattering from a superconducting pair potential and in the second case, the conversion occurs during head on collisions on repulsive electrostatic barriers. In graphene the electron hole symmetry and chirality makes these processes unique compared to those in normal metals and semiconductors.

Coupling two types of electron systems – the relativistic charge carriers in graphene with strongly interacting Cooper pair condensates in a superconductor provides opportunities to test various longstanding phenomena such as specular Andreev reflection[13], pseudo-diffusive dynamics of ballistic carriers[14, 15] and to study graphene's anomalous quantum Hall effects infused with superconducting correlations[16, 17]. Chapters 2 and 3 focus on work on these topics using graphene with transparent superconducting contacts. Chapter 2 presents a brief theoretical overview of the superconducting proximity effect (and Andreev reflection processes), the mechanism by which superconducting correlations are infused in graphene (and other normal metals) from the superconducting leads. The unique Andreev reflection processes in graphene especially near the Dirac point are highlighted. The rest of the chapter discusses the fabrication of ballistic suspended graphene- type II superconductor devices with transparent interfaces. Even though diffusive graphene-superconductor devices were studied almost six years ago [18-21], the fabrication of ballistic superconductor junctions have remained challenging. The procedures employed to free graphene from disorder posed challenges to the transparency of the superconductor-graphene interface. Effectively combating such challenges culminated in the development of the fabrication procedure described in the chapter. This is a crucial part of the work that made possible the experiment presented in chapter 3 and potentially can form the basis for many interesting studies in the future.

Chapter 3 of the thesis discusses work based on ballistic suspended graphene Niobium superconductor devices. Here we explore intrinsic transport near graphene's charge neutrality point where carrier density almost vanishes. Inducing superconducting correlations in ballistic graphene, we demonstrate evidence for transition from ballistic, propagating mode transport at high carrier densities to pseudo-diffusive, evanescent mode transport at low carrier densities (near

the neutrality point). Also we probe inter-band (specular) Andreev reflections i.e., superconductor induced reflection processes that couple electrons and holes from the conduction and valence band of the Dirac cone.

Type II superconductors with a transparent interface on ballistic graphene provides the opportunity to study induced superconductivity in the quantum hall regime (Andreev edge states). But, intriguingly, even as the superconductor retains its properties to very high fields, the expected evidence for Andreev edge states in graphene[22] is lacking[23, 24]. The devices studied in this thesis work also show similar results. In Chapter 4 we explore this issue by performing low field magneto-transport measurements in superconducting NbN- graphene junctions. By changing the way the magnetic field penetrates the superconductor, we reveal that the vortex screening currents in the superconducting NbN affect the Andreev reflection probability at the graphene-superconductor interface. According to our present understanding this suppression is significant when a reduced superconducting gap is present at the interface.

Chapter 5 of this thesis deals with the subject of transmission of massless Dirac particles through potential barriers. Charge carriers governed by non-relativistic quantum mechanics, when incident on a potential barrier, have a small probability of tunneling through. But the massless Dirac-like quasiparticles of graphene have perfect transmission at normal incidence[25], a property that has parallels to the Klein tunneling of spin ½ particles described by quantum electrodynamics[26]. In graphene this is a consequence of conversation of pseudospin – a quantity arising from the sub-lattice symmetry in graphene. The perfect transmission at normal incidence through electrostatic barriers can be used to collimate randomly oriented electron trajectories and guide them in a desired direction. Sharper potentials can also be used in negative index of refraction experiments [27, 28]. The first part of chapter 5 presents a brief theoretical overview of Klein tunneling and discusses previous experimental work on the subject. The rest of the chapter is dedicated to the fabrication procedures and preliminary experiments that attempt to study Klein tunneling in suspended graphene and hexagonal boron nitride (h-BN) supported graphene devices with contactless local top gates. Contactless top gates are like bridges that cross over the (suspended) graphene and are used to create the local electrostatic barrier. The h-BN supported graphene devices are known to display almost the same ballistic properties as suspended graphene devices and have no size limitations[29]. Therefore they are ideal for these electron collimation

experiments. The chapter also includes details of the transfer setup and procedure that was developed to make the h-BN supported graphene devices.

In the rest of this chapter I provide a brief overview of the theoretical aspects of graphene and its transport properties. The intention is to provide some background relevant to the experiments discussed in chapters 3, 4 and 5. Further details on the topics discussed in this chapter and in the beginning of chapter 2 can be found in a number of review papers [30-33].

1.2. Theoretical overview of the properties of graphene

1.2.1. The band structure of graphene using the tight binding approximation

Graphene is a single sheet of identical carbon atoms arranged periodically to form a two-dimensional hexagonal lattice structure. Each carbon atom with four valence orbitals forms two kinds of bonds with their three nearest neighbors. One is the strong in-plane σ bonds formed by sp^2 hybridization of the s, p_x and p_y electron orbitals. The other is the π-bond formed by nearest neighbor covalent bonding of the delocalized p_z orbitals. The σ bonds are responsible for the strength and stability of graphene whereas the π bonds govern the unique low energy electronic properties of graphene. The honeycomb lattice by itself is not a Bravais lattice but can be visualized as two part triangular Bravais sub-lattices, labelled A (red) and B (blue) in figure 1.1. Each carbon atom in one sub-lattice is surrounded by indistinguishable carbon atoms from the other. This symmetry, as we will see later, has interesting implications to the dynamics of charge carriers in graphene.
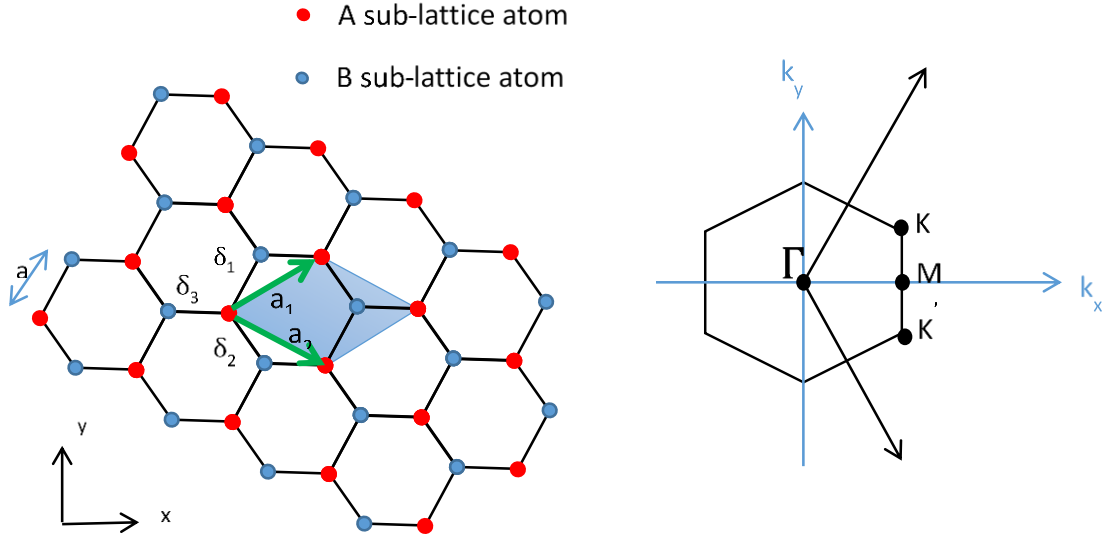
Figure 1.1: Atomic structure of graphene. (left) Hexagonal lattice graphene showing the two sub lattices A and B. (right) First Brillouin zone with the symmetry points Γ, M, K (and K').

The unit vectors of one of the Bravais lattices (sub lattice A in figure 1.1) and the corresponding reciprocal lattice vectors can be written as,

$$\vec{a}_1 = \frac{a}{2}\left(3, \sqrt{3}\right) \quad \text{and} \quad \vec{a}_2 = \frac{a}{2}\left(3, -\sqrt{3},\right) \tag{1.1a}$$

$$\vec{b}_1 = \frac{2\pi}{3a}\left(3, \sqrt{3}\right) \quad \text{and} \quad \vec{b}_2 = \frac{2\pi}{3a}\left(3, -\sqrt{3}\right) \tag{1.1b}$$

and the vectors to the nearest neighbor (B sub-lattice) atoms are given by,

$$\vec{\delta}_1 = \frac{a}{2}\left(1, \sqrt{3}\right), \qquad \vec{\delta}_2 = \frac{a}{2}\left(1, -\sqrt{3}\right) \qquad \vec{\delta}_3 = -a\left(1, 0\right) \tag{1.2}$$

Here a=1.46A^0 –is the lattice separation. The first Brillouin zone is hexagonal and is shown in figure (1.1(b)). Γ, K and M represent the high symmetry points. Although there are six K-points corresponding to the six corners of the Brillouin zone only two are inequivalent. The others are displaced by reciprocal lattice vectors. The two distinct K points, commonly labelled K and K',

are called *'valleys' or 'Dirac points (DPs)'*. This is because of their unique position in graphene's linear energy spectrum. The coordinates in reciprocal space for the two valleys are

$$\vec{K} = \left(\frac{2\pi}{3a}, \frac{2\pi}{3\sqrt{3}a} \right) , \vec{K}' = \left(\frac{2\pi}{3a}, -\frac{2\pi}{3\sqrt{3}a} \right) \tag{1.3}$$

The covalent bonding of the π-orbitals is sufficiently strong to use the tight binding approach for evaluating graphene's energy spectrum. The nearest neighbor tight binding Hamiltonian, in the basis of the π orbital wave functions Ψ_A, Ψ_B of sub lattices A and B, is given by

$$\hat{H} = t \begin{pmatrix} 0 & \sum_j e^{i\vec{k}.\vec{\delta}_j} \\ \sum_j e^{-i\vec{k}.\vec{\delta}_j} & 0 \end{pmatrix}, \text{ where } j=1, 2 \text{ and } 3. \tag{1.4}$$

Here $t \sim 3eV$ is the nearest neighbor hopping parameter. The eigenvalues of the Hamiltonian is given by,

$$E_{\pm}(\vec{k}) = \pm t \sqrt{1 + 4\cos\left(\frac{3ak_x}{2}\right)\cos\left(\frac{\sqrt{3}ak_y}{2}\right) + 4\cos^2\left(\frac{\sqrt{3}a}{2}k_y\right)} \tag{1.5}$$

and the plot of the band structure is shown in figure 1.2. It can be seen that the above energy spectrum is electron-hole symmetric very close to the two K points with vanishing energies: $E(\vec{K}) = E(\vec{K}') = 0$. This degeneracy is robust due to time reversal and C$_3$ symmetry of the lattice. Breaking this symmetry requires a periodic potential that acts on the sub lattice space.
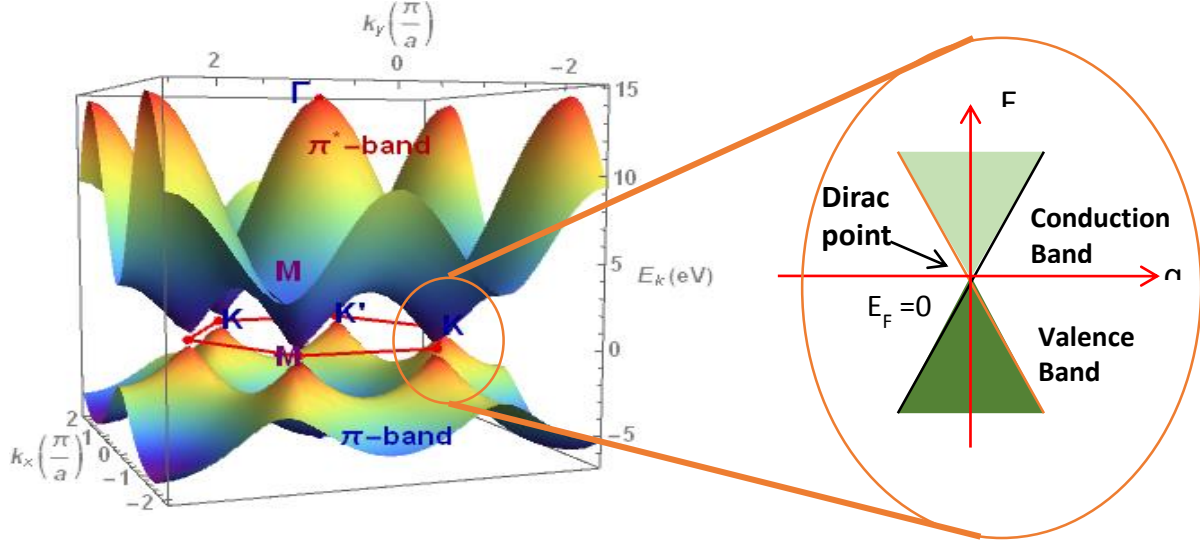
Figure 1.2: Band structure of graphene with the low energy Dirac spectrum near the K valleys. The π and π^* band are bonding and antibonding orbitals and represent valence and conduction bands near the K valley. Figure on left obtained from [34].

Now expanding equation (1.4) at the K point for small values of $\vec{q} = \vec{K} - \vec{k}$ the low energy Hamiltonian can be written as

$$\hat{H} = v_F \vec{\sigma}.\vec{p} \qquad (1.6)$$

where $\vec{p} = \hbar\vec{q}$, $v_F = \dfrac{\sqrt{3}ta}{2}$ and $\vec{\sigma} = \left(\sigma_x, \sigma_y\right)$ is a vector of Pauli matrices. The corresponding Hamiltonian for K' is $\hat{H} = v_F \vec{\sigma}^*.\vec{p}$ with $\vec{p} = \hbar\vec{q} = \hbar(\vec{K'} - \vec{k})$. The low energy eigenvalues at each valley is a linear function of momentum:

$$E(p) = \pm v_F \left|\vec{p}\right| \qquad (1.7)$$

Equation (1.6) resembles the Dirac[35] equation in 2D for ultra-relativistic massless fermions with a velocity $v_F = c/300$ where c- the speed of light in vacuum. The ± values correspond to the π and

π^* bonds and refer respectively, electron and hole-like excitations near the K valley (see Figure 1.2). The corresponding eigenfunctions describing the Dirac like quasi particle excitations at K and K' are:

$$\Psi_K^{\pm}(\theta) = \begin{pmatrix} \psi_{KA} \\ \psi_{KB} \end{pmatrix} = \frac{1}{\sqrt{2}} \begin{pmatrix} e^{\frac{-i\theta}{2}} \\ \pm e^{\frac{i\theta}{2}} \end{pmatrix} \qquad (1.8.a)$$

$$\Psi_{K'}^{\pm}(\theta) = \begin{pmatrix} \psi_{K'A} \\ \psi_{K'B} \end{pmatrix} = \frac{1}{\sqrt{2}} \begin{pmatrix} e^{\frac{i\theta}{2}} \\ \pm e^{\frac{-i\theta}{2}} \end{pmatrix} \qquad (1.8.b)$$

where $\theta = \arctan\left(\dfrac{q_x}{q_y}\right)$. Note that the above wave functions at K and K' are related by a time reversal symmetry with a reflection in k-space along k_x about the M-point in figure 1.1. The wave functions are two component spinors – they have a Berry phase of π. The two components, however, do not represent the real spin of electrons but from the two sub lattices. The Pauli matrix operators in equation (1.6) are therefore referred to as 'pseudospin' operators. They operate on the sub-lattice degree of freedom.

1.2.2. Chirality and the absence of backscattering

The Dirac-Weyl equation (massless Dirac equation) in QED describes two types of particles described by a quantity known as chirality (or helicity for massless spin ½ particles). The chirality operator is defined as: $\hat{h} = \frac{1}{2}\vec{\sigma}.\hat{p}$ where $\hat{p}$ is the unit vector in the direction of momentum. For graphene's Hamiltonian in (1.6), $\left[\hat{H},\hat{h}\right]=0$. Therefore chirality is a conserved quantity. It describes the projection of pseudospin on the direction of momentum. The chirality operator acting on the wave functions at K and K' gives

$$\hat{h}\Psi_K^{\pm}(\theta) = \pm\frac{1}{2}\Psi_K^{\pm}(\theta) \qquad (1.9.a)$$

$$\hat{h}\Psi^{\pm}_{K'}(\theta) = \mp \frac{1}{2}\Psi^{\pm}_{K'}(\theta) \qquad (1.9.b)$$

In the K valley the electrons have right handed (positive) chirality whereas the K$^{'}$ valley has negative chirality. Electrons and holes of the same valley have also opposite chirality (see figure 1.3).
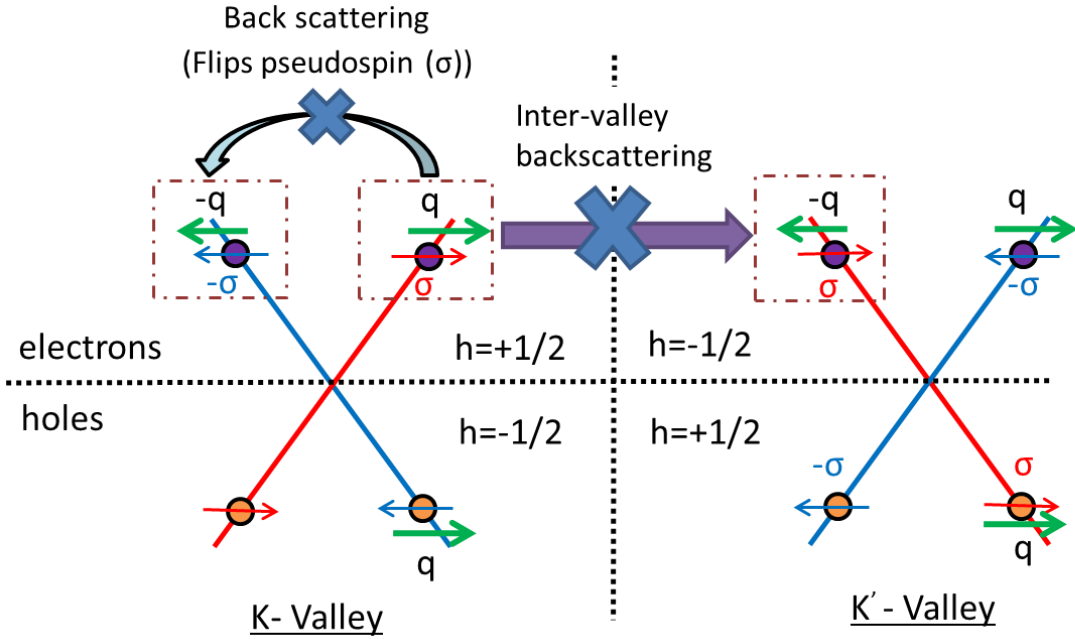
Figure 1.3: Illustration of the absence of intra-band elastic back scattering in graphene for electrons. The electron momentum for backscattering flips from q to –q (along→ direction). Here h represents chirality and σ represents pseudospin (colored to represent the sub-lattices A and B). The intra-valley back scattering (light blue curled arrow) cannot happen since the electron has to flip pseudospin i.e., blue branch to red branch of the spectrum. Inter-valley scattering (purple arrow) cannot happen because it will violate chiral conservation.

Pseudospin and chirality have important consequences on scattering in graphene. Consider Hamiltonian (1.6) with a scatter potential $\hat{V}(r) = V(r)\hat{I}$ where $\hat{I}$ - unit matrix. This potential does not operate on the sub lattice space i.e., it does not couple the sub lattices. Then the probability for

intra-valley elastic back-scattering ($\vec{q} \to -\vec{q}$) is zero since the pseudospin that is coupled to the momentum cannot be flipped. For K valley this can be shown from equation (1.8.a) as

$$\left\langle \Psi_K^+\left(\vec{q}(\theta)\right) \middle| V(r) \middle| \Psi_K^+\left(\vec{q}(\theta+\pi)\right) \right\rangle \propto i\left\langle \Psi_K^+\left(\vec{q}(\theta)\right) \middle| \Psi_K^-\left(\vec{q}(\theta)\right) \right\rangle = 0. \tag{1.10}$$

More generally using the first Born approximation, for $\left|\vec{q}_i\right| = \left|\vec{q}_r\right|$, the scattering probability as a function of the angle between the incident and scattered electron φ can be written as

$$P(\varphi) = \left|\left\langle \Psi_K^+\left(\vec{q}_i\right) \middle| V(r) \middle| \Psi_K^+\left(\vec{q}_r\right) \right\rangle\right|^2 = \tilde{V}_{\vec{q}_i\vec{q}_r} \cos^2\theta \tag{1.11}$$

Similarly for potentials that do not act on the valley space, inter-valley backscattering is prohibited because of chiral conservation (Figure 1.3). From equation (1.8)

$$\left\langle \Psi_K^+\left(\vec{q}(\theta)\right) \middle| V(r) \middle| \Psi_{K'}^+\left(\vec{q}(\theta+\pi)\right) \right\rangle \propto i\left\langle \Psi_K^+\left(\vec{q}(\theta)\right) \middle| \Psi_K^-\left(\vec{q}(\theta)\right) \right\rangle = 0 \tag{1.12}$$

Suppression of backscattering gives rise to weak anti-localization in graphene [36-38]. It also has interesting consequences on the ballistic propagation of electrons across a *pn* junction: The transmission across a potential is perfect similar to the Klein tunneling of relativistic particles across a strong repulsive electrostatic barrier[25]. The experiments exploring this phenomena are discussed in Chapter 5.

1.2.3. Density of states in graphene

Using equation (1.7) and accounting for spin and valley degeneracy, the number of states in the reciprocal space in graphene is given by:

$$n(q) = \frac{2}{\pi}\left(\frac{|E|}{\hbar v_F}\right)^2 \tag{1.13}$$

which gives the density of states per unit area:

$$D(E) = \frac{1}{\hbar v_F}\left(\frac{dn}{dq}\right) = \frac{2}{\pi}\frac{|E|}{(\hbar v_F)^2} \qquad (1.14)$$

The density of states in graphene is linear in energy and vanishes at DP. This is different from the energy-independent $D(E)$ in non-relativistic 2DEG systems. Even though the carrier density vanishes at the DP, the conductivity has a quantum limited universal value of the order $4e^2/h$.

1.3. Overview of transport properties in graphene devices

1.3.1. Graphene field effect gating

One of the conveniences in studying electronic properties of graphene is the capability of using a single gate electrode to create a field on the surface electrons and tune the Fermi energy (E_F) from conduction to valence band and vice versa. The relation between E_F and the carrier density (n) follows from equations (1.7) and (1.13) and is given by

$$E_F = \hbar v_F \sqrt{n\pi} \qquad (1.15)$$

where $k_F = \sqrt{n\pi}$. Graphene devices are made by deposition of graphite flakes on Si/SiO$_2$ substrates. The Si is electron doped and serves as the gate electrode. The SiO$_2$ is the gate dielectric. In the case of suspended graphene the gate dielectric is vacuum. The gate voltage is applied between the gate and one of the grounded electrodes in contact with the graphene flake (see figure 1.4).The relationship between the gate voltage (V$_g$) and n is given by $n = (C_g/eA)V_g = \varepsilon_r\varepsilon_0 V_g/ed$ where C_g is the gate capacitance, A is the gate area, ε_r is the relative dielectric constant and d is the thickness of the gate dielectric. The gate capacitance is usually the geometric capacitance (when the gate dielectric is thin, the quantum capacitance should be considered in series with the geometric capacitance).
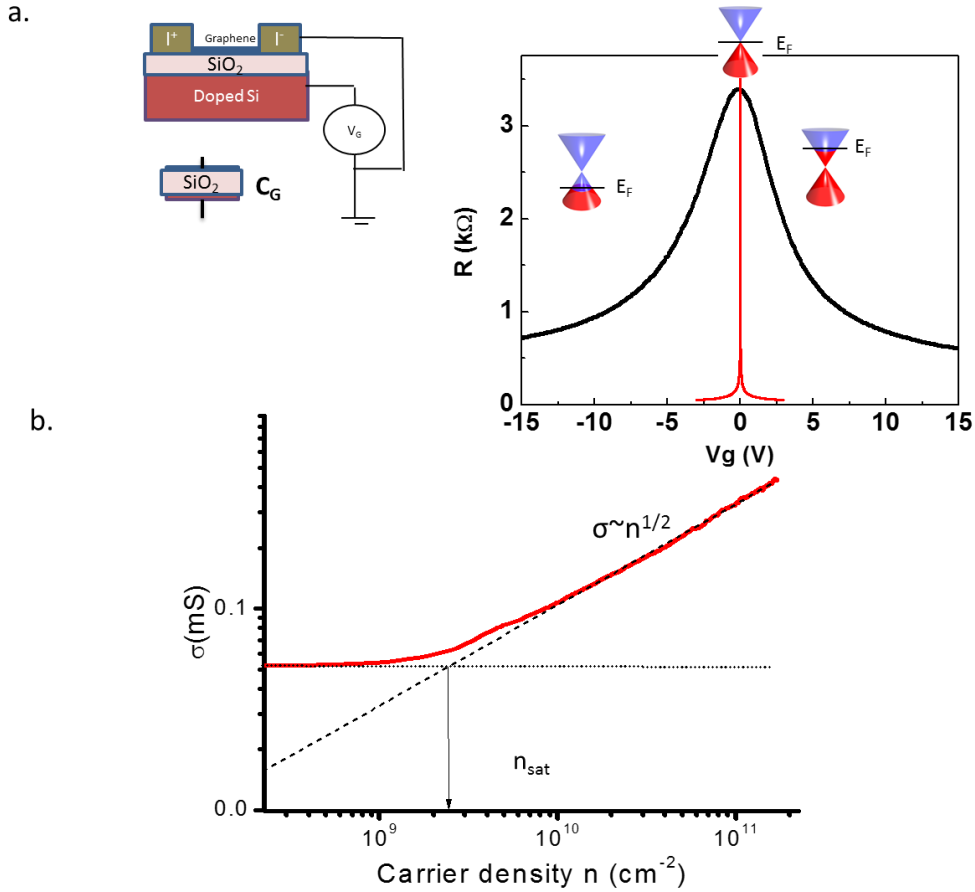
Figure 1.4 : Graphene field effect gating. a. Schematics of a device showing the gate capacitance and the ambipolar resistance vs. gate voltage. **b.** Conductivity σ as a function of carrier density (n) for a ballistic sample (plotted on a log-log scale) showing $n^{1/2}$ behavior at high carrier density and saturates to a constant below the minimum carrier density n_{sat}.

The gate voltage dependence of the resistance of an undoped ballistic device is shown in figure 1.4. The DP is at $V_g=0V$ where the resistance is maximum. Also the resistance is symmetric about the CNP reflecting the electron-hole symmetry of the low energy spectrum in equation (1.7). In experiments doping from impurities from the fabrication process can result in a non-zero gate voltage. This value varies from sample to sample and can be either positive or negative i.e., electron or hole doped. The metal contact leads can also infuse additional charge carriers in graphene forming a gate tunable *pn* junction near the leads[39]. This can cause the gating curve to become asymmetric.

1.3.2. Ballistic and diffusive transport in graphene

The conductance in a pristine graphene sheet can be calculated using the Landauer formula $G = \frac{4e^2}{h}\sum T_n$. Here the factor of 4 is for the spin and valley degeneracy in graphene. Transmission in the ballistic regime is given by $G = \frac{4e^2}{h}N$ where $N \sim W/\lambda_F$ is the number of modes at large Fermi energies. Here λ_F – is the Fermi wavelength and W- width of the graphene sheet. Using equation (1.15), the ballistic conductivity has the following relation:

$$\sigma \sim E_F \sim \sqrt{n} \tag{1.16}$$

This relation breaks down when $n \rightarrow 0$ at the DP. This is because, close to the DP, evanescent mode transport dominates over the propagating modes. Theoretically, this regime is identified as pseudo-diffusive where, even when the charge carriers are classically ballistic, their quantum transport is indistinguishable from that in diffusive metals. At DP, under certain conditions, evanescent transport alone prevails. Also the transmission is unity- a characteristic that can be related to the absence of backscattering in graphene. Several proposals exist that have highlighted on transport signatures relating to this unique behavior in graphene but several technical challenges have made experimental observations difficult. Details on this topic and some experiment evidence that shows the first hints of the transition from ballistic to pseudo diffusive like behavior is the subject of chapter 3.

Equation (1.16) implies that the mobility in ballistic graphene, $\mu \sim \frac{\sigma}{ne} \sim \frac{1}{\sqrt{n}}$ is density dependent. Due to the same reasons as mentioned above, the mobility at low n diverges due to the vanishing DOS and cannot be used for estimations near the DP. Also in real samples the ballistic relation fails due to the presence of small, but finite, potential fluctuations (electron-hole puddles) close to DP. Potential fluctuations are strongly enhanced due to topological corrugations and charge impurities [40, 41]. So the maximum mobility reported in ballistic sample is at the minimum carrier density $n=n_s$, where the slope of the μ vs. n curve begins to deviate from $-1/2$ (see

figure 1.4). Alternatively mobility and minimum carrier density (n_s) can be estimated by quantum Hall (QH) measurements. The ballistic mean free path $l_m = \dfrac{\sigma h}{2e^2 k_F}$ is also defined for densities above n_s. In ballistic samples the mean free path is only limited by the length of the sample.

In diffusive samples the conductivity is calculated using the Boltzmann equation:

$$\sigma = \frac{e^2 v_F^2 D(E_F) \tau_F(k_F)}{2} \tag{1.17}$$

Here k_F is the Fermi wave vector and $D(E_F)$ and $\tau(E_F)$ are the density of states and scattering time at the Fermi level respectively. Several sources of impurities and defects contribute to diffusive transport in graphene. The most common type of scattering in graphene devices is charge impurity Coulomb scattering. Due to the presence of Coulomb scatterers it can be shown that, $\sigma \propto n$ [42-44] making the mobility independent of n and the mean free path increase with n. This is what is usually seen in graphene on SiO_2 samples including the earliest experiments [45, 46]. For short range scatterers, such as lattice scale defects, conductance does not significantly depend on n. Other sources for diffusive transport include phonon scattering and formation of mid gap states by defect induced bound states[47]. Since the time scale of the scattering mechanisms is dependent on Fermi energy, their influence on the gating curves will vary at different V_g. The overall effect from the different mechanisms on the experimental $R(V_g)$ can be fitted using the Mathiesson's rule. Mean free path and mobility are estimated by the Drude model.

1.3.3. Substrate induced charge inhomogeneity

Long range Coulomb scattering from trapped charged contaminants between the substrate and graphene[40], the substrate roughness[48], dangling bonds[49] and defects can dope graphene and split the zero density DP into puddles of electrons and holes. This DP regime is commonly known as the charge neutrality point (CNP) to distinguish it from the ideal DP. Due to the fluctuating puddle densities, in the commonly used substrate SiO_2 the energy smear at CNP (δE_S) ~ 30meV to 100meV. This makes it impossible to study ballistic transport at low n and intrinsic physics at the DP. Two popular techniques have emerged over the years that attempted to reduce

the effect of the substrate with great success. One is to suspend graphene between the metallic contacts by etching away the substrate underneath [11, 12]. The other is by using hexagonal boron nitride (*h-BN*), a 2-D substrate with reduced surface roughness and hexagonal lattice structure similar to graphene. Suspended graphene shows high mobility and low n_s after current annealing (see 2.3.3). And to this date, suspended graphene is best for studying transport near the CNP at densities $n_s \sim 10^8$- 10^9 cm^{-2}[12] (potential fluctuations ~5meV). The main limitation of suspended graphene samples is the size. Suspending graphene for electronic devices with large dimensions and different geometries with non-invasive electrodes (like Hall Bar geometries) is technically challenging. Fabrication of graphene on h-BN has improved over the years since it was first developed and generally it can attain high nobilities and long mean free paths[50]. And since graphene is substrate supported there are no device-size limitations. But generally in graphene/h-BN the potential fluctuations ~10*meV*, slightly higher than suspended graphene.

1.3.4. Quantum Hall effect in graphene

Given the linear gapless spectrum and chiral nature of the quasiparticles in graphene, the QH effect has anomalous features distinguishable from conventional semiconductor 2D electron gas (2DEG) systems [46, 51]. In the presence of a field B, replacing $\vec{p} \rightarrow \vec{p} + e\vec{A}$ in equation (1.6) and using the Landau gauge for writing the vector potential $\vec{A} = -By\hat{x}$, the eigenenergies of the Landau levels can be obtained. It is written as:

$$E_n = sign(j)\sqrt{2e\hbar v_F^2 |j|B} \ \ where \ \ |j| = 0,1,2,3...$$
(1.18)

The Landau spectrum is $\propto \sqrt{|j|}$, which is unlike the 2D semiconductor Landau level spectrum: $E_n = \hbar\omega_c(j+1/2)$, where ω_c is the cyclotron frequency. Also, in graphene there is a zero energy, electron-hole degenerate Landau level. The electron excited Landau edge states above *E=0* share their energy with hole edge states below *E=0,* resulting in the characteristic half-integer QH effect. The Hall conductance in monolayer graphene is

$$G_{xy} = 4(j + \frac{1}{2})\frac{e^2}{h}; j = 0,1,2,.. \qquad (1.19)$$

The filling factor $\nu = \frac{nh}{eB} = 4(j + \frac{1}{2}) = 2,6,10...$, where h- Planck constant and n- carrier density. The

quantized values in bilayer graphene: $G_{xy} = 4(j+1)\frac{e^2}{h}; j = 0,1,2,...$ This difference can be used to

identify graphite flake is single or bilayer graphene.

From equation (1.18), the requirement to see at least one QH plateau in pristine graphene

is set by the following: $E_1 - E_0 = 35meV\sqrt{B(T)}$. Therefore for B>1T, integer QH effect can

emerge at room temperature for samples with a maximum δE_S ~30 meV. But disorder smears the

Landau levels and fields around 30T are normally required[45]. In suspended graphene with δE_S

<5 meV, QH features should be easily observable ~ 1T. At low temperatures, in the best suspended

samples, QH plateaus can fully develop at a few hundred mTesla.   For fractional QH effect, the

separation between Lambda levels is smaller: <5meVs for B=1T [52-54] and with currently

available magnetic fields, ballistic samples are normally required.

Other than thermal effects, for QH plateaus to develop the scattering time (τ) > the time

required to complete one cyclotron orbit: $\omega_c\tau$ >1 (or equivalently, the mean free path l_m> magnetic

length $\sqrt{\frac{h}{eB}}$). In most SiO$_2$ based graphene devices, even at low temperatures, the required fields

to observe well developed QH plateaus are higher than the theoretical values because of impurity

scattering and substrate inhomogeneity.

So it is clear that ballistic graphene devices with high mobility, long mean free path and

low potential fluctuations are essential to study intrinsic properties near the Dirac point as well as

QH effect at low fields. Low field QH and fractional QH effect are ideal to study the coexistence

of superconductivity with the Landau spectrum since most superconductors that can be used as

contacts on graphene and 2DEGs lose their superconductivity at few Tesla (for example Nb the

upper critical field is ~3.5-4T).

Chapter 2

Superconductor-graphene junctions

Superconductivity can be induced in normal metals by bringing them in contact with a superconducting material so that the coherence of the Cooper pair condensate diffuses into and survives in the normal material. Merging the relativistic Dirac fermions in graphene with superconducting correlations can lead to many interesting phenomena. Pseudo-diffusive dynamics of ballistic charges[14, 15], specular Andreev reflection[13], induced superconductivity under magnetic fields and in the QH regime[22] are some of the interesting phenomena that remain to be observed experimentally. In Chapters 3 and 4 many of these phenomena will be explored using graphene -type II superconductor devices. As a prelude, the first half of this chapter will briefly outline the basic features of superconducting proximity effect, and highlight features that are unique to graphene. The fabrication of ballistic superconductor graphene devices is crucial for observing many of the phenomena stated above. Even though most of these were predicted within years after the discovery of graphene in 2004, several technical challenges have made experimental realization impossible. The latter half of the chapter will detail how such samples are fabricated using suspended graphene. At the end of this chapter the experimental measurement setup used to characterize these devices is presented.

2.1. Superconducting proximity effect – A brief overview

2.1.1. Andreev reflection

When a superconductor (S) is in perfect contact with a normal metal (N), an electron with energy (E) above E_F but within the superconducting gap (Δ) cannot transmit since there are no quasi-particle states within the gap. In such cases charge transmission occurs by a process called Andreev reflection (AR) where an electron (hole) entering the superconductor (S) from the normal metal (N) gets reflected as a hole (electron) so that a Cooper pair can form inside S. So effectively

a charge of *2e* gets transferred across the SN interface. The electron and hole excitations involved in AR are from the conduction band (CB). Since a CB hole moves opposite to the direction of its wave vector, the hole retraces the path of the incident electron and hence the reflection is retro (Figure 2.1)[1].

The Andreev quasiparticle excited states at the SN interface are described by the Bogoliubov deGennes (BdG) equation [55],

$$\begin{pmatrix} H - E_F & \Delta \\ \Delta & THT^{-1} - E_F \end{pmatrix} \begin{pmatrix} u \\ v \end{pmatrix} = E \begin{pmatrix} u \\ v \end{pmatrix} \tag{2.1}$$

where *H* –is the free electron Hamiltonian for the N-side and *(u,v)* – represents the electron-like and hole wave functions and *T* is the time reversal operator. The reflected quasiparticle state is a time reversed state of the incident quasiparticle with a fixed phase relation determined by their energy with respect to Δ. If the superconductor used is an s-wave superconductor the net spin of the Cooper pair is zero and the Andreev quasiparticles will have opposite spins.

The phase conjugated Andreev pair can propagate into the N region extending up to a distance known as the coherence length $(\xi) \sim \dfrac{\hbar v_F}{\Delta}$. The spilling of this coherence from the superconductor across the interface and into the normal metal is commonly known as the *superconducting proximity effect(PE)[33]*. By the Andreev process the superconductor draws a charge of 2*e* for each incident charge *e*. So it follows that when E<Δ, the conductance of the interface is twice of that when the superconductors become normal.

---

[1] Note that in the illustration in figure 2.1 a step like function for the gap is used at the SN interface. This assumption is only valid in cases where 'bulk' superconducting contacts are directly in contact with a normal metal.
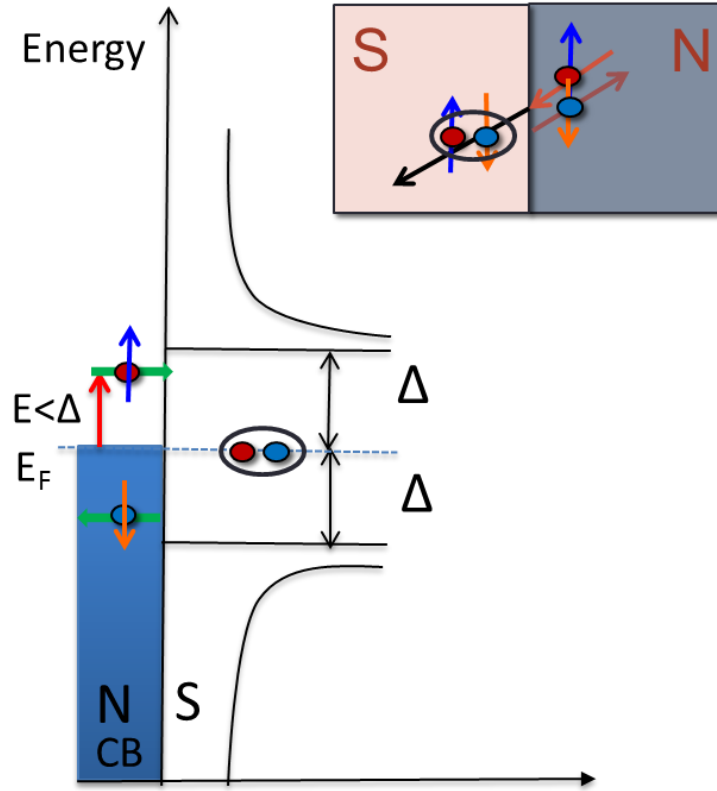
Figure 2.1: An illustration of Andreev reflection at a Superconductor-Normal interface.

2.1.2. The Blonder, Tinkham and Klapwijk model (BTK model)

In experiments the SN interface is not ideal for complete AR. Even when the E<Δ, normal scattering processes can happen. The BTK model is a widely used microscopic theory that in-cooperates the elastic scattering processes due to Fermi velocity mismatch and impurities to calculate the current-voltage (IV) characteristics of the SN interface [56]. The scattering potential is modelled by a delta function potential $V(x) = Z\hbar v_F \delta(x)$ at the interface. Here Z is known as the dimensionless barrier strength.

Solving the BdG equations with $V(x)$ [33], the current flow through the *SN* interface can be written as,

$$I_{NS}(V_{bias}) = \frac{G_N}{e} \int_{-\infty}^{\infty} [f(E - eV_{bias}) - f(E)][1 + A(E) - B(E)] dE \qquad (2.2)$$

Here $A(E)$ and $B(E)$ are Andreev and the normal reflection probabilities respectively. $f(E)$ is the Fermi Dirac distribution . G_N is the normal state conductance of the interface i.e., when the superconductors are just above T_c. V_{bias} – is the bias voltage applied across the interface. The values of A and B are a function of E, Z and can be tuned by the bias voltage. From [33],

For $E<\Delta$:

$$A(E) = \frac{\Delta^2}{E^2 + (\Delta^2 - E^2)(1 + 2Z^2)}$$
$$B(E) = 1 - A(E) \qquad (2.3)$$

For $E>\Delta$:

$$A(E) = \frac{u_0^2 v_0^2}{\gamma^2}$$
$$B(E) = \frac{(u_0^2 - v_0^2)Z^2(1 + Z^2)}{\gamma^2} \qquad (2.4)$$

with parameters

$$u_0^2 = 1 - v_0^2 = \frac{1}{2}\left\{1 + \left[(E^2 - \Delta^2)/E^2\right]^{1/2}\right\}$$
$$\gamma^2 = \left[u_0^2 + Z^2(u_0^2 - v_0^2)\right]^2 \qquad (2.5)$$

In experiments the quantity that is usually of interest is the differential resistance. The expression for the differential resistance follows from equation (2.2) and is given by:

$$\frac{dI}{dV}(V_{bias}) = G_N(1 + A(eV_{bias}) - B(eV_{bias})) \qquad (2.6)$$

It is clear that when $eV_{bias}< \Delta$, since $A\,(eV_{bias})$ increases, $\frac{dI}{dV}(V_{bias})$ increases from the normal state value G_N. For an ideal interface ($Z=0$), $A=1$, $B=0$ and the conductance below the gap is constant and twice the normal value. For intermediate Z, the conductance enhancement becomes

weaker and less abrupt. This is because the increase in $A(E)$ is mitigated by finite normal scattering probability $B(E)$. For higher Z (strong barrier or tunnel junctions) $A(E)$ is completely suppressed and $\frac{dI}{dV}(V_{bias})$ below Δ can decrease substantially reaching zero in ideal tunnel barriers with no thermal induced hopping. The differential conductance for different Z calculated by BTK is presented in figure 2.2,
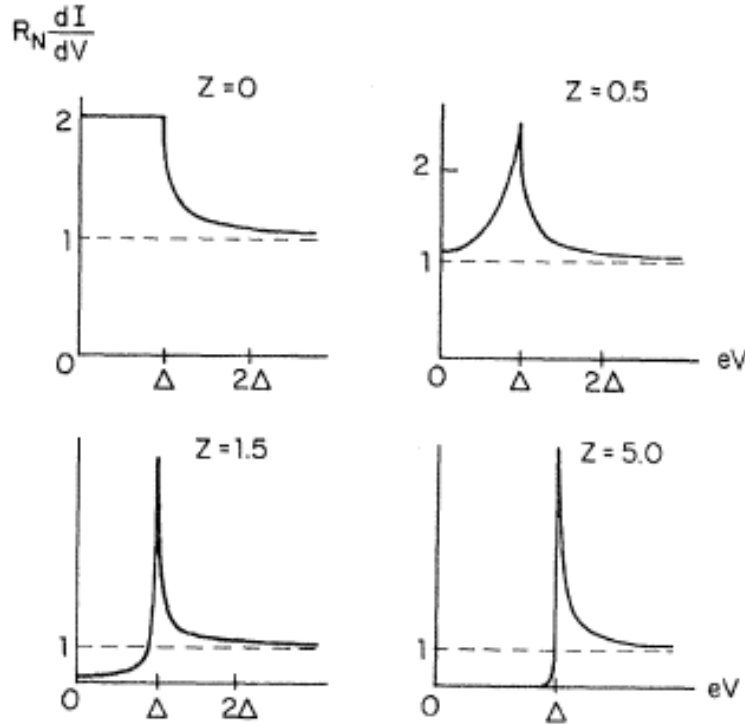
Figure 2.2: Normalized differential conductance curves for different values of Z based on the BTK model. The plots are from [56].

2.1.3. Excess current

The DC current voltage (IV) curve of a transparent SN junction does not follow a linear Ohmic relation $V=IR_N$ where $G_N=1/R_N$. This is because additional current flows through the *SN* interface due to the proximity effect when eV<< Δ. The linear fit for the IV curve for eV_{bias}>> Δ, has a slope G_N with a non-zero intercept at $V=0$. The value of the intercept is the excess current (I_{exc}). The expression for the excess current can be written as[56]

$$I_{exc} = (I_{SN} - I_{NN})\bigg|_{eV \gg \Delta} = \frac{1}{eR_N[1 - B(\infty)]} \int_0^\infty [A(E) - B(E) + B(\infty)]dE , \qquad (2.7)$$

where $B(\infty) = \dfrac{Z^2}{(1+Z^2)}$. For a fixed temperature $\dfrac{I_{exc}R_N}{\Delta}$ is only a function of Z. The dependence

of I_{exc} on Z for T=0 is shown in Figure 2.3(a) and the method to calculate excess current from an IV plot is shown in Fig 2.3 (b). Using the value of the excess current, the strength of the proximity effect of a junction can be evaluated.
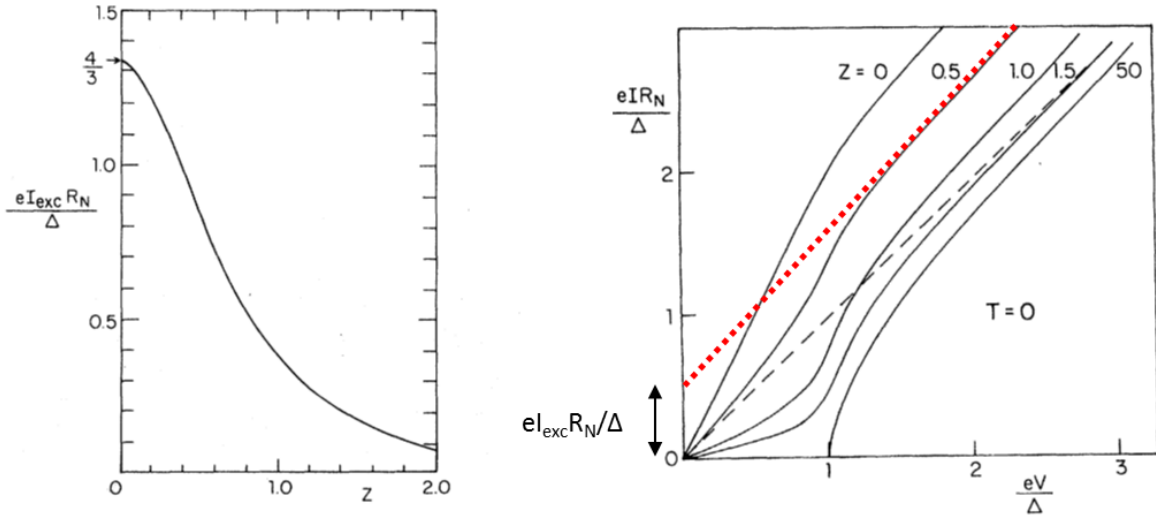
Figure 2.3: Excess current (I_{exc}) in SN junctions: **a.** I_{exc} as a function of Z. **b.** IV curves for junctions with different Z at T=0K. The red dotted line is a linear fit for curve Z=0.5. The black dotted line represents the Ohmic curve with zero intercept. Both lines have a slope of R_N. The plots were adapted from reference [56].

2.1.4. SNS junctions: Multiple Andreev reflections (Sub harmonic gap structures)

In a normal metal separated by two superconducting contacts (SNS junctions), the excess current is almost twice of that of the SN junction[57]. In SNS junctions close to zero bias and when $\xi >$ L-length of N channel, a Josephson supercurrent flows through the channel. This current has a phase that is related to the phase difference of the two superconductors and is an AC current (The excess current is a DC current and does not include the dissipationless AC current at zero bias).

The AR processes takes place at finite biases and for SNS junctions this can happen when $eV_{bias} <$ 2Δ. The dip in $\frac{dV}{dI}(V_{bias})$ occurs at $V_{bias} = 2\Delta/e$ (see figure 2.4 right).

Unlike in SN junctions, in SNS junctions when $eV_{bias} < 2\Delta$, in the absence of any decoherence mechanisms in the normal metal, the Andreev pair can traverse from the left superconducting lead to the right and undergoes an AR again. The number of times the AR happens reflect as harmonic oscillatory features in the DC IV characteristics. To understand the harmonics, a simple way is to focus on the transport of a single electron in N between the two S-leads. Let V_{bias} be the voltage bias between the two S-leads. When $|eV_{bias}| > 2\Delta$ there is no Andreev process and an electron just normally escapes from the left lead to the right lead. But if $|eV_{bias}| = 2\Delta$ then at least a single AR becomes possible and an effective charge of 2e is transferred through the junction. If $2|eV_{bias}| = 2\Delta$, AR happens twice, one at each lead. The charge transfer is now with 2x2e into the superconductors. This is illustrated in Figure 2.4. Decreasing V_{bias} further, more ARs take place at the superconducting leads leading to more charge transfer in multiples of 2e. The V_{bias} and the number of ARs (n) are related by the following equation:

$$eV_{bias} = \frac{2\Delta}{n} \text{ , where } n=1,2,3 \text{ etc.,} \tag{2.8}$$

The coherent sum of many such multiple AR (MARs) results in proximity effect with a sharp dip in dV/dI at values of V_{bias} given by equation 2.8. These oscillatory signatures from MARs are also known as sub harmonic gap structures (SHGS). Figure 2.4 shows an experimental curve for an Al-graphene Josephson device at T=270mK. At-least three SHGS are discernible. The vanishing dip at V_{bias}=0 is due to the onset of supercurrent. The number of SHGS that are experimentally observable depends on thermal noise and the transparency of the interface.

The MAR dip features and normalized supercurrent (I_cR_N) are gate (density) independent in diffusive samples. It was shown that the magnitude of the MAR dips were dependent on L/ξ, where L- is the length of the junction and $\xi = \sqrt{\frac{\hbar D}{\Delta}}$ – the coherence length in N. Here $D = \frac{v_F l_m}{2}$ is the diffusive constant. This was confirmed with graphene-Al SNS junctions [20].
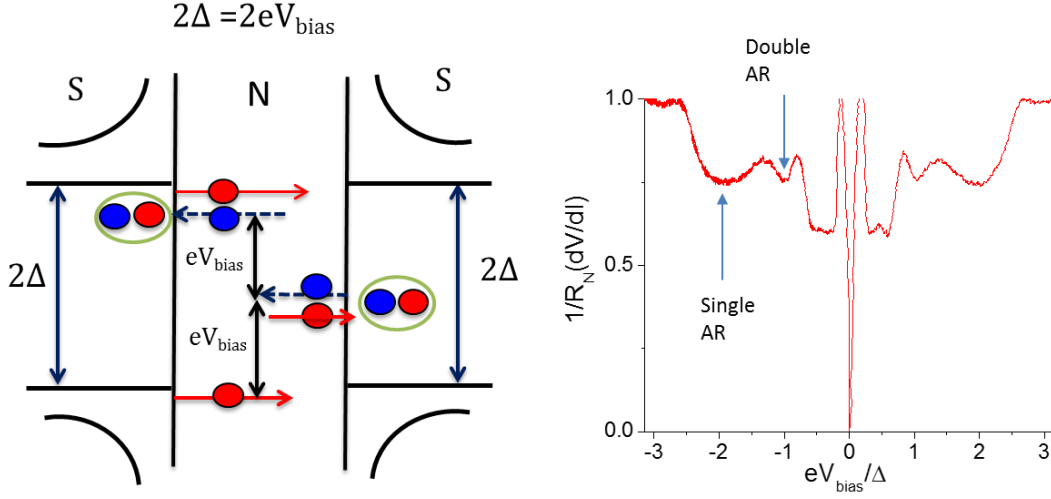
Figure 2.4: Sub harmonic gap structures due to multiple Andreev reflections (MARs): (left) Illustration for double AR i.e., $2\Delta=2eV_{bias}$. (right) An experimentally measured normalized differential resistance vs. V_{bias} curve showing dips associated with MARs.

2.1.5. Andreev reflections in graphene – Retro and specular

Proximity effect in graphene can be described in the same way as in other metals by using the BTK model. But replacing the Schrodinger equation with the Dirac Hamiltonian in the BdG equation presents some additional properties that differ from normal metals.

As mentioned earlier, Andreev electron and holes are time reversed. So the superconducting pair potential will couple states in graphene from the time reversed valleys – K and K$^{'}$. The quasiparticle electron-hole states (u,v) should then be described by the four component spinor wave functions $(u_1, u_2, v_1, v_2) = (\psi_{A,K}, \psi_{B,K}, \psi_{A,K'}^*, \psi_{B,K'}^*)$. The time reversal operator $T = \begin{pmatrix} 0 & \sigma_z \\ \sigma_z & 0 \end{pmatrix} C$ where C- charge conjugation operator[58]. In ballistic systems, the two valley transport is intrinsic to graphene while in the normal state it is single valley transport. Although presence of certain scatterers can couple valleys in diffusive systems, the resulting transport is not intrinsic to graphene and is sample (or impurity) dependent [19]. The phase coherent two valley transport has led to interesting proposals in the detection of valley polarization in ballistic graphene [17].

Unlike in normal metals, in graphene the AR probability is unity even when Z is finite. This is because AR does not flip pseudospin i.e., Andreev electrons and holes in graphene belong to the same sub lattice. Backscattering without AR would require scattering to a different sub-lattice. This will violate chiral conservation. Therefore the quasiparticle has no other way but to undergo AR.

Another interesting phenomenon which is unique to a zero gap semiconductor like graphene is that the ARs can be inter-band i.e., the electrons from the conduction band can Andreev scatter as a hole in the valence band. This requires the Fermi energy (E_F) < superconducting gap (Δ). Since a valence band hole moves in the same direction as its wave vector, unlike in retro reflection, only the velocity component perpendicular to the interface is flipped. As a result the reflection becomes *specular*[13] (Figure 2.5). Exploring this experimentally is challenging since it requires ultra clean samples with less energy smearing at CNP compared to the superconducting gap which is typically a few meVs. Specular AR is explored experimentally at the end of Chapter 3.
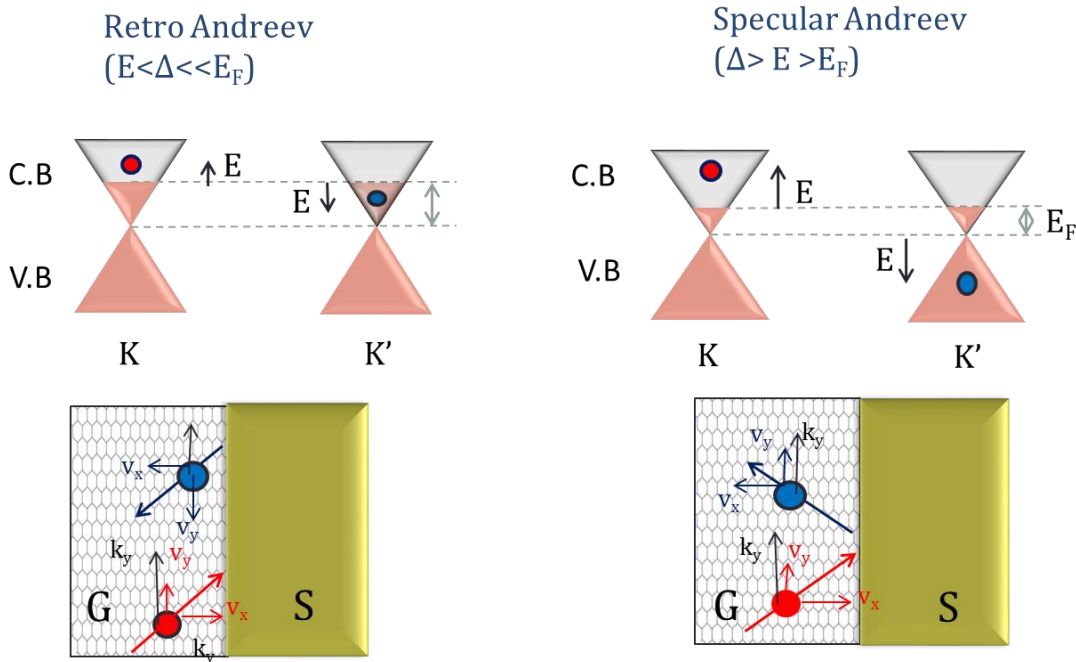
Figure 2.5: Illustration of retro and specular Andreev reflection at a Superconductor (S) graphene (G) interface. C.B- conduction band, V.B valence band. v and k are group velocity and wave vector respectively. Here $E=eV_{bias}$.

2.1.6. Andreev reflection in magnetic fields

With a type-II superconductor coupled to a normal metal, it is possible to retain the superconducting properties of the lead at higher fields, up to the upper critical field of Hc_2, while studying the response of the Andreev pair in the normal metal. In retro AR the electron and hole are from the same (say conduction) band. With negative mass and opposite charge, the cyclotron orbit of the hole in a magnetic field has the same rotation as the electron. The situation is different in graphene for specular (inter-band) AR, where the cyclotron orbits are opposite for electrons and holes. Experiments can be designed in large scale ballistic devices that can detect these spatially different cyclotron trajectories. The trajectories can be switched back and forth by tuning the Fermi energy towards and away from the Dirac point. This is illustrated in figure 2.6.
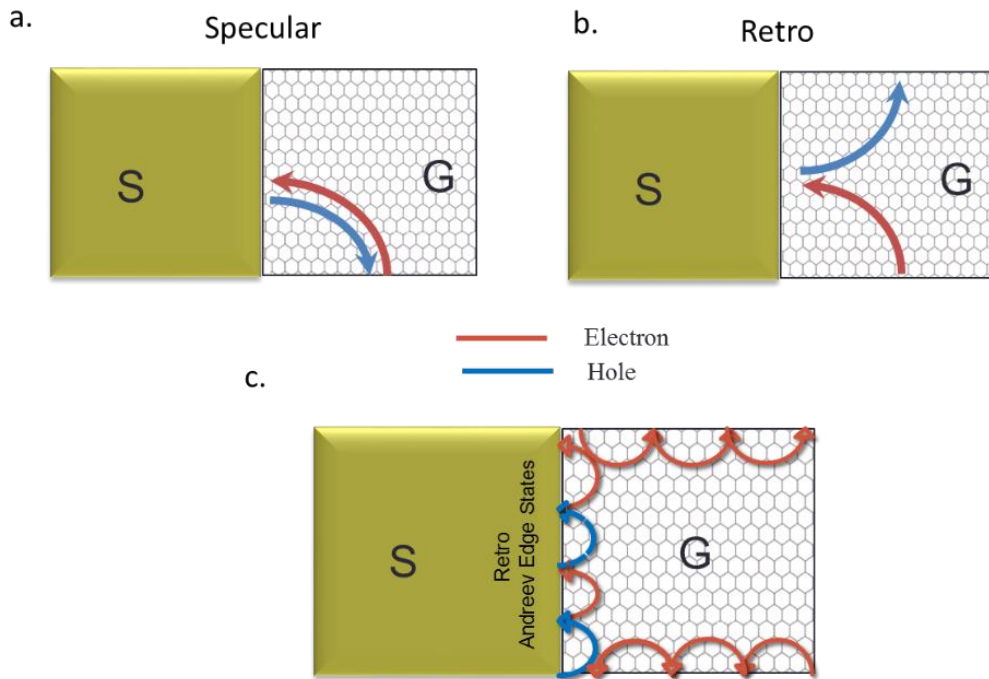
Figure 2.6: Illustration of Andreev reflection in magnetic fields: a. and **b.** In low magnetic fields**:** Direction of electron and hole cyclotron orbits for specular (a) and retro (b) Andreev reflection. **c.** Formation of (Retro) Andreev edge states in the QH regime (high magnetic fields). Magnetic field is directed out of the paper.

Thin film type II superconductors support vortices at low magnetic fields. Their effect on the Andreev pair at the interface is also an interesting question. This is discussed in Chapter 4. At high magnetic fields when the bulk becomes insulating, alternating Andreev electron and hole skipping orbits are formed at the superconducting interface. These are known as "Andreev edge states". Depending on the phase coherence of the Andreev pair on the normal side and the quality of the interface, the presence of these Andreev edge states is expected to change the QH conductance from conventional values. In the ideal case it is expected that the quantized conductance values should double[22]. The effect of specular AR in the QH conductance and the proximity effect in graphene's fractional QH regime are other prospective studies that can be initiated using ballistic graphene superconductor devices.

2.2. Fabrication of superconducting graphene (SGS) junctions

The study of proximity induced effects in electron gas system requires a transparent SN interface. Graphene practically is a semimetal and is well known for forming good Ohmic contacts with various metals and induced superconductivity in graphene was reported in 2007[19-21]. But studying ballistic transport properties in such Josephson devices has remained challenging. This requires improved fabrication schemes that can produce a transparent interface. Also such interface should remain robust after current/thermal annealing and other pre-processing procedures, typically required for producing a pristine graphene strip. Moreover studying Andreev edge states and intrinsic transport near the CNP such as specular AR requires type II superconductors with higher Hc_2 and a large superconducting gap. These superconductors are typically sputter deposited and pose additional challenges. In this section a method to successfully fabricate ballistic-suspended and graphene with type II superconductors (Nb and NbN) is presented. Such samples are used to observe pseudo-diffusive behavior in graphene near Dirac point, which will be the subject of Chapter 3.

2.2.1. Suspended graphene superconductor junctions

Our approach to make ballistic devices is to use suspended graphene. The most common way to suspend graphene for electronic characterization is by clamping the graphene by contact leads and to use etchants such as buffered HF to remove the SiO_2 underneath. Details of this

method will be explained in Chapter 5. Since commonly used superconductors like *Nb* and *NbN* are reactive to etchants, an etch-free technique is required. We achieve this by using two layers of contrasting e-beam resist with the graphene sandwiched in between. Then by careful control of the e-beam dose and the developing procedure the graphene is eventually suspended over the SiO_2 substrate. The details of the procedure are outlined below.

A. Deposition of graphene by mechanical exfoliation

1. A Si/SiO_2 substrate with 300 nm of SiO_2 and predefined alignment marks is washed in acetone/IPA and is cleaned in UV-ozone for 20 minutes. The Si is n-doped and serves as the back electrode.

2. Immediately before graphene deposition the substrate is baked for 2 minutes at 400^0 C and then spin-coated with Microchem^{TM} Polymethyl methacrylate (PMMA) - A4 at 3000 rpm. The resulting thickness of the film is 220 nm. The substrate is baked for 90s on a hot plate set at 180^0C. To ensure a good thermal contact with the plate, the back of the substrate is carefully wiped clean of PMMA using an acetone soaked Q-tip and the sample is covered with an aluminum lid during the baking.

3. *Blow press method*: Thin highly oriented pyrolytic graphite (HOPG) flakes are peeled from the bulk using a sharp tweezer and placed carefully on the PMMA surface. Then it is "blow pressed "using clean and dry N_2 gas through a needle, ~0.7 mm in diameter for 3-5s. The deposition works well when liquid N_2 pressure is maintained between 20-30 psi and the humidity around 20-30%. The single layers left behind are identified under an optical microscope. Since graphene is deposited on the PMMA resist, the contrast may not be sufficient to identify graphene. But by adjusting the aperture of the objective lens or employing digital color filters the contrast is improved. The green and luminescence filters provide the best contrast.

   Other variations used in depositing graphene: For deposition on the PMMA resist the typical scotch tape method is not preferred as it leaves irremovable glue residues that can get on the graphene piece while processing in solvents. An alternative is using the silicone free 'blue tape' from Ultron Systems R 1007 (Here residues can be washed away by warm acetone). Also flakes exfoliated from a flat monochromatic graphite by the blue tape produce small single layer pieces on PMMA with a slightly higher yield than the blow press method.

4. Once a suitable single layer flake (straight edged flat rectangular flakes gave better results) is identified the second layer of resist – Methyl methacrylate (MMA) 8.5 EL 8.5 is spun on the substrate. The spinning speed is slowly ramped from 0 to 3000 rpm to minimize the rolling up of deposited graphene flakes. Then the substrate is baked at 150^0 C on a hotplate for 90s, same care as before (Figure 2.7 (a)).
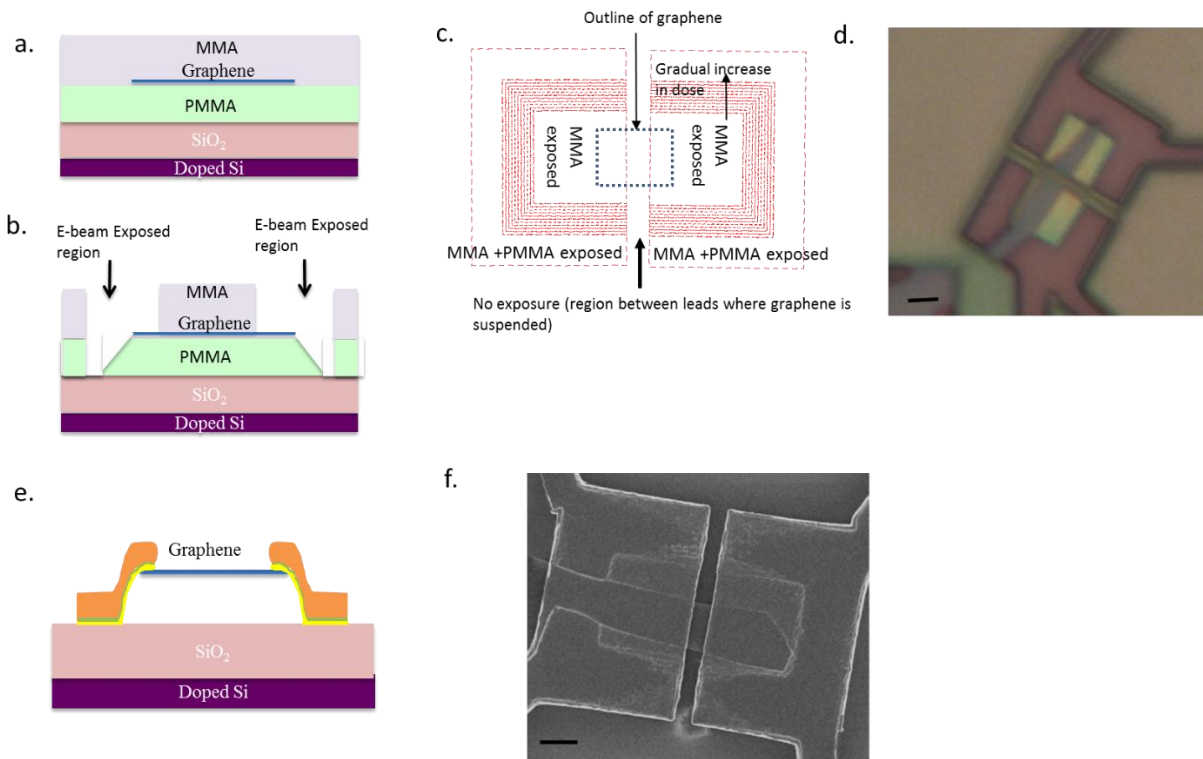
Figure 2.7: Etch free – double resist fabrication for suspended graphene – Superconductor junctions: a. before EBL **b.** after EBL **c.** EBL design showing the different exposure region **d.** Optical image of device after EBL and developing **e.** after metal deposition and lift off **f.** SEM image of final device (top view)**.**

B. E-beam lithography (EBL)

EBL is performed using carefully controlled doses on the two different resists sandwiching graphene. Suspended graphene is usually supported by metallic contacts. But since no part of graphene is in contact with the substrate, a pill-box support structure is designed as shown in figure 2.7 (c). In the 'inner' rectangular region low dose is used so that only MMA gets developed. This inner region, after metal deposition, will form a suspended contact to the suspended graphene channel. Towards the 'outer' region the dose is gradually increased so that the PMMA layer also gets developed. Eventually the dose for the outer leads reaches a value that enables both PMMA and MMA to be completely developed. The NPGS design of the gradual dose region is shown in figure 2.7(c). It is composed of closely spaced C- shaped enclosures with a width of 10 nm. Here the dose is increased in steps of $10\mu Ccm^{-2}$.The gradual increase of dose ensures a smooth transition of the metal contacts from the suspended region to the substrate. This technique is also economical in the use of metals especially in cases where the PMMA layer needs to be thick.

After EBL, the sample is developed in Methyl isobutyl ketone (MIBK): isopropyl alcohol (IPA) = 1:3 for 45s, followed by a minute in cold deionized (DI) water: IPA (1:3) and a final rinse in IPA for 35 s before blow drying with dry N_2 gas. During this procedure the sample is held with a tweezer and gently swayed in the developers for effective results. The cold DI water + IPA help to remove the fine PMMA residue, which is typically difficult to remove using MIBK alone. A sample after developing is shown in figure 2.7 (d). Right before metal deposition, the developed samples are exposed to UV ozone for 1.2 minutes to remove any remaining organic residue.

C. Thin film metal deposition

The superconductor contacts are defined by DC magnetron sputtering. But due to the intrinsic strain of sputtered films, direct sputtering on graphene damages it, creating a bad interface. Therefore prior to sputtering buffer layers of very thin normal metal are deposited by e-beam physical vapor deposition (EBPVD). The samples are kept pumped for at least 10 hours in a UHV chamber equipped with the apparatus for both EBPVD and DC magnetron sputtering. The long pumping helps to remove desorbed impurities and water on the sample and chamber surface.

i. e-beam physical vapor deposition (EBPVD)

In EBPVD, accelerated electrons hit a crucible containing the metals evaporating them. The metal vapor rises and coats the sample directly facing the crucible at a distance.

For a good S-G interface it was found that a pressure of $\sim 2\times10^{-8}$ Torr or lower is required before evaporation onto the sample. The vacuum conditions are further improved by briefly preheating the Ti crucible an hour before deposition (with the sample facing away). This allows for the Ti vapor to trap residual gases and seal sources of outgassing in the walls of the chamber. When all these conditions are met, the first layer, Ti ~1.5nm is evaporated quickly followed by Pd ~1nm. Ti forms a very good sticking layer while Pd acts as a protective layer sealing Ti from any unwanted exposure. This is especially important in the reactive sputtering of NbN, where N_2 gas is used (see next section). Each metal pocket is preheated to establish a steady base pressure and growth rate ($2A^0$/s) before exposing it to the sample. Slower growth rate can leave the coated metal layers vulnerable to impurities.

ii. Sputter deposition

After EBPVD, the sample is sputter deposited with the superconductor material in the same UHV chamber. Sputter deposition is a physical vapor deposition technique where free electrons from a negatively charged target (made of the material of interest, here Nb) ionize the gas medium (typically Argon) in the deposition chamber. These positively ionized atoms (plasma) are accelerated back to the negatively charged target and a cascade of collision results in atoms being sputtered from the target surface. These atoms then get deposited on the sample facing the target. A constant flow of the gas is maintained in the chamber during the process. In DC magnetron sputtering used here, the magnetic field controls the sputter rate. In this thesis work, two kinds of superconducting films were used – Nb and NbN. And in both cases a 3" circular Nb target is used. Nb sputtering is a non-reactive process using the inert gas Ar for the plasma. NbN is reactive sputtering where a mixture of Ar and N_2 is used on the Nb target. During the sputter process the bombarded Nb target reacts with nitrogen ions forming NbN.

A crucial challenge in sputter deposition on graphene is stress. The use of buffer metals alone is not sufficient to protect graphene from tear or damage due to stress. To determine the type of stress, the film is sputtered on stress free Al pre-evaporated on PMMA and lifted off in acetone which slowly dissolves the PMMA releasing the bimetallic Nb/Al (or NbN/Al) film. This process is observed under an optical microscope. In the case of compressive stress, the film bubble that

detaches forms a "flowery" or wrinkled rim as the detached film tries to increase the surface area and minimize the elastic energy. When the film bubble breaks they curl downwards. A tensile film, on the other hand, forms a spherical bubble with a sharp rim and when broken curls upwards (see figure 2.8).
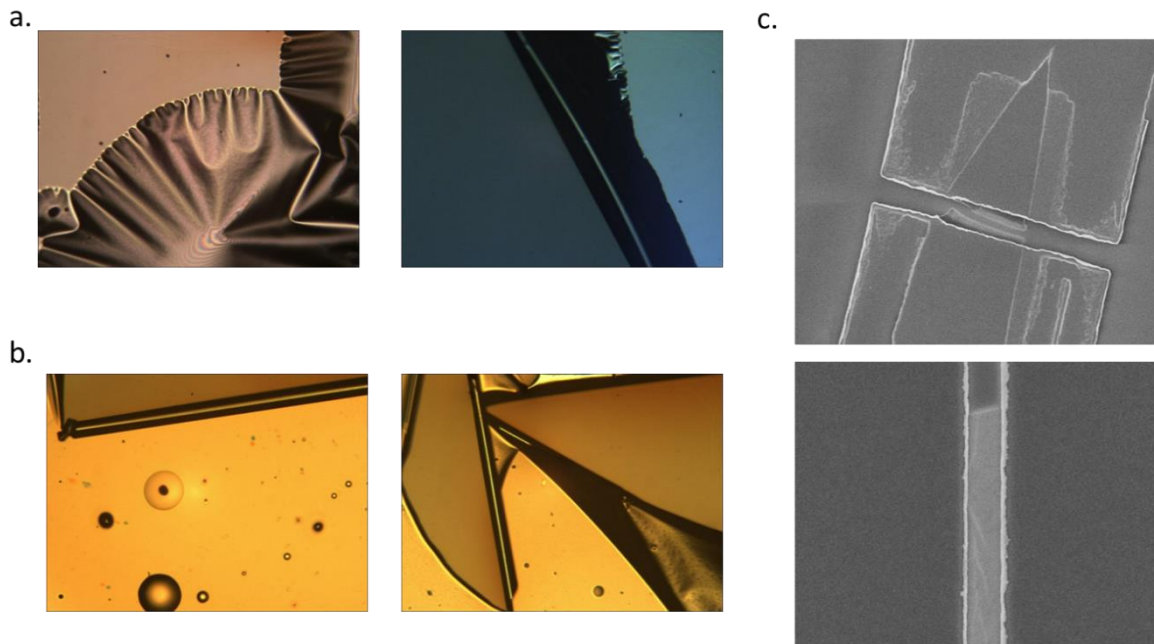
Figure 2.8: Stress tests for sputtered Nb films. Optical images of Nb/Al bimetallic film when lifted off in acetone from PMMA/Si substrate. **a.** Films with compressive stress **b.** Films with tensile stress **c.** SEM image showing a graphene channel torn apart (top) and cracks (bottom) due to stress from the sputtered film.

The stress in both reactive and non-reactive sputtered NbN and Nb depends on the flow rate, the pressure of the gases, the sputter gun power and the distance of the sample from the target. So to find the best combination of parameters, initially the target-sample distance and the power were determined to give the best possible results for T_c with a reasonable contact on graphene. Then the 'lift off tests' were performed by tuning the flow rate and the pressure of the gases each time until the minimum stress condition is found. Finer tuning of the parameters is normally required as the minimum stress values did not provide the best results on graphene. This might be because the lift off test only shows the effective stress of the whole film. But stress can vary across the layers. The stress of the first few deposited layers on graphene can be slightly different from

the results from the lift off tests. On graphene the resistance drop below T_c and the value of the induced gap were used as gauges for the quality of the sputtered film.

Reactive sputtering for NbN: For reactive sputtering, consistent with literature, high Ar/N_2 pressure causes tensile stress while a low Ar/N_2 pressure causes compressive stress [59]. The stoichiometric changes in Nb and N_2 near the target can cause the intrinsic stress between each layer of the film during sputtering. To reduce this, the flow rate of the gas mixture is increased while adjusting the shutter valve to maintain a steady pressure. It was found that the Ti buffer layer can also react with the Ar/N_2 plasma causing bad contact resistance even at stress free sputter conditions. To eliminate this, the Ti was covered with thin layer of Pd, as mentioned earlier.

After all parameters are determined, the sputtering procedure used is as follows: After EBPVD on sample, the chamber is partially closed from the cryopump using a shutter valve and Argon gas is introduced into the chamber. The flow controller and the shutter valve are adjusted so that a steady flow rate and a constant chamber pressure of 8.4 mTorr (Ar - 7.5mTorr + N_2 - 0.9mTorr) is achieved. Right before sputtering on the sample, the target surface is made fresh by pre-sputtering for 80 seconds with the sample facing away. A constant power of 470W is provided to the Nb target at the time of sputtering. The voltage and current values typically vary from 378-380V and 1.23-1.25A. While in operation, the pressure changes from 7.6 to 7.4mTorr indicating the use of N_2 in the reaction. This value was found to be ideal for stress free films and is often used as a check-parameter for instabilities in chamber or target conditions. After pre-sputtering the sample is rotated so that it faces the target. Then 70-80 nm of the superconductor at the rate of 1nm/s is sputtered. The distance between the target and the sample holder is ~10 cm.

Non -reactive sputtering for Nb: In the case of non-reactive sputtering, a similar trend in stress is seen: high Ar pressure shows tensile stress while low Ar pressure shows compressive stress. Here changes in Ar pressure and rate of deposition can cause the intrinsic stress. The established procedure used in this thesis is as follows: After EBPVD, the chamber is partially closed from the cryo-pump using a shutter valve and Ar gas is introduced into the chamber. The flow controller and the shutter valve are adjusted so that a stable flow rate with a chamber pressure of Ar (8.17 mTorr)) is achieved. Right before sputtering on the sample, the target surface is made fresh by pre-sputtering for 80 seconds with the sample facing away. A constant power of 400W is provided to the 3" Nb target at the time of sputtering. The voltage and current values typically vary from 321-326V and 1.19-1.24A. While in proper operation the pressure is stable varying by

only by 0.025mTorr. If the change of pressure during growth exceeds 0.05 mTorr, it results in intrinsic strain and poor transparency of the contacts. After pre-sputtering the sample is rotated so that it faces the target and 60-65 nm of the superconductor at the rate of 1nm/s was deposited. The distance between the target and the sample holder during sputtering is ~10 cm.

D. Lift-off

After sputtering the sample is unloaded from the chamber. A small scratch is made on the corner of the substrate to expose Si for gate wire bonding before liftoff[2]. For the lift off process, the sample is immersed in warm acetone (70^0C). The acetone dissolves the resist layers lifting off the metals with it. During the first 30s of lift off, the sample is swayed gently in the solvent so that the detached metal films do not have a chance to stick back onto the substrate. After 10 minutes the sample is quickly transferred to a fresh batch of acetone and kept covered for 10-15 minutes at the same temperature. This ensures a more thorough removal of the resist layers. (Note: At this stage the graphene is now suspended in acetone. So from here on, when handling the substrate, utmost care is taken to avoid collapse of graphene static charges. Also the substrate should not be directly taken out to air. This is because change in surface tension will force the suspended graphene to collapse). Next, acetone is diluted with IPA and then the sample is quickly transferred to a fresh beaker of pure IPA and kept for 10 minutes. To take the sample safely out to air, a beaker of IPA is boiled on a hotplate until bubbles emerge and then is allowed to cool briefly for ~`10-15 s. Once the IPA is ~80^0C (and not boiling!), the sample is quickly transferred and gently stirred for 5s to equilibrate with IPA temperature. Then it is taken out and held vertically to dry[3]. Since warm IPA has a reduced surface tension and dries off quickly, this method serves as an effective substitute to critical point drying. Hexane is also used at times as a substitute to IPA. The advantage with hexane is the boiling point is lower (68^0C) and therefore the sample does not have to undergo a huge thermal gradient. The SEM image of a sample after liftoff is shown in figure 2.7(f).

---

[2] This process may induce momentary electrostatic charges on the substrate and if graphene is already suspended electrostatic force may force it to collapse. So as a precaution this is done before liftoff.
[3] Note: IPA should vaporize immediately and the surface should be dry within a couple of seconds. Any IPA trapped in the tweezers should be allowed to dry thoroughly or should be wiped off carefully so that it does not get on to the sample

2.2.2. Non-suspended superconductor- graphene devices

For non-suspended sample there are only a few differences in the procedure. PMMA A4 at 3000 rpm is the only resist used. EBL is straightforward with a single dose of 420 μC/cm^2. The sample is developed for 2 minutes in cold water: IPA (1:3) and then rinsed in IPA for 35 s before blow drying in dry N$_2$. Metal leads are made of Ti (2nm), Pd (1.5nm) and the superconducting film (~40 nm).

2.3. Measurement setup and techniques

Although a variety of different instruments and setups were used over the course of this dissertation work a few of the most commonly used instruments and measurement setups are summarized below.

2.3.1. He-3 Insert design and operation

All the superconductor-graphene devices presented in this thesis are measured in a home built He-3 refrigerator placed in the Variable Temperature insert (VTI) space of the Oxford superconducting magnet Dewar. The He-3 refrigerator is designed without a 1 K plot as seen in figure 2.8. So to achieve sub Kelvin temperatures, first the He-3 gas stored in a can at the top of the insert is completely condensed, at a stable temperature of 1.5K, into the He-3 pot located right above the sample. The stable temperature of 1.5 K is maintained by controlled pump-flow of He-4 gas through a capillary in the VTI space of the Oxford superconducting magnet Dewar. This process plays the role of the 1-K plot. During this condensing process, the sorb is heated at 40 K to release any trapped He-3 gas and ensure complete condensation. Sorb heat and temperature is provided by CryoCon 22 Temperature controller. After sufficient time (~ 45min) is allowed to condense the entire He-3 gas in the condenser, the sorb heater is switched off. Once the sorb reaches a temperature of 1.5K it pumps on the He-3 cooling the He-3 pot and sample further down to 300mK. Baffles are deployed to isolate the He-3 pot and sample from high temperature elements. Stainless steel tubes are used for the pumping lines. The sample sits in vacuum in good thermal contact with the He-3 pot but is sealed off from the He-4 bath by a brass can. A common problem encountered in the design is super-leak. This may be due to minute imperfections when

machining the conical seal of the brass can. Various greases like Apiezon N and Bluestar CAF 1 red silicone elastomer were used to reduce the leak but a redesign of the seal is necessary for long term operation.

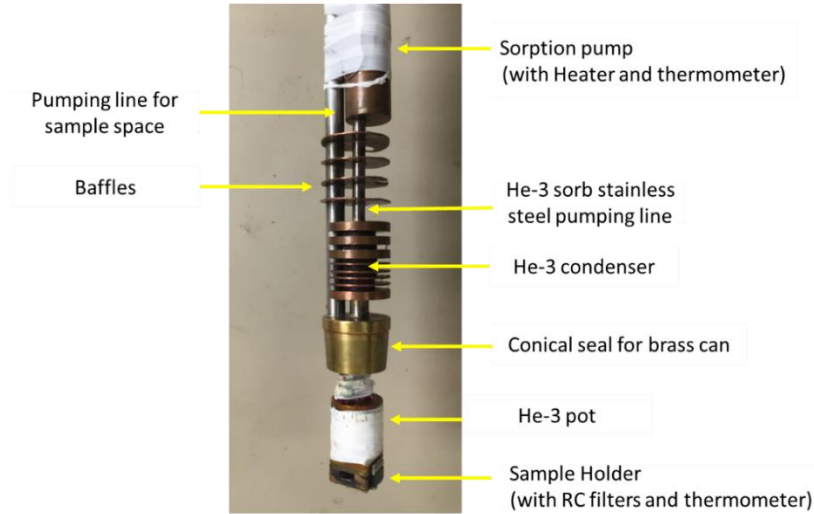**Figure 2.9: Components of the bottom end of the He-3 insert.**

2.3.2. Measurement setup
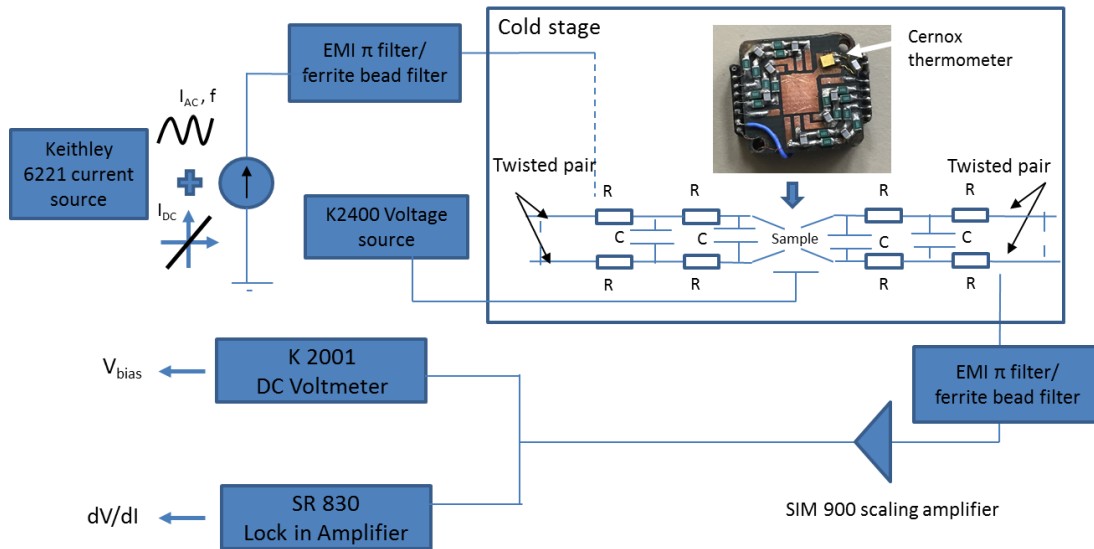
Figure 2.10: The typical setup used for low temperature measurement of differential resistance as a function of V_{bias} at different gate voltages.

i. For differential resistance measurements the device is ramped with a DC current riding on a small AC current (10 or 20 nA) at a frequency of 47Hz. The output signals from the sample is amplified using a SIM 900 scaling amplifier. The SR 830 lock in amplifier measures the voltage response to the AC current modulation that is used to calculate the differential resistance (dV/dI). The DC bias voltage across the source and drain leads (V_{bias}) is measured using a Keithley 2001 Voltmeter.

ii. The gate voltage is supplied by a Keithley 2400 voltage source.

iii. For superconductor DC IV measurements Keithley 6221 current source and Keithley 2001 voltmeter are used.

iv. Filters – Two stage cryogenic RC filters with a cutoff frequency of ~ 3 kHz are used close to the sample (on the sample holder as shown in figure 2.9). On the outside, at room temperature, EMI π filters and ferrite bead filters in series with RF chokes[4] are used.

2.3.3. Current annealing of suspended devices

Immediately after fabrication, suspended graphene almost always has some e-beam resist impurities that cannot be completely removed by solvents like acetone or resist strippers like Nano^{TM} Remover PG. Even very small amount of solvents and water can dope graphene. This prevents from observing the expected ballistic properties To remove such impurities the graphene channel is heated by passing a huge current through the device[60]. The heat desorbs the impurities in the channel. The technique works effectively for suspended graphene compared to graphene on SiO_2 since both sides of suspended sheet are free to desorb and there are no trapped impurities or heat dissipation through the substrate. Current annealing can heat the center of the suspended graphene strip to almost 600^{0}C or above [11, 12]. Generally, for the suspended samples described in the thesis current annealing is performed at 10K either in *He* gas flow or in vacuum environment. But for superconducting junctions current annealing in a vacuum environment, below T_c, produced the best results. Gate voltage V_g is kept at zero.

---

[4] The ferrite bead high frequency filters are built following the scheme by Brain D'Urso and Jim Mac Arthur at Harvard. The link for the recipe is
http://users.physics.harvard.edu/~coldwell/marcus/how_to/Ferrite_Bead_Filter.pdf

During the procedure, current is ramped through the sample from zero to finite values while measuring the voltage. If a reasonable change is noticed in voltage for a fixed current, then the current is held at that value for a while until no further changes are observed. Then its ramped back down to zero and a gating curve is obtained to evaluate the improvement. The process is repeated until best results (for mobility or mean free path) are obtained. The minimum current typically required for annealing is ~0.3mA/µm. Sometimes abrupt changes in the voltage happens during annealing due to an external impurity landing on the sample or other accidents. This can lead to an unexpected burning of the sample. In order to prevent these abrupt the compliance of the current source (Keithley 6221) is set to the minimum value and changed in increments when required, while ramping the current.

Chapter 3

Signatures of pseudo-diffusive transport in suspended ballistic graphene superconductor junctions[5]

In chapter 1 it was pointed out that the conductance of a pristine sheet of graphene, away from the Dirac point (DP), is proportional to the number of propagating modes in graphene. This fact breaks down close to the DP where the carrier density tends to zero. Theoretical calculations predict that pristine graphene displays unexpected "pseudo-diffusive" behavior in this regime [14], i.e., even in the absence of defects or impurities, the transport signatures near the DP resemble that of a diffusive conductor. The conductance should reach a universal, quantum limited value of $\dfrac{4e^2}{\pi h}$ [61]. The origin of these phenomena is the change in the nature of transmission of conducting channels. Near the DP, the transmission switches from propagating to evanescent mode. In a sufficiently wide ballistic graphene, unlike in normal metals, a sizeable number of evanescent modes can have finite transmission. At DP, these perfectly transmitting evanescent modes gives rise to the universal conductivity and a conductance proportional to the aspect ratio.

Pseudo-diffusive behavior has been observed in 2D photonic crystals and photonic lattices resembling graphene [62, 63]. In electronic transport a direct measurement of conductivity at DP is difficult due to the presence of electron hole puddles, even in the best of samples. But in graphene, the capability to tune the carrier density by using a gate electrode provides an opportunity to observe the 'transition' from ballistic to evanescent mode mediated pseudo diffusive transport. Transport signatures that are sensitive to changes in transmission of the

---

conduction channels, like shot noise and superconducting IV characteristics, are quantities that can be measured. Their density dependence in the 'evanescent regime' is expected to provide evidence to the transition. But several prevailing technical challenges prevented observations of this longstanding prediction.

This chapter discusses one of the first observations that indicate this transition. This was made possible by developing superconductor proximity induced suspended ballistic graphene with low potential fluctuations near charge neutrality point (CNP). The transition is observed when studying the junction's IV characteristics. When approaching the CNP ($n<10^{10}cm^{-2}$), where the evanescent mode transport starts to dominate over the conventional propagating modes, the multiple Andreev reflection (MAR) related features known as sub-harmonic gap structures (SHGS) become more pronounced. The product of normal resistance and excess current, ($I_{exc}R_N$), which remains constant at high carrier densities is also suppressed rapidly at low carrier densities near the CNP. Both observations are in contrast with previous experimental observations in disordered graphene superconductor junctions, where both SHGS and $I_{exc}R_N$ show no significant gate dependence. The results are in qualitative agreement with the theoretical predictions and provide strong evidence for pseudo-diffusive transport in ballistic graphene.

At the end of the chapter, a very fine scan of the Fermi energy (carrier density) in the vicinity of the CNP is presented, exploring the possibility of specular Andreev reflection related signatures.

3.1. Theoretical Background: The gate dependent transmission in pristine graphene

To understand the transition of ballistic to evanescent mode transport, Katsnelson [61] and Tworzydlo et al.,[64] calculated the transmission in pristine graphene as a function of the gate voltage. The derivation is summarized as follows. Consider a pristine graphene strip of width W in contact with leads separated by length L. The graphene underneath the two leads is assumed to be heavily doped (chemical potential μ_∞) with infinite modes. Then the energy states in the two leads can be written as $\mu_\infty \pm \hbar v_F \sqrt{k^2 + q_N^2}$ where k- longitudinal momentum. For the graphene strip in between the leads, the energy states are: $\mu \pm \hbar v_F \sqrt{\widetilde{k}^2 + q_N^2}$, where $\widetilde{k}$ - longitudinal momentum.

Here μ ($<<\mu_\infty$) is the gate tunable Fermi energy in graphene with $\mu=0$ representing the DP. For W>>L, the details of the graphene edge becomes insignificant[6]. Allowing the wave functions to disappear at the graphene boundaries, y=0 and y=W, the transverse momentum can be shown to be quantized as

$$q_n = \frac{\pi}{W}(n+\frac{1}{2}) \tag{3.1}$$

where n=0,1,2,3 –representing the modes in the graphene. Solving the Dirac equation and matching the solution at the leads, the transmission for each mode in graphene is given by

$$T_n = \left| \frac{\tilde{k}}{\tilde{k}\cos(\tilde{k}L) + i(\delta\sin(\tilde{k}L)} \right|^2 \tag{3.2}$$

with $\delta = \frac{|E_F|}{\hbar v_F}$. $\tilde{k} = \sqrt{\delta^2 - q_n^2}$ is real for $q_n<\delta$ and imaginary for $q_n>\delta$. Therefore the number of modes $N < \frac{E_F W}{\pi\hbar v_F}$ (lower order modes) the transmission are propagating and for $N > \frac{E_F W}{\pi\hbar v_F}$ (higher order modes) they are evanescent. The transmission probability as a function of $q_n L$ for different values of the dimensionless Fermi energy $\kappa = \frac{|E_F|L}{\hbar v_F}$ is shown in figure 3.1. The computation here was done for N = 1000 and W/L=9.

---

[6] It has been shown that for W/L<4 the transmission will depend on the detail of the graphene edges- armchair or zigzag.
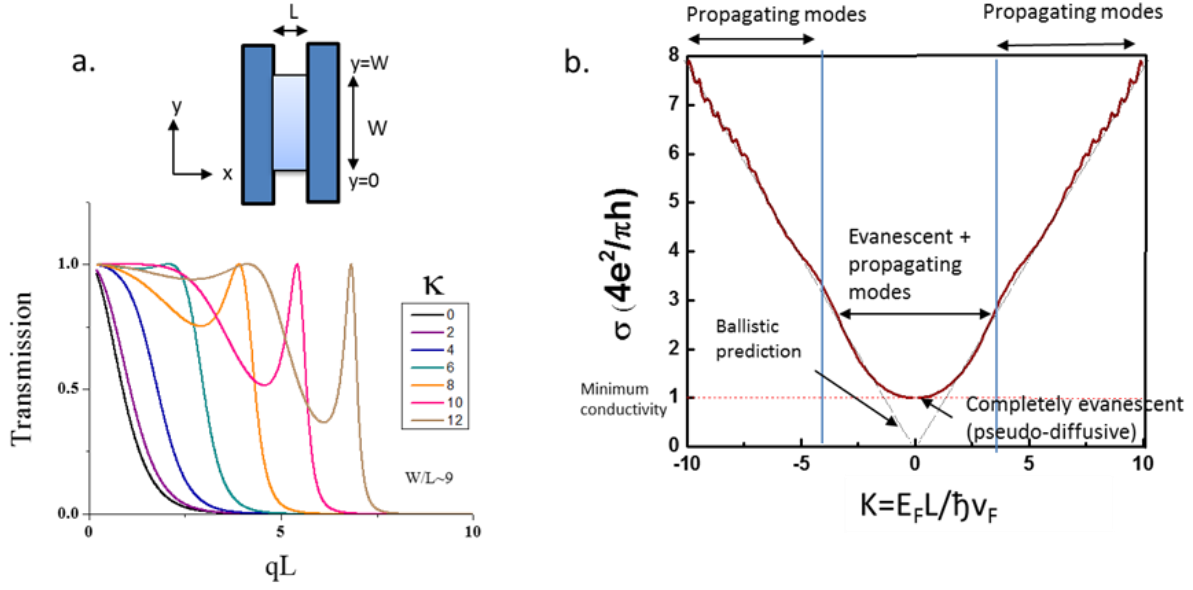
Figure 3.1: Ballistic and evanescent transport in graphene. a. Transmission as a function of qL for various $\kappa = \dfrac{|E_F|L}{\hbar v_F}$ (from equation 3.2) and **b.** Conductivity (σ) vs κ for a pristine graphene device. Dotted line is the naïve ballistic prediction due to propagating modes alone. Solid line is the expected curve by using transmission from equation 3.2 and the Landauer formula from equation 3.4.

For a fixed L, as $\kappa \to 0$ as $\delta \to 0$, higher order modes becomes imaginary and transport is carried by evanescent modes along with the lower order propagating modes. At the Dirac point $\delta=0$ ($E_F=0$) and all the modes are evanescent. The transmission probability at Dirac point for very large N is

$$T_n = \frac{1}{\cosh^2 qL} = \frac{1}{\cosh^2 n\pi L/W}; n = 0,1,2,..$$
(3.3)

This finite transmission is unlike non-relativistic charge carriers. For normal incidence i.e., when the $qL \to 0$, $T= 1$, confirming the absence of backscattering discussed in section 1.2.2[7].As long as

---

[7] This problem is identical to the inter band tunneling of relativistic fermions through a rectangular barrier (as discussed in chapter 5) with the left and right contact leads representing conduction band and the graphene representing the valence band. When the energy of the electrons are aligned close to the top of the barrier, the transport is evanescent

W>>L, close to the Dirac point a finite number of open evanescent channels exist and the conductance is calculated using the Landauer formula for

$$G = \frac{4e^2}{h} \sum_{n=0}^{N-1} T_n \rightarrow \sigma_0 \frac{W}{L} \qquad (3.4)$$

where $\sigma_0 = \frac{4e^2}{\pi h}$ is the quantum limited minimum conductivity. The conductance near Dirac point is dependent on sample dimensions as in diffusive metals. The fluctuations in electrical current (shot noise) near the evanescent regime are found to be enhanced with the gate dependent Fano factor

$$F = \frac{\sum_{n=0}^{N-1} T_n (1-T_n)}{\sum_{n=0}^{N-1} T_n} \qquad (3.5)$$

reaching 1/3 at Dirac point, another similarity with the transmission statistics in diffusive metals. This finite noise at Dirac point, without impurities or defects, is associated with the *Zitterbewegung* of ultra-relativistic Dirac particles[61].

3.2. Proposals and requirements for experimental observations of pseudo-diffusive electronic transport

Several longstanding theoretical proposals have been made as to how the pseudo-diffusive behavior can be observed in ballistic graphene devices. For this purpose, transport characteristics that are sensitive to the nature and distribution of charge transmission in the conduction channels should be considered. One straightforward way is to measure the shot noise and see how the Fano factor changes with the carrier density. At higher carrier densities the Fano factor is low (~0.1) as

and at Dirac point, pseudospin conservation makes the T=1. [58] C.W.J. Beenakker, Andreev reflection and Klein tunneling in graphene, (2007) 1-20.

expected in ballistic transport, but when close to the evanescent regime, as mentioned earlier, the Fano noise increases reaching the value of 1/3 at DP.

Transport in ballistic graphene (G)-superconductor (S) hybrid devices is also expected to show pseudo-diffusive signatures [14, 15, 65]. Relevant to the work here is the prediction by Cuevas *et al.in* [15]. They showed that in short ballistic SGS junctions the quasiparticle current-voltage characteristics such as excess current and SHGS amplitudes should display a strong Fermi energy or carrier density dependence near Dirac point, reflecting the crossover from ballistic to pseudo-diffusive charge transmission. Previous (experimental and theoretical) work using superconductor point contact break-junctions (S-S, S-Insulator-S etc.,) have confirmed the sensitivity of SHGS amplitudes to individual transmission of the channels in the point contact. In the experimental work the number of channels and their transmission were controlled by adjusting (breaking) the contact[66]. But here, in graphene, by using a gate electrode to tune the Fermi energy we can control the number of channels and their transmission into the evanescent regime. This leads to a direct insight of an intrinsic property of graphene's energy spectrum!

In realizing these predictions, the experimental work carried out so far [18-20, 67, 68], has been impeded by numerous technical challenges. To reach the energy scale required for evanescent transmission, the Fermi wavelength $\lambda_F = \dfrac{hv_F}{E_F}$ should approach the dimensions of the sample.

Here $v_F \approx 10^6$ m/s is the energy independent Fermi velocity and E_F is the Fermi energy. Therefore the potential fluctuations (δE_s) near CNP should be small, a few meVs, even for a sub-micrometer long channel. In addition, charge carrier scattering should largely be eliminated, so that the transmission of the carriers reflects the intrinsic nature of the transverse modes. This requires the devices to be ballistic. Due to the strong substrate-associated disorder, previous observations were marred by the presence of large potential fluctuations and short mean free path (usually <<100 nm) due to the SiO$_2$ substrate (see section 1.3.3). More recently, graphene/h-BN hetero-structures have demonstrated ballistic transport [69]. Josephson current has also been observed in these structures when coupled with superconductors [23, 24]. However, with these methods achieving both very low carrier density and highly transparent S-G interfaces is still under development.

3.3. Experimental methods and sample characterization

In order to meet the requirements to explore the pseudo-diffusive regime near DP the fabrication method as explained in Chapter 2 was developed. Here the important details are presented. The graphene was deposited using mechanically exfoliated highly oriented pyrolytic graphite (HOPG). The graphene channel was designed to have a large aspect ratio (*W/L*) ~9 with width *W* =5.5μm and length *L* = 0.6μm. Such geometry minimizes any effect from the edges of graphene and complies with the theoretical prescription $W/L \geq 4$ [64]. Moreover, a larger *W/L* improves experimental observation by allowing more evanescent modes (large higher order N) to contribute to the conductance. To suspend graphene an etch-free method as outlined in chapter 2 and previous work is used[70]. The contacts were formed by electron beam evaporation of Ti and Pd to form a thin buffer layer ~2nm followed by DC magnetron sputtering of ~60 nm Niobium (T_c~9K, Hc_2~3.5 T). The *Ti/Pd* buffer layer helps in achieving a low contact resistance. The sputter conditions and device geometry are determined to minimize the stress on graphene. This is essential for a transparent superconductor- graphene interface and also improves the chances of getting a ballistic graphene channel by current annealing. All the measurements were performed in an Oxford Instruments VTI refrigerator and the He-3 insert (see Chapter 2, section 2.3), with room temperature ferrite and π-filters, and cryogenic 2-stage RC filters

The gating curves of the device after current annealing measured for two different temperatures, 9K (~ *T_c*) and 1.5 K, are presented in figure 3.2(b). At *T*~9K the device shows a maximum mobility of >250,000 cm^2/Vs and the mean free path is sample length limited. From the smear at the CNP and using QH measurements (see below) to establish the relation between *n* and *V_g* (see below), the minimum carrier density is $n_s \sim 1.4 \times 10^9$ cm^{-2}. This corresponds to a potential fluctuation δE_S~ 4.4meV at CNP, the smallest value observed so far in such devices. To characterize the Fermi wavelength, similar to Ref.[15], a dimensionless parameter $\kappa = \dfrac{E_F L}{\hbar v_F} = \dfrac{2\pi L}{\lambda_F}$ is used. Therefore the maximum δE_S~ 4.4meV in our sample corresponds to κ~4.0. The resistivity at CNP is $\sim 19 k\Omega = 0.93 \dfrac{\pi h}{4e^2}$. The small discrepancy from the theoretical value of $\dfrac{\pi h}{4e^2}$ may be attributed to the presence of electron hole puddles and finite Coulomb scattering which in practice cannot be completely avoided. The excellent quality of the device is also evident from the QH

measurements. As shown in figure 3.2(c), at T=1.5K, and in a low magnetic field of B= 300mT, pronounced magneto-oscillations are already observed. At B=500mT, the sample displays fully developed anomalous QH plateaus at the expected filling factors $v=\pm2,\pm6,...$ for monolayer graphene. From these QH plateaus, the carrier density (n)-gate voltage (V_g) relation is found to be: $n=1.84\times10^{10}\times\left(V_g-V_{NP}\right)$[Volt] cm^{-2} where $V_{NP}=-0.9$V is the gate voltage at CNP. This is consistent with the estimation using the geometrical capacitance considering 285nm SiO$_2$ in series with 220nm (thickness of the PMMA spacer) of vacuum. On the higher mobility electron side, additional oscillatory features in resistance, R (V_g), at v=1,4,8... , etc. are observed which may be attributed to the onset of broken symmetry. The resistance at the CNP displays diverging behavior with increasing field, starting at a low B~0.3T. All these observations demonstrate that the sample is of extremely high quality, with long mean free path and minimal potential fluctuations.

Next, we study the superconducting proximity effect at T=1.5K in the absence of magnetic field. Compared to T>T_C, the junction resistance is significantly reduced. For $V_g-V_{CNP}>0.3$**V** , the resistance vanishes reflecting the presence of a finite supercurrent. Figure 3.2(d) shows the differential resistance $\frac{dV}{dI}$ as a function of bias voltage (V_{bias}) taken at $V_g-V_{CNP}=7.5$**V** (κ~39). From the curve we obtain the superconducting gap on graphene (Δ) ~0.34meV. This value is significantly smaller than the BCS gap of Nb, $\Delta_{\mathbf{BCS}}\left(0\right)\sim1.764k_BT_c\sim1.37$**meV** , and varies slightly from sample to sample. Similar reduction has also been observed in superconductor-nanowire weak links [71, 72] and can be attributed to the impact of the finite-thickness of Ti/Pd buffer layer. At finite $V_{bias}\ll2\Delta$, the resistance drops down to ~ 40% of the normal resistance (R$_N$) due to superconducting proximity effect. Evaluating the value of the normalized excess current $I_{exc}R_N\sim0.4$mV $\sim\Delta/e$ and using the OTBK model [57] we estimate the dimensionless barrier strength of the interface, Z ~0.5. The SHGS are very weak, consistent with the theoretical prediction for ballistic channels with high transmission [73, 74]. Other factors that may affect the weak SHGS include the small induced superconducting gap and the relatively high measurement temperature.
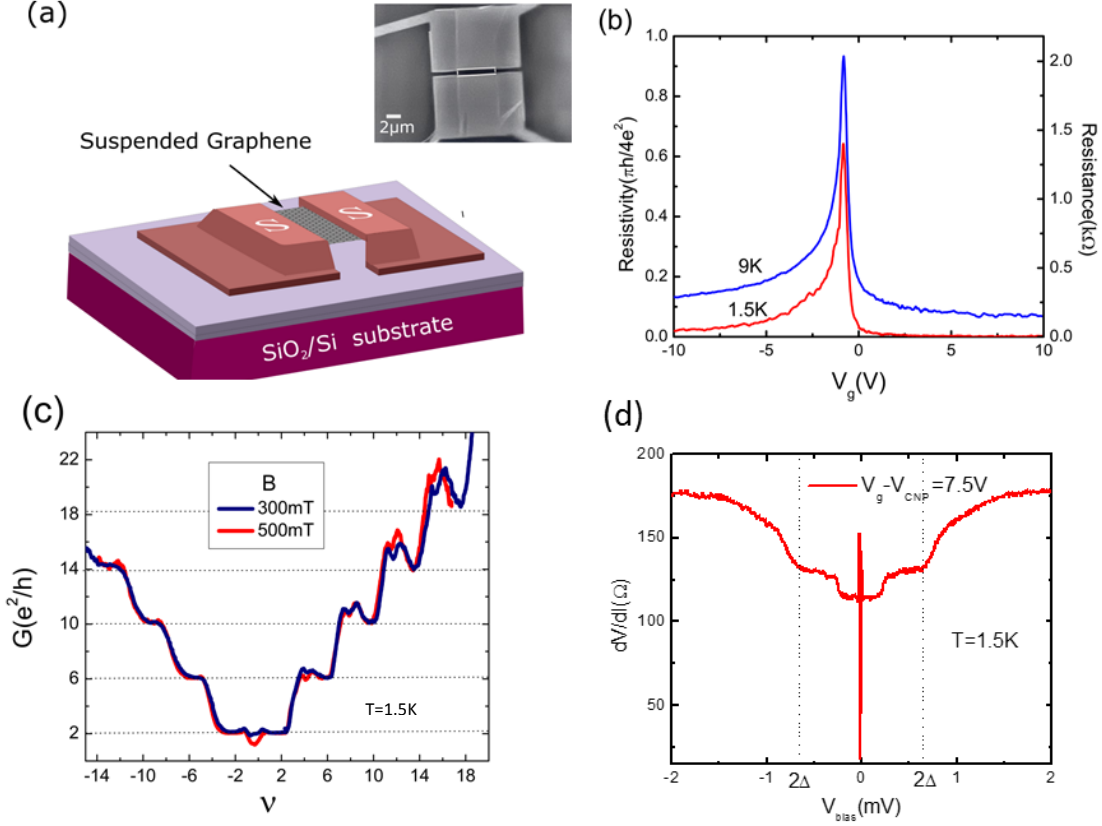
Figure 3. 2: **Device characteristics: a.** Main panel: Device schematics. Inset: SEM Image of the device. Scale bar is 2μm. The graphene channel is highlighted by the open rectangle **b.** Resistivity in units of (πh/4e^2) as a function of gate voltage (V$_g$) at T=9K (blue) and T (<T$_C$) =1.5K (red). **c.** QH measurements: Conductance versus filling factor for two different magnetic fields 300mT (blue) and 500mT (red) at T=1.5K. **d.** Differential resistance as a function of bias voltage (V$_{bias}$) at T=1.5K. Gate voltage is 7.5V away from the CNP gate voltage (V$_{CNP}$). The corresponding κ ~39(see text) and the induced gap (Δ) =0.34meV.

Now we focus on the behavior of the differential resistance as we approach the CNP. Figure 3.3 (a) shows the normalized differential resistance $\dfrac{1}{R_N}\dfrac{dV}{dI}$ as a function of V_{bias} obtained at various gate voltages. When $V_g - V_{CNP} < 0.6\text{V}$ ($n < 10^{10}\,\text{cm}^{-2}$ and $\kappa < 9$), the differential resistance curve starts to develop a pronounced dip at $V_{bias} = 2\Delta/e \sim 0.68\text{mV}$. As the V_g is ramped further towards the CNP, i.e., for $V_g - V_{CNP} < 0.3\text{V}$ ($n < 5.7\times10^9\,\text{cm}^{-2}$ and $\kappa < 5.5$), while the dip at $V_{bias} = 2\Delta/e$ continues to be deeper, other SHGS start to emerge at low V_{bias}. All the observed

47

features appear at $V_{bias} = \pm 2\Delta/ne$ where $n=1, 2, 3...$ as expected for MAR processes and their positions in V_{bias} are independent of V_g. The higher order features are within noise. The observed features are sharpest at CNP where the SHGS at $n=1, 2$ and 3 are all easily resolvable. But once V_g is ramped to the hole side, slightly away from the CNP (κ~ -1.9), the SHGS begin to weaken. The dip at $n=1$ shows the most prominent response to the gate voltage. In conjunction with the appearance of the pronounced SHGS, the overall shape of the normalized differential resistance curve transforms from a "V"-shape to a shallow profile. We note that the observed gate-dependence of the $\dfrac{dV}{dI}$ versus V_{bias} curves is specific to superconductivity. Above T_c the "background" $\dfrac{dV}{dI}$ versus V_{bias}, within the bias voltage range studied here, shows roughly no curvature.
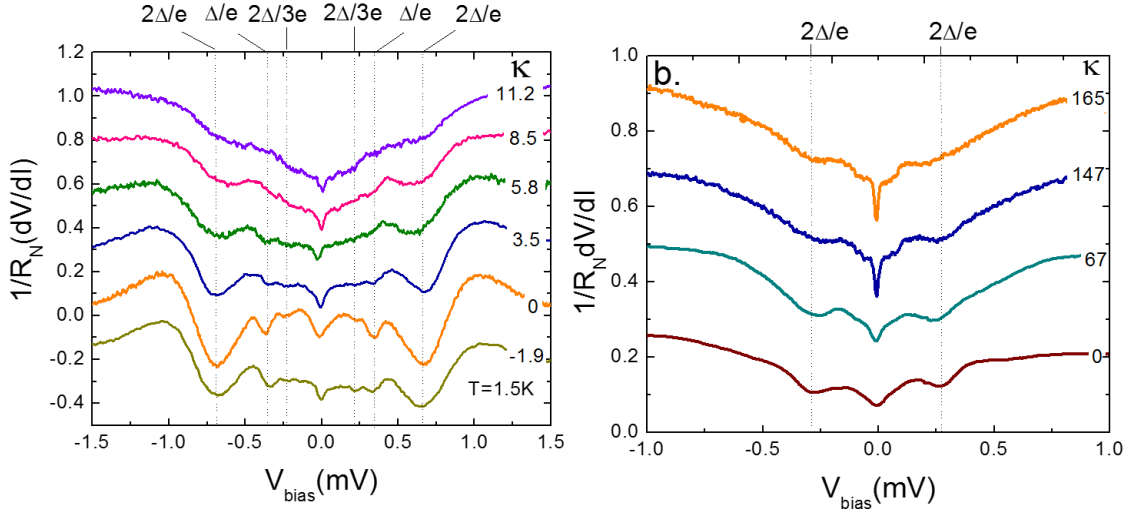
Figure 3.3: Normalized differential resistance $\dfrac{1}{R_N}\dfrac{dV}{dI}$ versus bias Voltage (V_{bias}) for different

$\kappa = \dfrac{E_F L}{\hbar v_F}$. Individual curves are shifted for clarity. Dotted lines indicate SHGS. **a.** Ballistic SGS: Ti/Pd/Nb contacts at T=1.5K. Evolving SHGS at $V_{bias}=\pm 2\Delta/ne$ for n=1, 2 and 3 where 2Δ=0.68meV.**b.** Diffusive SGS: Ti/Pd/Nb contacts at T=1.5K. Unchanged Gap feature at $V_{bias}=\pm 2\Delta/e=\pm 0.3$mV.

For comparison, we present a similar set of data for diffusive samples with Ti/Pd/Nb (Figure 3.2 (b)) contacts. In the diffusive case, graphene channel sits on SiO_2 and has a mean free path $l_m \ll L$ and $\delta E_F \sim 40\text{meV}$. In contrast to the ballistic sample, there is no significant gate voltage dependence of the SHGS disordered devices for a large range in κ. The results are no different from previous work on diffusive graphene samples with Ti/Al-contacts (see [20]). We note that the higher order SHGS are unresolvable in the diffusive Ti/Pd/Nb device, which may be attributed to the smaller induced superconducting gap and the relatively high measurement temperature.

To understand the observed gate-dependent SHGS, we consider the Fermi energy modulation of charge transmission in a ballistic graphene device in figure 3.1. In general, the transmission of Dirac electrons in graphene can be described by a summation of contributions from the boundary-defined transverse modes, each satisfying the Dirac-Weyl equation. At high densities, the channels in the ballistic graphene strip are propagating with high transmission. Approaching the CNP, however, the propagating modes become suppressed and the evanescent modes contribute increasingly to the conduction with more channels having a lower transmission. With superconducting contacts, it has been shown that the oscillatory amplitude of the SHGS increases due to the contribution from the low-transmitting channels [15, 73]. As a result, close to the CNP where evanescent modes with low transmitting probability dominate, the SHGS are more pronounced than at large gate voltages. The stronger gate-dependence of lower order SHGS, especially n=1, is also consistent with the theory. This is because compared to the higher order SHGS, the lower order ones are formed by Andreev quasi-particles that traverse the graphene channel fewer times and hence involves more contribution from the low transmitting channels.
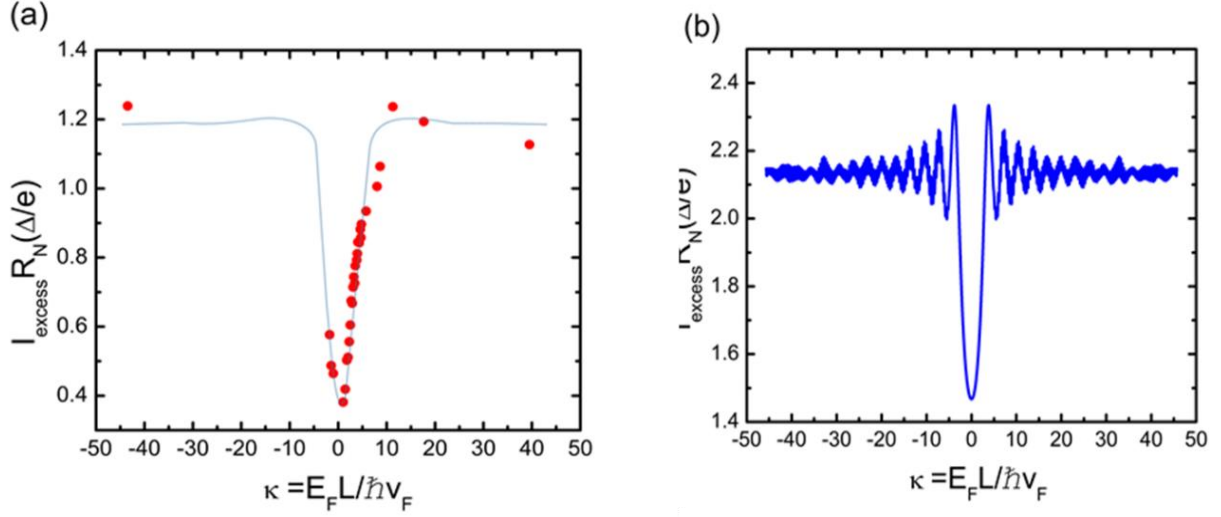
Figure 3.4: Normalized Excess current ($I_{exc}R_N$) as a function of $\kappa = \dfrac{E_F L}{\hbar v_F}$ a. Experimental data: $I_{exc}R_N$ is calculated from the current-voltage characteristics of the device for different V_g at 1.5K.The (blue) line is drawn as a guide to the eye. **b.** Theoretical calculation**:** for short ballistic SGS junction with W=5.5μm and L=0.6μm at T=0K.

A quantitative comparison with the theoretical predictions for pseudo-diffusive transport can be made by characterizing the excess current through the SGS device. Generally in a SNS junction when $eV_{bias} \gg 2\Delta$, the current though the sample consists of a normal 'Ohmic' current (I_N) and an 'excess' current (I_{exc}) due to the superconducting proximity effect. Compared to the Josephson current, excess current is much more robust against the influence of the electromagnetic environment, and hence provides a reliable parameter for characterizing the proximity effect. In SGS junctions the abundance of nearly ballistic modes at large Fermi energies leads to large excess current. However, in the vicinity of the CNP the number of highly transmitting propagating modes decreases and the charge transport becomes increasingly evanescent thereby decreasing the excess current. Figure 3.4 (a) shows the normalized excess current $I_{exc}R_N$ in our device (extracted from current-voltage curves at various gate voltages) as a function of κ. For κ >9, i.e., in the ballistic transport regime $I_{exc}R_N \sim 0.4$mV$\sim 1.2\Delta$/e whereas for κ <9, there is a clear gate dependence. The excess current sharply reduces when approaching the CNP. This reduction coincides with the onset of the enhanced SHGS as shown in figure 3.3 (a). For short ($\dfrac{\hbar v_F}{L} > \Delta$) ballistic graphene Josephson

junctions, the transmission dependence of the excess current been theoretically studied in reference [15]. With L=0.6μm, $\frac{\hbar v_F}{L} \sim 1meV$ and since the induced gap $\Delta \sim 0.34meV$ our device marginally satisfies the short junction limit. The observed gate modulation of normalized excess current is in qualitative agreement with the zero temperature theoretical calculation as shown in Figure 3.4 (b). Using W=5.5μm and L=0.6μm of our sample and following the result in [15], the total excess current in a short Josephson junction is calculated as a sum of its individual contribution from all the transverse modes, each determined by the corresponding transmission coefficient T_n.

$$I_{exc} = \sum_n \frac{2e\Delta}{h} \frac{T_n^2}{1-T_n} \left(1 - \frac{T_n^2}{2(2-T_n)\sqrt{1-T_n}} \ln\left(\frac{1+\sqrt{1-T_n}}{1-\sqrt{1-T_n}}\right)\right) \tag{3.6}$$

The discrepancy between the theory and our observation, especially in the values for normalized excess current, may be attributed to a few factors. First, the theory assumes an ideal SN interface (Z=0), whereas in our device Z~0.5. Secondly, our measurements were carried out at a base temperature of ~ 1.5K while the theory does not consider a finite temperature. Both these factors contribute to the reduction of the normalized excess current. In addition, for lowest values of κ, the theory does not consider the presence of the electron hole puddles that exists in real devices. These, together with temperature smearing, can we explain the slight broadening in the excess current dip with an onset at κ~9 compared to the theory (κ~4).

An imperfect SG interface that may also result in Fermi energy modification of transmission coefficients without any direct consequence of the Dirac fermionic nature of graphene. Indeed it has been suggested that in graphene-metal junctions, the doping of the metal contacts can extend into graphene, forming a *p-n* junction that imposes the charge carrier reflections [75, 76]. A direct evidence of the presence of such interfacial *p-n* junction is the electron-hole asymmetry in the *R* vs. V_g dependence. As the gate voltage is swept across the CNP, the S-G interface changes from *p-n* to *n-n* and the asymmetry in the *R* vs. V_g dependence can be associated with the transmission probability across the S-G junction. While the presence of such junctions may affect the SHGS and I_{exc}, the gate voltage dependence will be gradual with no particular energy scale. In addition, such contact-doping associated reflection should give rise to

asymmetry in the quasi-particle current-voltage characteristics that persists up to large gate voltages on both the electron and hole sides[24]. These are apparently not consistent with the observation of a sharp dip on the $I_{exc}R_N$ vs. E_F dependence for $E_F<8meV$, and the qualitatively symmetric behavior with respect to the CNP.

3.4. Probing specular Andreev reflection

Applying Dirac BdG equation for the S-G interface, Beenakker[13] showed that when approaching the DP the switch from retro Andreev reflection (r-AR) to specular Andreev reflection (s-AR) will be marked by an inversion in the bias dependence of the sub gap conductance-$(1/G_N)\ dI/dV$. The results are plotted in figure 3.5(a). The plot for $E_F/\Delta=10$ shows the typical conductance enhancement due to r-AR when eV_{bias} is below the gap. A contrasting feature is seen for the s-AR curves at $E_F/\Delta = 0.2, 0.4.., 1.4$. In the s-AR regime (i.e., $E_F \sim \Delta)$, when eV_{bias} is close to E_F, there is a dip in $(1/G_N)\ dI/dV$ which reaches zero at $eV_{bias}=E_F$. This is because when $E=eV_{bias}=E_F$, the reflected quasiparticle has to be at the DP (compare with illustration in figure 2.5 in Chapter 2). This is not possible and therefore the AR probability vanishes. Figure 3.5(b) shows the 2D plot of $(1/G_N)\ dI/dV$ as a function of $(V_{bias},\ E_F/\Delta)$.

In experiments studying s-AR, the feature to look for is the sudden appearance of a sub gap peak (dip) in the differential resistance (conductance) that is distinguishable from the MAR features when $E_F\sim\Delta$.

With the high quality sample and low potential fluctuations at Dirac point of the order of the gap, it is reasonable to expect signatures for specular Andreev processes to also appear in the SGS sample presented here. In order to explore this, $\dfrac{dV}{dI}$ vs V_{bias} was measured by a very fine scan in gate voltage close to the Dirac point. The 2D version of the experimental data is shown in figure 3.6. Each curve that make up this plot is measured at gate voltage increments of 0.005V (Δn $=9.2\ x\ 10^{-7}\ cm^{-2}$). For the sample area of 2.5μm^2, the number of electrons in graphene changes from 100 to 40 and each gate measurement adds 2 electrons. In the low bias regime, when $E_F<2.7meV$, (in the range of $0\leq V_g-V_{CNP}\leq0.02V$) an anomalous peak emerges. This peak cannot be associated with those accompanying higher MAR processes. So there is a possibility that the peak might be related to the onset of s-ARs.

There are several factors that need to be considered in confirming this claim. For example, the gap $2\Delta = 0.67meV$ is smaller than the E_F values for which the peak is observed. The peak is weak for Vg> 0.02V and there is no clear sign of it moving out towards higher bias, like in the theoretical plot 3.5(b). But the theoretical calculations are for SG devices and the devices measured here are SGS samples. So finite interference from MAR processes cannot be excluded. The thermal smearing of E_F/Δ for T=1.5K will also play a role in this energy regime. Also the plots in figure 3.5, based on [13], assume a step like pair potential at the SG interface. This is not the case in real devices. More theoretical calculations for SGS junctions, accounting for a smoother change in pair potential across the interface and MARs is required to make a clear comparison of the observations.
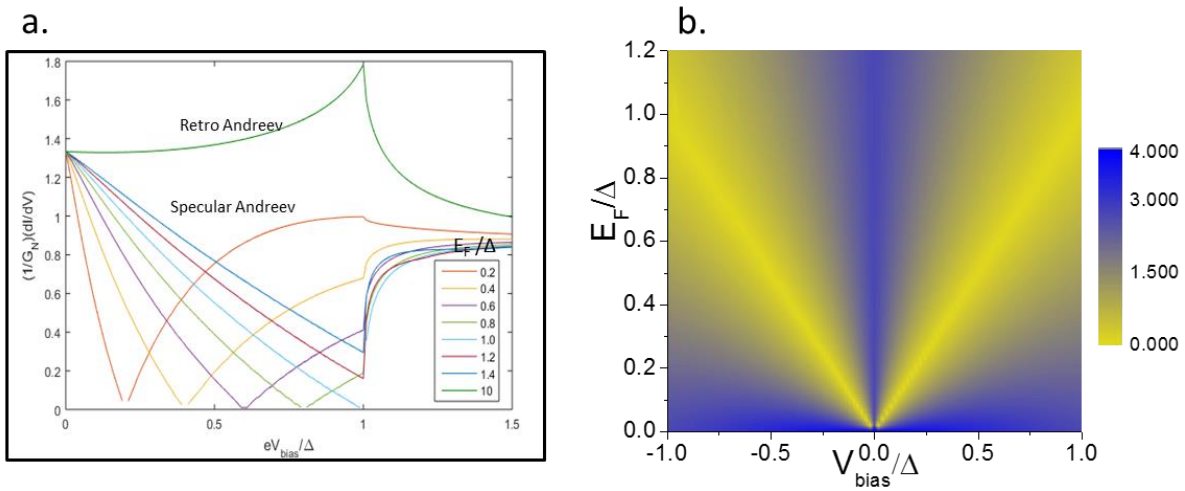
Figure 3.5: Differential conductance curves for specular Andreev reflection at a superconductor-graphene junction –Plots based on theoretical calculations in [13] for T=0K: a. Contrast between differential conductance for specular and retro Andreev reflections: Green curve (E_F/Δ=10) represents retro. For $E_F/\Delta \leq 1$, the curve flips due to specular Andreev reflection. **b.** Differential conductance vs. V_{bias} and E_F.
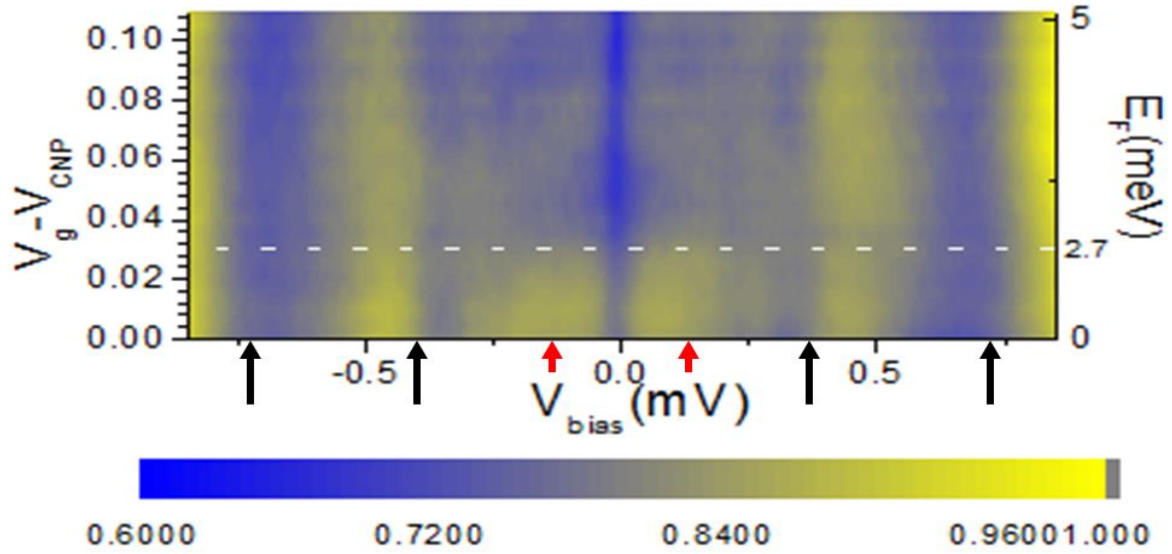
Figure 3.6: Differential resistance vs. V_bias for E_F≤5 meV at T=1.5K. Below the white dotted line additional peaks appear at low bias (indicated by red arrows). This does not follow the harmonics of MAR dip-peak structures (indicated by black arrows).

Chapter 4

Magneto transport in type II superconductor – graphene Josephson weak links

4.1. Introduction and motivation

Long before the discovery of graphene, it has been predicted that a proximity induced 2DEG system under a magnetic field can show unconventional QH plateaus due to the presence of Andreev bound states at the Superconductor-Normal (SN) interface[22]. These predictions hitherto remain unconfirmed. The ability to fabricate ballistic Superconductor-Graphene (SG) devices as seen in the last chapter and several other advances in fabrication of ballistic graphene devices[50] adds a new dimension to this research with interesting possibilities that may arise when merging ultra-relativistic physics with superconductivity. Induced superconductivity in the chiral edge states in graphene can also be used to detect valley polarization[17]. Also, more recently, it has been predicted that s –wave proximity induced superconducting low dimensional materials with large spin orbit coupling (SOC) and Zeeman split energy spectrum can host Majorana bound states [77]. Although graphene has a weak SOC, recent advances in fabrication has increased hope in engineering devices that can support spin polarized edge states. These edge states when coupled with a superconductor can form topological superconductors for observing Majorana modes and even other exotic non-abelian states in the fractional QH regime[16].

Several experiments have been reported in the last decade that studied induced superconductivity in the QH regime, but still a 'clear' evidence for the existence of Andreev edge states and enhanced QH conductance plateaus is lacking [23, 78-80]. In these experimental work type II superconductors are used as they have higher upper critical fields. Although the reasons are not clear at this stage, one of the common features in type II Superconductor hybrid devices with thin buffer normal metal layers between the S and N (like *Ti, Pd* in the previous chapter) is the

presence of a reduced superconducting gap. This can be due to the reverse proximity effect near the superconductor or minigap in N due to the presence of Andreev bound states. In AR, since the incident/reflected quasiparticles follow the same trajectory on the normal side of the interface and do not enclose a flux, they are immune to any phase breaking effect by magnetic fields. But an interesting situation was proposed to occur [81, 82] due to screening currents that form in the superconductor in a magnetic field. Screening currents are composed of a moving Cooper pair condensate. At the SN interface, in order to accommodate this Cooper pair momentum on the S-side, the incident and Andreev-reflected quasiparticles acquire a momentum shift. When the applied magnetic field is sufficient that the associated energy shift is comparable to the superconducting gap at the SN interface, AR probability becomes significantly suppressed, thereby weakening the proximity enhanced conductance. This so called "Doppler shift" effect is significant when the effective superconducting gap near the SN interface is small. Experimentally, the effect of screening currents on proximity-induced superconductivity has been studied in Niobium/2DEG junctions [83]. Here, at fields of ~ 200mT, the AR probability is completely suppressed. The suppression was accounted for by considering the effect of diamagnetic Meissner currents in the superconducting leads.

But in thin film superconductors vortex currents are more dominant than Meissner current[84] . The arrangement of vortices is highly dependent on how the field is introduced and ramped through the superconductor. But so far no experimental work has studied the impact of vortices and their distribution on the proximity effect. In this chapter, magneto transport in NbN superconductor - non suspended graphene weak links is presented, where the role of the vortices on the suppression of the proximity effect is revealed. This is achieved by employing a variety of magnetic field ramping techniques and studying their effect on the SGS IV characteristics. Using these techniques the suppressed proximity effect is retrieved at magnetic fields, where QH edge states are expected to emerge in ballistic graphene (500mT-1T). At the end of the chapter, a possible qualitative explanation of these observations is presented within the Doppler-shift framework.

4.2. Device fabrication and characteristics

This chapter deals mainly with non-suspended graphene Josephson weak links. The details of the device fabrication is presented in detail in Chapter 2. For the sake of continuity, some of the important aspects of the fabrication procedure is presented here in short.

Graphene-superconductor weak links (SGS) are fabricated on SiO_2/Si substrates, through standard mechanical exfoliation and e-beam lithography. For a highly transparent S-G interface, a buffer layer of *Ti* (2nm)/*Pd* (1.5nm) is thermally (e-beam) evaporated onto the contact area in a UHV environment (base pressure ~2 $\times 10^{-8}$ Torr). Immediately after the evaporation and without breaking vacuum, superconductor *NbN* is deposited onto the samples via DC magnetron sputtering. This reactive DC Magnetron sputtering is carried out in *N₂/Ar* environment. The buffer layers are essential to protect graphene from damage during sputtering and reduce the contact resistance of the interface. The sputter conditions and the lead geometry are chosen to minimize the stress on graphene. The current and voltage pair leads are split close to the contact point on the graphene channel to minimize the contribution of contact resistance especially above T_C. Typical graphene channels are of *L~0.5μm* in length and *W~1.5-10 μm* in width as shown in figure 4.1(a) and 4.2 - left inset. All devices are measured in a He-3 refrigerator, equipped with room temperature EMI ferrite beads and π-filters, and cryogenic 2-stage *RC* filters. The mobility of the graphene channel is estimated to be 5000-6000cm^2/Vs from gating of the two-terminal resistance (Figure 4.1(c) just below the transition temperature of the *NbN* leads (T_c ~ 11K) and the mean free path is calculated to be ~ 50-60nm. The zero-bias resistance below T_c, drops rapidly with decreasing temperature and reaches zero at *T~1-2K*, and the *IV* curves at *T=0.4K* in Figure 4.1(b) clearly show the existence of critical current I_C~75nA . In some of the wider samples which show large I_C ~1uA (Figure 4.2 right inset) at sub-kelvin temperatures a very sharp, equally spaced oscillations in the differential resistance (*dV/dI*) vs bias voltage (*V$_{bias}$*) is observed. This might be due to self–induced Shapiro steps (Figure 4.2) and has been also observed in other experiments[85]. All these features demonstrate a transparent S-G interface.
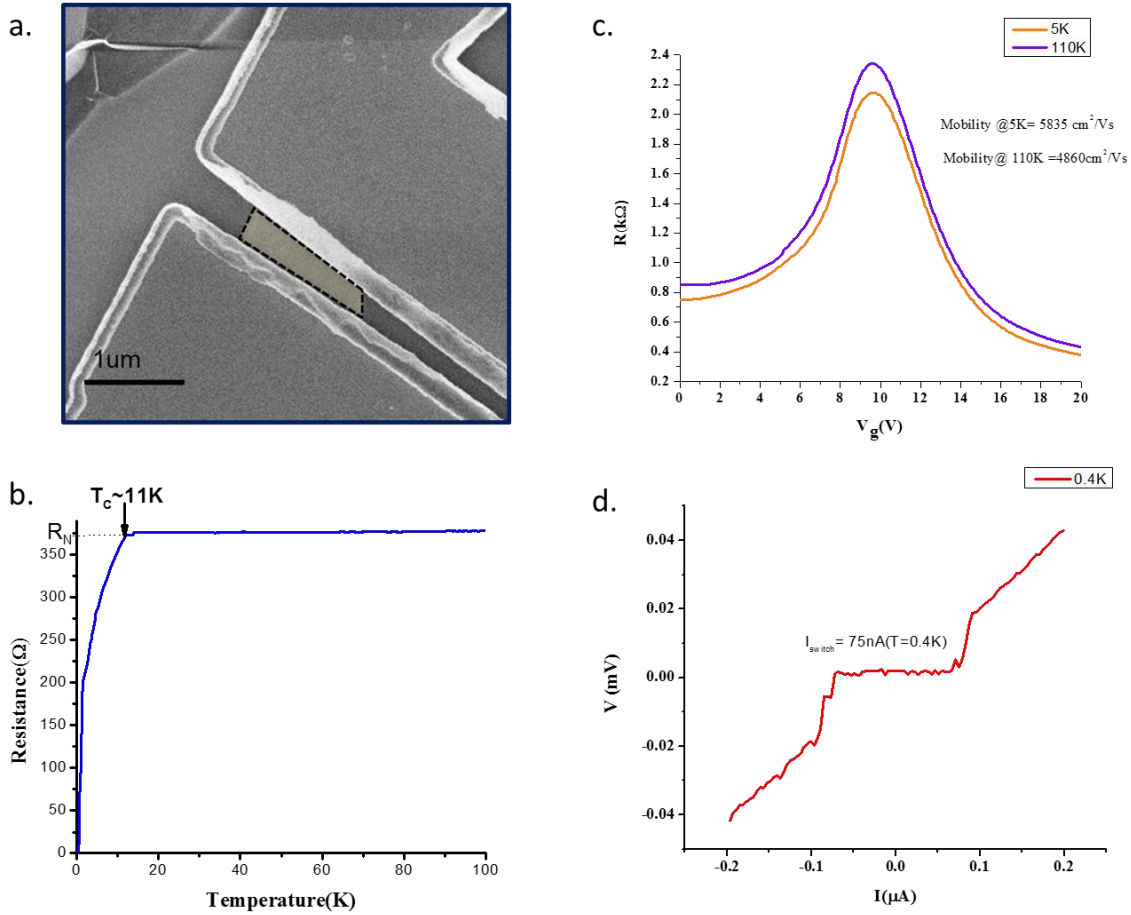
Figure 4. 1: Properties of non-suspended NbN-graphene Josephson weak link a. SEM image of the device. The graphene channel is highlighted. Scale bar is 1 μm. **b.** Resistance (R) vs. temperature of the SGS junction showing $T_c=11K$. **c.** Gating curves R vs V_g at 5K and 110K. **d.** Current Voltage (IV) charactersitcs of the junction at 0.4K. The switching to critical current I_C is ~ 75nA. T~0.4K.
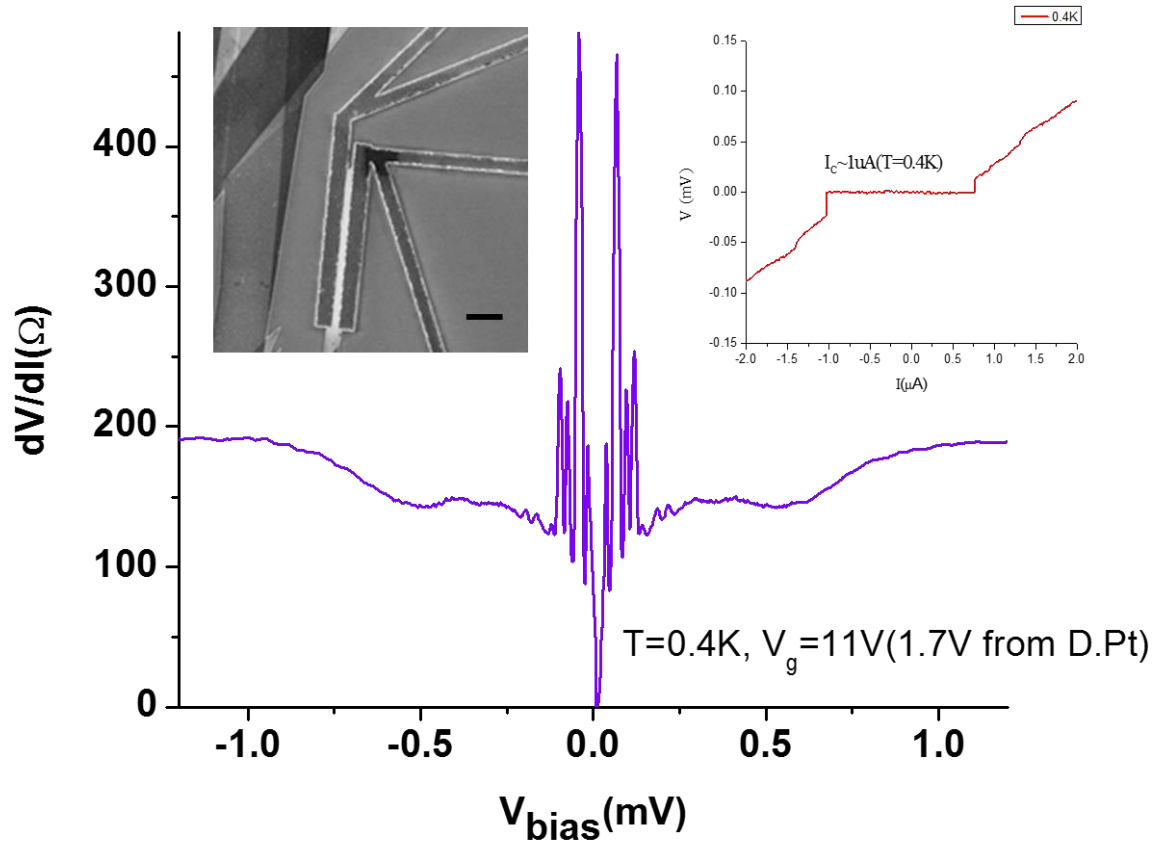
Figure 4. 2: Differential resistance (dV/dI) vs bias voltage (V$_{bias}$) of a 10 μm wide graphene-NbN Josephson junction. (left inset) SEM image of the device. Scale bar is 2μm. (right inset) Current-Voltage (IV) characteristics showing I_c~ 1uA. T~0.4K.

At T=0.4K, a clear evidence of multiple ARs (MARs) in *dV/dI* vs. *V$_{bias}$* curves is seen, as shown in figure 4.3. Here a conductance enhancement is observed when bias voltage is less than ~1.5mV. At lower bias voltages sub-harmonic gap structures are observed, where the valleys of the oscillations agree well with the expected MARs at $V_{bias} = \frac{2\Delta}{ne}$, with Δ=0.15meV (figure 4.3 bottom right). As in the last chapter, the gap Δ at the metal-graphene interface is sample dependent but is always much less than the bulk gap of *NbN* (from BCS theory Δ(0)=1.764*k$_B$T$_c$~1.8 *meV* for 11K).
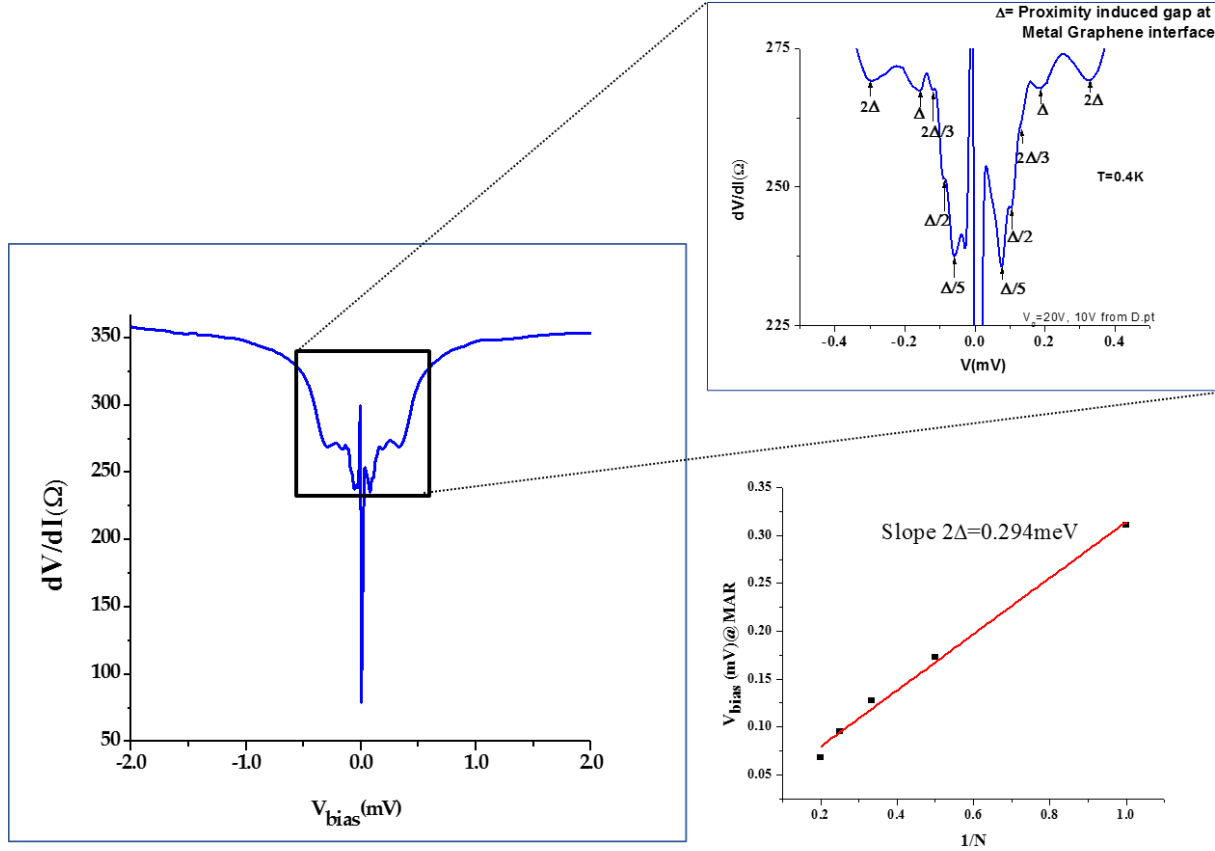
Figure 4.3: Multiple Andreev reflections in NbN-graphene Josephson weak links. (left) Differential resistance (dV/dI) vs bias voltage (V_{bias}) at T=1.5K (top right) Plot zoomed in to show MAR related resistance dips at V_{bias}=2Δ/ne (bottom right) V_{bias} -MAR dips vs 1/N where N-integer with a linear fit to extract the gap 2Δ=0.294meV.

4.3. Magnetic field measurements

For the magnetic field measurements first, the typical zero-field-cool (ZFC) procedure is used where the sample is cooled below T_c and then the magnetic field B is monotonically ramped up to the desired values. The data presented here is taken at a gate voltage of 10V from the Dirac point. For each B, the bias dependence of the differential resistance is measured. The ZFC- ramp up *dV/dI* normalized by the normal resistance (R_N) of the junction slightly below T_c. *($1/R_{N)}$(dV/dI)* vs V_{bias} is shown in figure 4.4. The measurements are performed at a stable temperature of T=1.5K. For B=0, R_N drops by 25% at V_{bias}=2Δ. Since both supercurrent and the oscillatory MARs features become completely suppressed under a very small magnetic field of ~1mT, the SGS junction can

be treated as two separate SG junctions with single AR at the interface. Further increasing the magnetic field, the AR enhancement of conductivity is rapidly suppressed and eventually vanishes around B=200mT. Above 200mT the dV/dI remains flat at R_N.
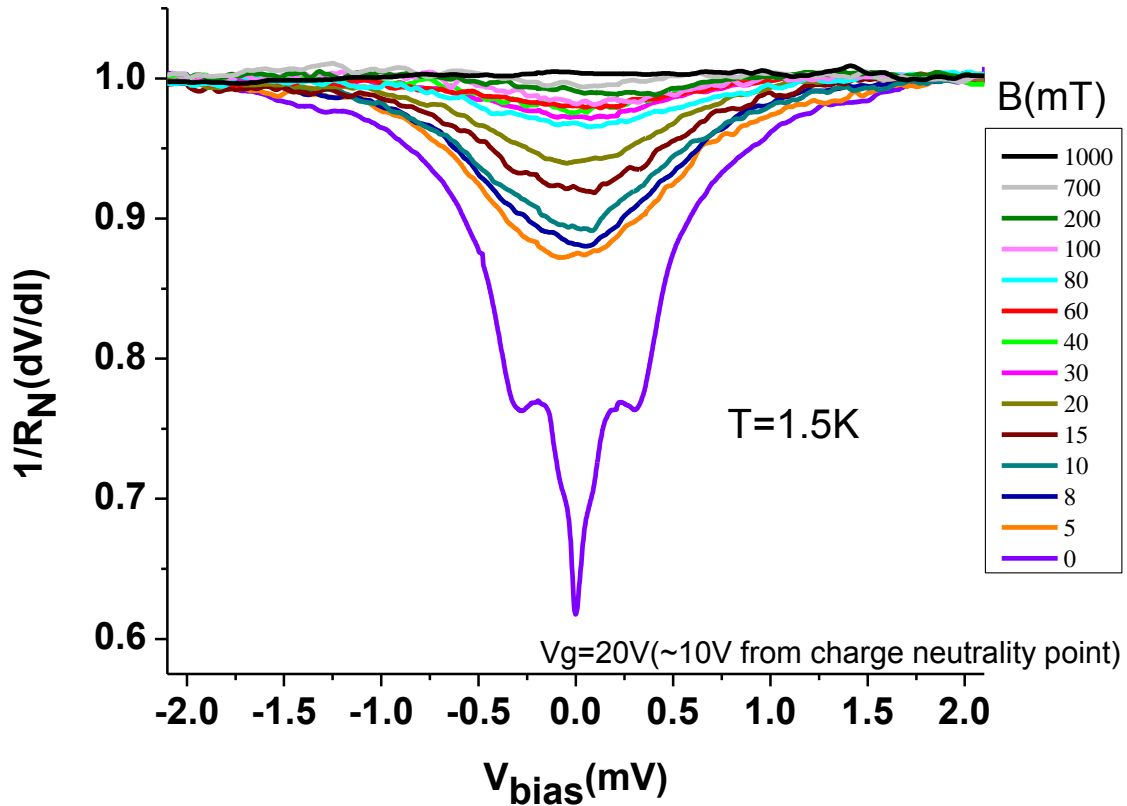
Figure 4.4: Zero field cool differential resistance measurements. Measurements are taken by monotonically increasing field from 0 to 1T at T=1.5K. V_g=20V, 10V from the charge neutrality point.

The effect of B on single ARs at the S-G interface can be better evaluated by calculating the excess current I_{exc}. The normalized excess current ($I_{exc}R_N$) vs B is shown in figure 4.5(a) and it is clear that the excess current drops quickly and eventually reaches and remains zero above B= 200mT. A similar rapid suppression of the AR conductance enhancement at low magnetic fields is also seen in the Nb-graphene devices figure 4.5(b) at the same temperature and gate voltage except that the suppression is not complete and there remains a small non-zero excess current at

the higher end of the applied field range. The suppression, however, irrespective of the superconductor does not change with carrier density or with temperature below T_C. Also in the field range measured the NbN and Nb do not lose their superconductivity (verified to ~ 5T and Hc_2 of the Nb films ~ 3.5T). Only the proximity effect is suppressed.
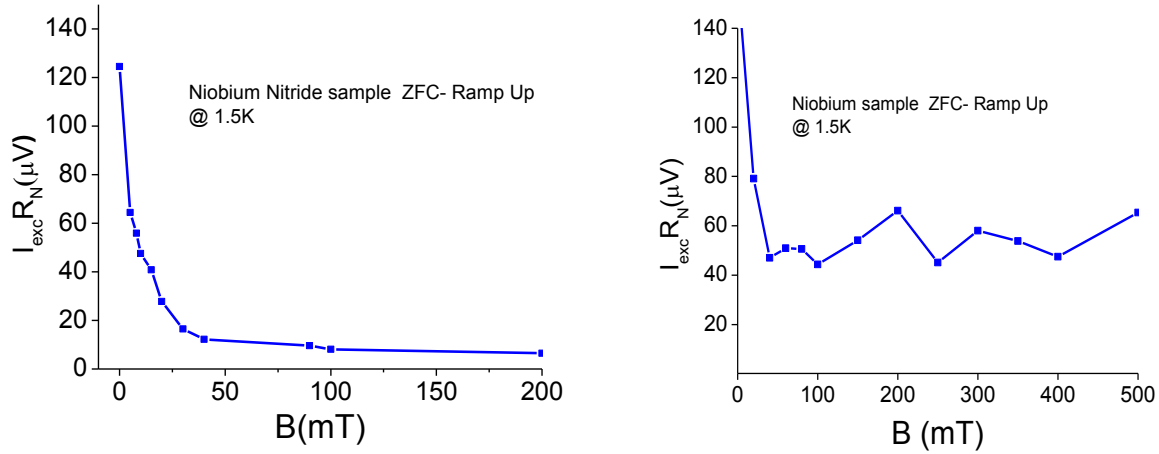
Figure 4.5: $I_{exc}R_N$ vs. applied magnetic field (B) for zero field cool- ramp up measurements: for (a) graphene - Nb (b) graphene-NbN junctions at 1.5K.

To explore the possible impact of magnetic flux (vortex) distribution on AR, the differential resistance measurements are taken under two other conditions. One is the field-cool (FC) process, where each time the magnetic field is applied above T_c and then device is cooled down to T=1.5K; while in the "zero field cool down-ramping" (ZFC ramp down) process, the magnetic field is ramped up from zero below Tc first to a high value (>1T) then decreased down to the desired values. The schematic of the three field ramp processes is shown in figure 4.6.
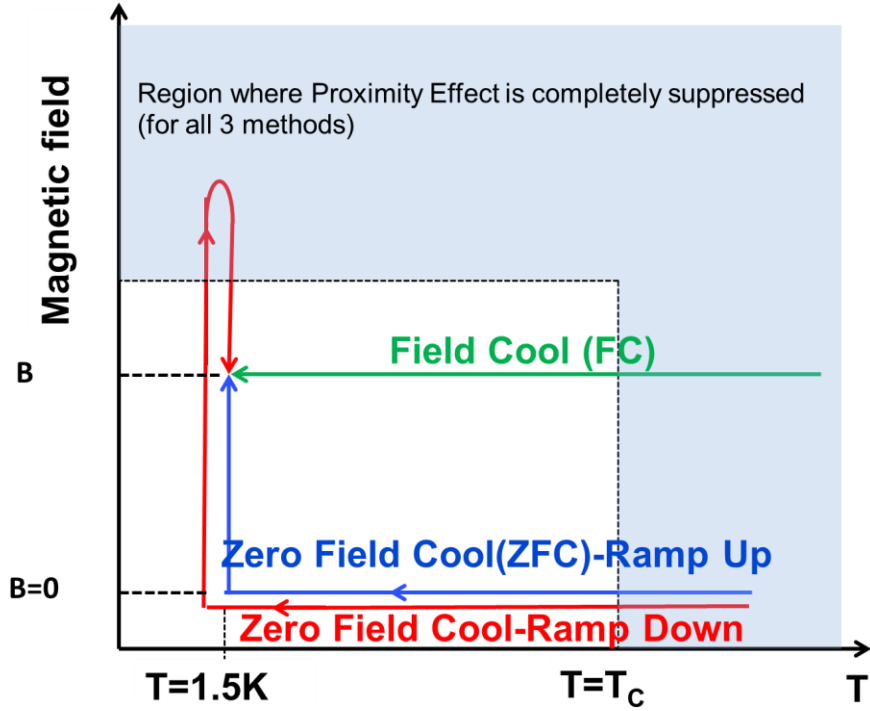
Figure 4.6: Schematics of the three magnetic field ramping procedures - 1. Zero Field Cool (ZFC) ramp up 2. ZFC- ramp Down 3. Field Cool (FC).

The $1/R_N$ (*dV/dI)* vs V_{bias} at 200 mT for all three methods is shown in figure 4.7. The conductance enhancement is retrieved when using the FC method whereas an even larger enhancement is observed by the ZFC ramp-down method. The differential resistance is also measured for various other values of B, in the range 0 to 1T. $I_{exc}R_N$ is a good estimate of the strength of the single AR probability. Therefore the $I_{exc}R_N$ values is obtained from the differential resistance curves and is shown as a function of the applied field B in figure 4.8. It is now clear that, in general, the excess current is higher for the FC technique compared to the ZFC ramp up technique. For the ZFC-ramp down technique the excess current is the highest compared to the other two methods for fields above ~40mT. However, below 40 mT, the excess current dips slightly. This means that while the S-G interface is below T_c, cycling the field through it from zero to 1T and then back to zero does not retrieve the supercurrent. It is also important to note that the excess current obtained by the field cool technique overlaps with the ZFC ramp up data in the low field range (0-10 mT).
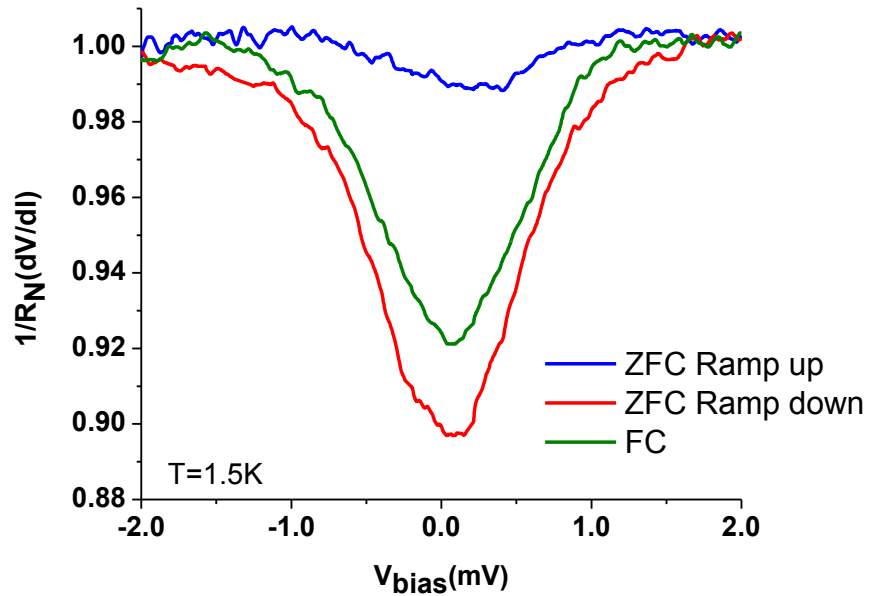
Figure 4.7: Comparison of the differential resistance curves at B=200mT for the three magnetic field ramping procedures. ZFC (blue), ZFC-Ramp down (red) and FC (green) and T=1.5K.
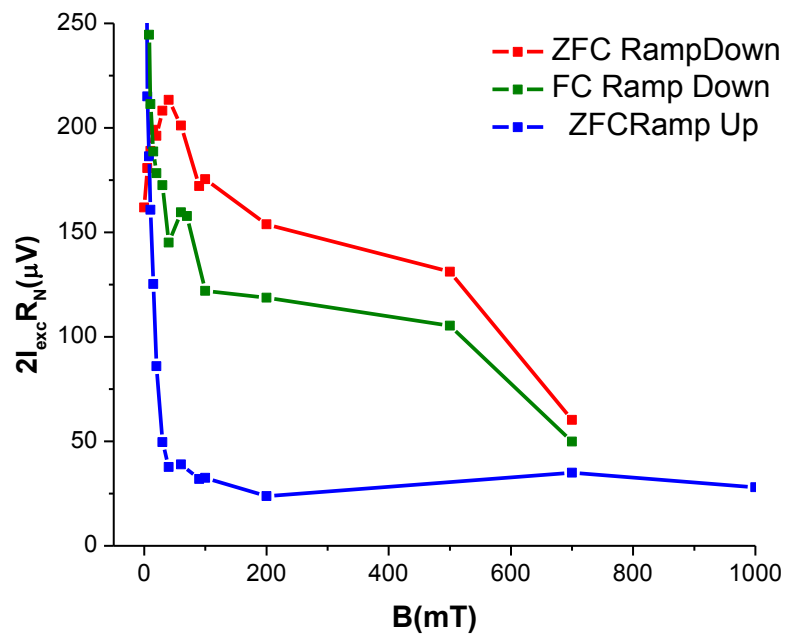
Figure 4.8: Comparison of excess current vs applied field B for the three field ramp procedures. ZFC (blue), ZFC-Ramp down (red) and FC (green) at T=1.5K.

4.4. Discussion and future work

The ZFC measurement on the suppression of AR probability in presence of a small magnetic field in our devices is qualitatively consistent with the previous theoretical and experimental works on superconductor/2DEG systems [83]. In these devices the "Doppler" shift of the quasiparticle spectrum was explained considering the Meissner current. At the SN interface on the S side, the Meissner current can be considered as a moving Cooper pair condensate with a momentum $(2p_s)$. Here $\vec{p}_s = e\vec{A}$ where $\vec{A}$ is the vector potential. The presence of this current shifts the momentum of the incoming and reflected Andreev electron (p) and hole ($-p$) on the N-side to $p+p_s$ and $-p+p_s$ respectively (in the direction of the current). If the resulting energy shift $\tilde{\varepsilon} = p_s v_F$ in the quasiparticle excitation spectrum is greater than the reduced gap (Δ)[8] the Fermi energy of the quasiparticles shifts outside the proximity reduced gap. This suppresses the AR probability [81, 82].

In type II superconductors vortices enter the superconductor above the lower critical field (H_{c1}) $\ll$ upper critical field (H_{c2}). In narrow superconducting strips the H_{c1} is further reduced. The vortices form once the magnetic field is above $B_m \sim \dfrac{\Phi_0}{L_c^2}$, where $\Phi_0 = h/2e$ is the superconducting flux quantum and L_c is the width of the superconducting thin film[84]. For the dimensions of our devices, this gives $B_m \sim 0.5mT$ which is at the low end of the magnetic field applied in our experiments. So the effect of vortices should be considered in explaining the observations. Vortices nucleate at the surface of the superconductor and penetrate into the interior of the thin film. Each vortex carries a flux quantum Φ_0 in its core of size ξ -the superconducting coherence length. Inside the core, the superconducting electron density vanishes. The field is maximum at the core and decays over a certain length scale[9] determined by the penetration depth λ. Screening currents encircle the core in the region where the field decays. In strong pinning superconductors when a magnetic field is applied, the motion and distribution of vortices on the superconductor is

---

[8] Note that Δ is smaller than the bulk superconducting gap of NbN, which, from the T_c should be around 1.8meV. So the Doppler shift mechanism is observable in SN interfaces where the gap is reduced at the SN interface.

[9] Length scale over which the field decays differs based on the vortex type. Pearl vortices that form in thin films decay as 1/r within the Pearl length (=2λ²/d, where d- thickness of the film) and 1/r² outside Pearl length. The scale of Abrikosov vortices that form in bulk films is log (λ/r).

determined by how the field is applied and hence is different for ZFC vs. FC. It also depends on ZFC ramp directions performed below T_c. The hysteric-like behavior of the excess current with ZFC - ramp up and down procedures and the inability to completely retrieve the supercurrent through the device after a complete ZFC cycle all indicate that the distribution of vortices has a direct impact on the proximity effect. The resultant vortex screening current emerging from the distribution should correlate to the observations of the suppression of the proximity effect in the same manner as the Doppler shift mechanism with Meissner current.

Based on results from magneto-optic imaging of vortices reported in work [86, 87], the following explanation for the observations is proposed. For the ZFC, above $B_m = 0.5mT$, the vortices penetrate the NbN superconductor from the edges (boundaries). Due to vortex pinning, edge defects and vortex-vortex interaction, they pile more on the edges. As the field is increased more vortices enter from the edge and slowly nudge the other vortices to the center of the superconductor. Eventually, above a certain field a non-uniform distribution of vortices builds up in the entire leads. This completely suppresses the proximity effect. On the other hand in the case of FC, above T_C, the magnetic field penetrates through the superconductor uniformly and when cooled below T_C the vortices are "frozen" (pinned) in place and the distribution remains uniform. In the case of ZFC-down ramp, while ramping down, flux free regions can form due to penetration of anti-vortices (vortices of opposite polarity) that annihilate the vortices. These flux free regions can explain the increase in excess current. But the annihilation is not complete due to strong pinning and non-uniform vortex density. So when the field is ramped back to zero, some vortices remain trapped and the proximity enhanced conductance is not fully recovered. This can explain the dip in the excess current below ~40mT for ZFC ramp down in figure 4.8.

The actual distribution of vortices (or the associated screening current distribution) is difficult to calculate as it depends on the pinning properties, grain boundaries, defects, film roughness and the geometry of the leads. But the observations follow the general predictions of the Bean's critical state model[88] ,which explains the distribution of Abrikosov vortices in bulk type - II superconductors with width $\gg \lambda$. Theoretical calculations are required to see how the

model exactly applies for the arrangement of Pearl vortices in thin films of width~ λ [10] (The superconducting leads on the sample are of width ~2μm and a rough estimate of λ for NbN~0.5μm).

The Oxford superconducting magnet also uses the type II superconductor – Nb_3Sn and it can have trapped flux when a current is ramped back and forth through it. So it is important to know whether any hysteresis from ramping the magnet back and forth affects the measurements. But from tests performed using FC measurements of differential resistance, the $I_{exc}R_N$ vs B curves for ramp up and ramp down (figure 4.6) overlap. This eliminates the role of the magnet[11] and confirms that it is indeed the vortices in the NbN contacts that are responsible for the observed suppression of the proximity effect. Typically trapped flux in magnet systems after a complete ramp cycle, if present, is found to be low, with a shift in the field around 20-50 gauss.
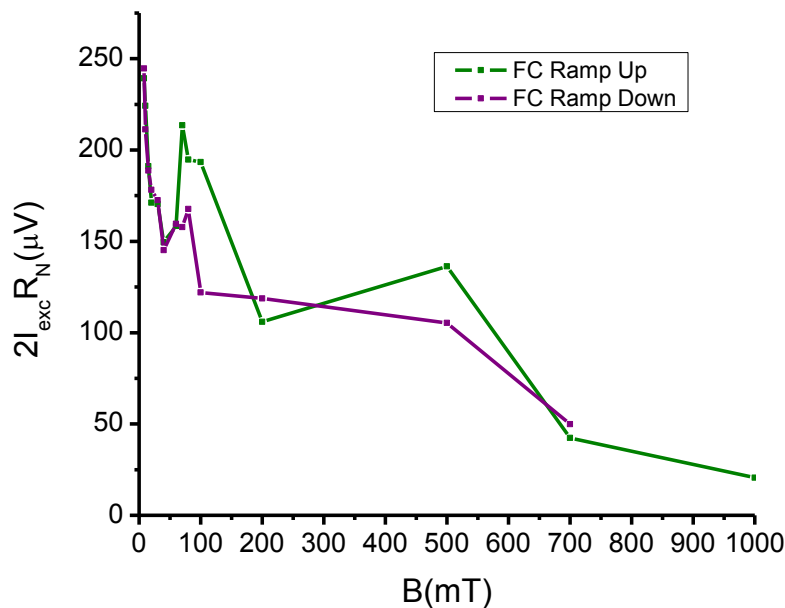
Figure 4.9: $I_{exc}R_N$ vs B - for FC ramp up and down to test any impact from trapped flux in the superconducting magnet system.

[10] A possible way to study the effect of vortices and test it directly with the Bean's critical model is to make wider, thicker leads. But the technical challenge is the total stress of the wide film on the graphene will be larger and therefore can affect the interface properties.

[11] The reason for the spike around 65mT, which is seen in all curves, is unknown. But generally the excess current for FC Ramp up and down overlap especially for the field range 0-60mT, unlike the ZFC Ramp-down curve.

In addition to vortices as the source of the supercurrent, the impact of the current's spatial distribution for the overlap-type SN junctions should be considered. The presence of a distributed contact resistance and graphene's sheet resistance can result in non-uniform current distribution across the SN junction. Such non-uniform current will inevitably couple to the distribution of supercurrent in determining the total conductance of each SN junction.

Another important question that has to be answered is how the suppression of proximity effect varies when using other type II superconductors. Preliminary results show that the suppression indeed takes place in Nb based devices as shown in figure 4.5 (b). But a small finite excess current remains even at fields ~1T. This indicates that the properties of the superconductor − pinning forces, penetration depth and the coherent length influence the arrangement of the vortices and hence its effect on the proximity effect.

Due to the suppression of proximity effect, evidence for Andreev edge states in the QH regime is also suppressed. This can be seen in figure 3.2 (c) where at 200mT and 300mT, even though the leads are superconducting, the QH plateaus are no different from a normal graphene device without proximity effect. Figure 4.10 illustrates this point further. The data is for suspended graphene-Nb superconducting junction. The differential resistance measured at $v=2$ (the valley or compressible state between $v=2$ and $v=6$ plateaus) and $v=6$ plateau corresponding to incompressible state almost overlap for T=1.5K and T=5.8K (~ T_c of Nb at 0.75T). There is only a small increase in the resistance within 2Δ in both cases which is different from the theoretical expectations. Even though our Nb- graphene retain some proximity effect in high fields (see figure 4.5 (c)), the absence of Andreev edge states is no different from the observations of many other experiments reported recently [23, 24]. At this stage the reasons for this is not clear. But it is likely that a very strong proximity effect is required to generate an Andreev edge state. In the QH incompressible regime, the bulk is insulating and only edge states exist. The electrons/holes in these edge states undergo AR on the S-G interface and the reflected charge carriers are bound to the edge. So they have chance to undergo AR again and again. The interference of these AR processes determines the effective current that runs parallel to the S-G interface. In a perfect interface, the presence of AR bound edge current is expected to enhance the QH conductance by a factor of two[22]. But if the interface is not completely transparent (low AR probability), multiple

entry into the SN interface can create normally reflected particles along with AR particles. The normally reflected particles are still confined to the skipping orbit or edge states. So these normally reflected electrons/holes can undergo AR reflection, but now with a compounded probability which is even lower. This will greatly reduce the electron-hole composition of the AR bound pairs along the S-G interface leading to a suppressed or nullified effect. Other than improving the transparency and the gap, whether modifying the sample geometry can mitigate this suppression (superconductor point contacts with van der Pauw method measurements) is an open question.

Understanding the suppression of Andreev reflection and the role of vortices is an important step towards studying or using proximity related phenomena in magnetic fields especially when the superconducting gap at the interface is reduced. If the effect of vortices has to be minimized, interface engineering using appropriate buffer layers to maintain the bulk superconducting gap at the S-N (or S-G) interface is required. Some recent work have shown some progress in this aspect [24, 89].
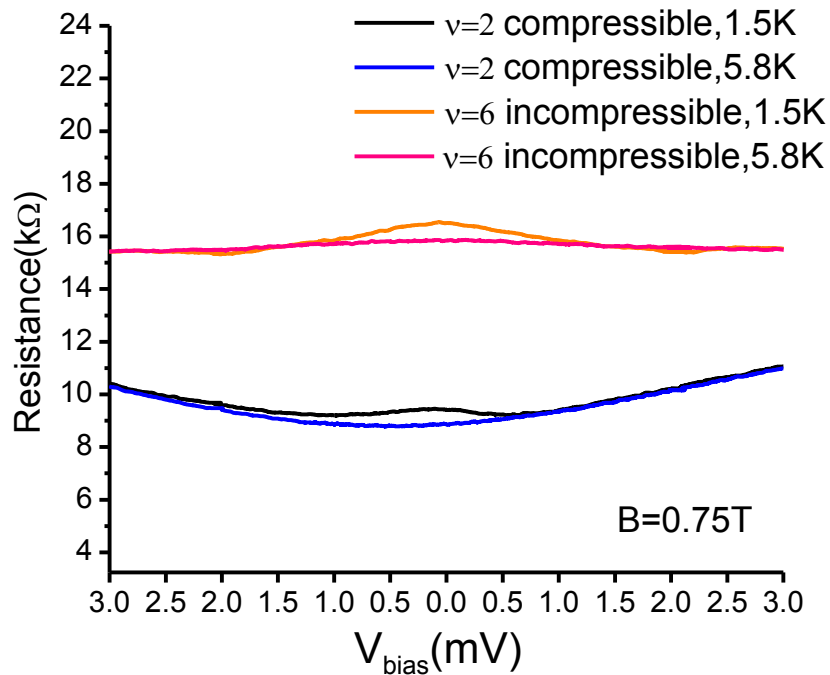
Figure 4. 10: Differential resistance in the quantum hall regime of the suspended graphene Nb superconducting junction.

Chapter 5

Fabrication of graphene heterostructures for Klein tunneling experiments

5.1. Klein tunneling of relativistic particles

Scattering and tunneling of Schrodinger particles on a potential barrier is one of the popular concepts in the early days of quantum mechanics. So within a year after Paul Dirac worked out the equations for relativistic particles, the scattering problem was worked out for relativistic fermions by Oskar Klein[26]. The result was surprising and considered paradoxical. The 'Klein' paradox (as it was known) is as follows. For a 1-D step potential given by

$$V(x) = \begin{cases} 0 & x < 0 \\ V & x \geq 0 \end{cases} \tag{5.1}$$

the transmission across the barrier for the non-relativistic case when particles of energy E <V in the x direction is T~ exp (-αx) for α>0. Here α is the kinematic factor and is a function of barrier height and energy of the incident particle. But for the relativistic case, the transmission is

$T \sim \left(\dfrac{4\kappa}{(1+\kappa)^2} \right)$ for V>>E, where κ >1. Here κ is similar to α but calculated for the Dirac equation.

The paradox is that the transmission does not decay but propagates through the barrier and is finite even for an infinitely tall and wide repulsive potential!
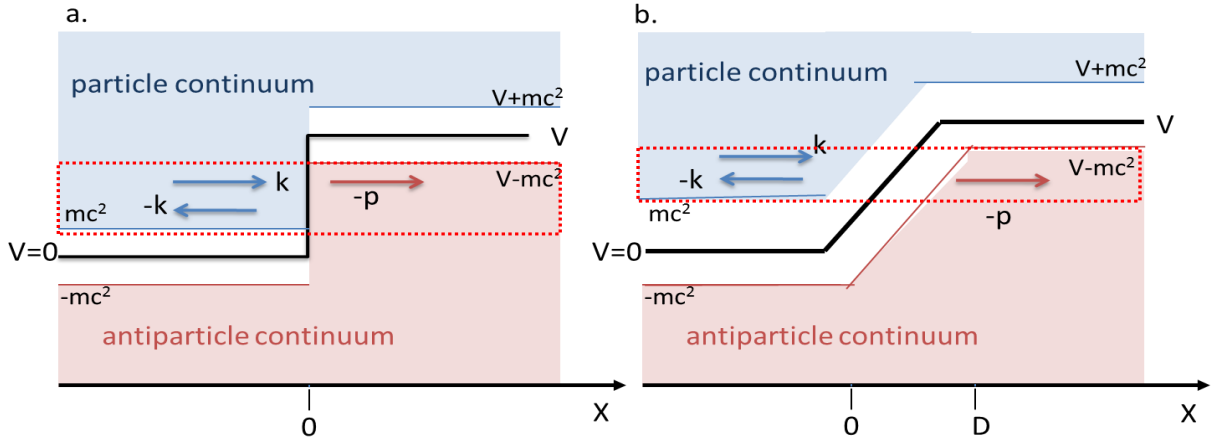
Figure 5.1: Tunneling of Dirac particles of mass m across a. Klein (sharp) b. Sauter (smooth) potential step. The red dotted show the overlap region of the particle and antiparticle continuum, when $mc^2 < E < V - mc^2$.

This paradox, however, was later understood as due to spontaneous formation of particle antiparticle pair from the vacuum at the barrier [90, 91]. As long as the barrier height $V \sim mc^2$ or higher, the particle effectively propagates as an antiparticle inside the barrier as depicted in figure 5.1 (a). In condensed matter physics this is simply understood as electrons propagating into the inverted hole energy states within the barrier (inter-band propagation). It was also conjectured by Bohr that the Klein result is only valid when the potential is sharp on the scale of the Compton wavelength $\lambda_C = \dfrac{\hbar}{mc}$. Sauter later confirmed this by solving the same problem for a smooth potential step (Figure 5.1 (b)) and obtained the anticipated exponential decay for transmission[92]. So for a potential

$$V(x) = \begin{cases} 0 & x < 0 \\ Sx & 0 \le x \le D \\ V & x > D \end{cases} \qquad (5.2)$$

the transmission $T \sim e^{-2\pi^2 \frac{hc}{S\lambda_C^2}}$. The decaying transmission ensues since the fermions have to traverse the classically forbidden evanescent regime i.e., when the momentum $p(x) = \sqrt{(V(x) - E)^2 - m^2}$ is imaginary.

71

Klein tunneling of relativistic particles across sharp barrier are expected to be observed near the event horizon in black holes as Hawking radiation[93] and positron generation from a super critical nucleus and [94]. These extreme physical conditions are required since the barrier should be at least equal to mc^2 within a scale of the Compton wavelength of an electron which is $\sim 10^{-12}$ m. Graphene, however, with its Dirac-like spectrum and m=0 provides an ideal system for a table top demonstration for Klein tunneling.

5.2. Klein tunneling in graphene

As seen in chapter 1 the charge particles in graphene are chiral. If there are no mechanisms that flip the pseudospin (i.e., no scattering processes that couple the two sub lattices) then the particles cannot backscatter as chirality is conserved. Therefore in a bipolar junctions (*pn* or *np*) the charge particles cross the junction by preserving the pseudospin direction and by a conversion of electrons to holes (figure 5.2(a)). This results in perfect transmission at normal incidence. Being massless there is also no minimal value for the potential as in the case of relativistic particles with finite rest mass in QED.

For a *pn* junction which is sharp on the Fermi length scale ($k_F D <1$) but smooth on the lattice scale (*a~2.46A*) there is no inter-valley scattering and the value of transmission can be reduced to a simple form by considering the overlap probability of the electron wave function $\Psi_K^+(\theta)$ outside the barrier and hole wave function $\Psi_K^-(\pi-\theta)$ propagating inside the barrier (see equation 1.8):

$$T = \left\langle \Psi_K^+(\theta) \middle| \Psi_K^-(\pi-\theta) \right\rangle = \cos^2 \theta \tag{5.3}$$

Here $\theta = arctan\ (k_y/k_x)$ and *x* is the direction perpendicular to the barrier and *y* - parallel to the barrier. So for a range of values of θ, the transmission is finite irrespective of the barrier height and complies as expected with the Klein calculation. For normal incidence there is perfect transmission. The transmission for sharp barriers was also calculated for bipolar heterostructures(*npn, pnp*) by Katsnelson *et al* [25]. The transmission for a rectangular barrier of height V between $0<x<w$ that extends infinitely along the y axis is shown in figure 5.3(a). Here

perfect transmission is observed, not just for normal incidence, but also at larger angles. This is due to the resonances inside the barrier set by the condition: $q_x w = \pi N$ where $N=0, \pm 1, \pm 2$. Here q_x is the momentum in the x direction inside the barrier.
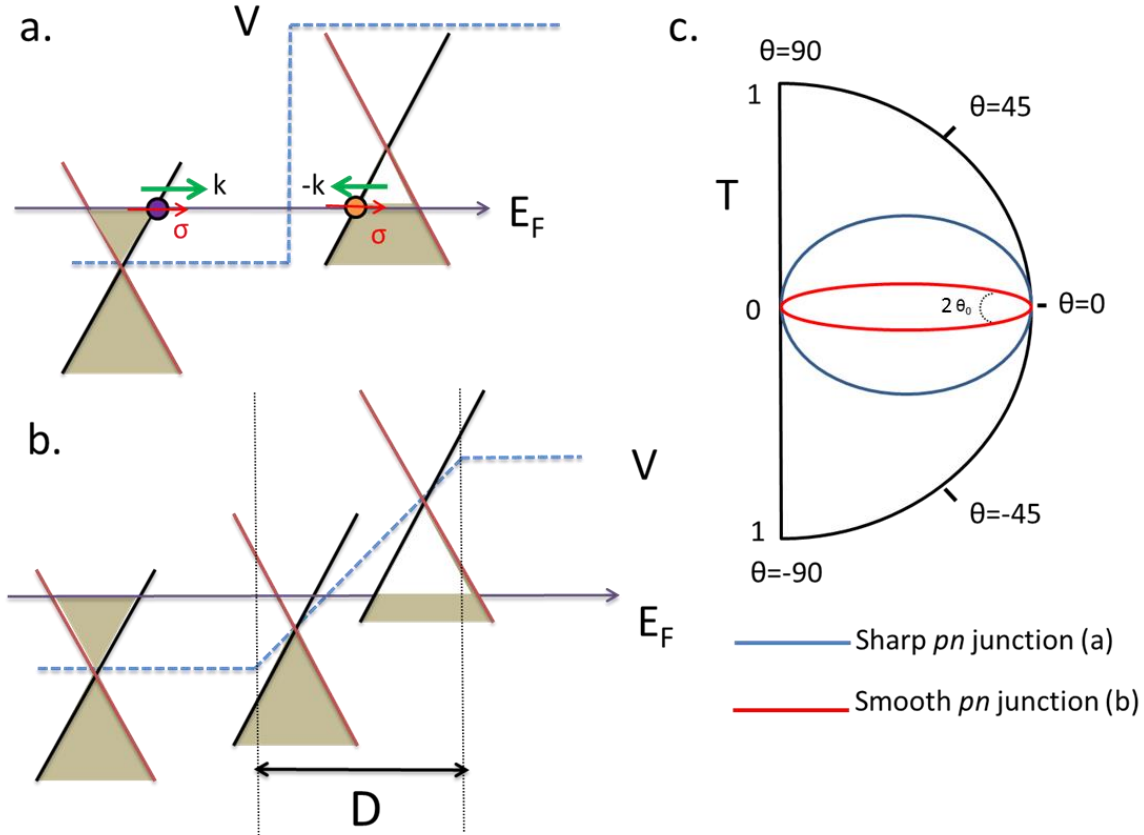
Figure 5.2: Klein tunneling in graphene across a pn junction for **a.** Sharp barrier **b.** Smooth barrier. The directions of pseudospin σ and momentum vector k are depicted inside and outside the barrier. **c.** Transmission (T) as a function of incident angle θ. $2\Theta_0$ is the angular range for propagating transmission smooth barrier. See main text for details.

To observe Klein tunneling, it is necessary to have sharp *pn* junctions such that $k_F D < 1$. In experiments potential barriers local gates are used to create a local electric field profile on the graphene strip. Based on the best case for the minimum carrier density~ 10^9 cm^{-2}, typically obtained with ballistic suspended graphene, D~$1/k_F = 150$ nm. This is practically challenging when including the extent of the stray fields. Therefore the more realistic *pn* junctions in

experiments is the smooth Sauter-like potential shown in figure 5.2 (b). Cheianov and Falko in [95] worked out the transmission for a smooth potential, similar to the one in equation 5.2 but in 2D with $k_F D>1$, The electrons in graphene that are incident at the center of the barrier with $E = \hbar v_F \sqrt{p_x^2 + p_y^2}$,will have a momentum $p_x(x) = \sqrt{V^2(x)/v_F^2 - p_y^2}$ that becomes imaginary when $|V| < p_y v_F$. So within a distance $p_y v_F / S$ from the junction the transmission is via evanescent modes. Only close to normal incidence, $p_y=0$, the transport is propagating. The transmission turns out to be,

$$T \sim e^{-\pi(k_F D)\sin^2\theta} \tag{5.4}$$

which is similar to the form Sauter obtained. Figure 5.2 (c) illustrates the transmission as a function of incident angle for a sharp and a smooth barrier. The sharp barrier has higher transmission for a wider spread of incident angles around zero (see equation 5.3), but for the smooth potential the spread is reduced by D and k_F. The bipolar heterojunction for the smooth potential, shown in figure 5.3 (b), is just an extension of the result for the smooth step potential. The problem can be considered as two *pn* junctions in series (since *pn* junctions in graphene are not rectifiers like semiconductor diodes). Note that the perfect transmissions at high angle resonances seen in sharp bipolar heterostructures in the barrier are no longer present in heterostructures with smooth junctions.

So far the discussion was based on coherent charge carriers with well-defined incident angles. But in real devices the incoherent nature of the charge carriers due to the diffusive doping near the contact leads[96], a single angle of incidence cannot be considered. The incident electrons have a random distribution of angles and hence the effective transmission is the sum of all contributions. But from equation (5.4) the *pn* junction filters out only electrons at angles $|\theta_0| = 1/(\pi k_F D)^{1/2}$ about the normal. For a *pnp (npn)* junction electrons incident at $|\theta_0| \sim 1/(2\pi k_F D)^{1/2}$ or lower are collimated through. The smoother the junction more the collimation. The relation between the transmission through a *pn* junction and its conductance follows from the Landauer formula:

$$G \sim \frac{4e^2W}{h} \int_{-\pi/2}^{\pi/2} \frac{k_F d\theta}{2\pi} T(\theta) \sim \frac{2e^2W}{h} \sqrt{\frac{k_F}{D}} \qquad (5.5)$$

Here W- width of the sample. Due to the collimated transmission the resistance of a *pn* junction (R_{pn}) is higher than a unipolar junction (R_{pp} *or* R_{nn}).
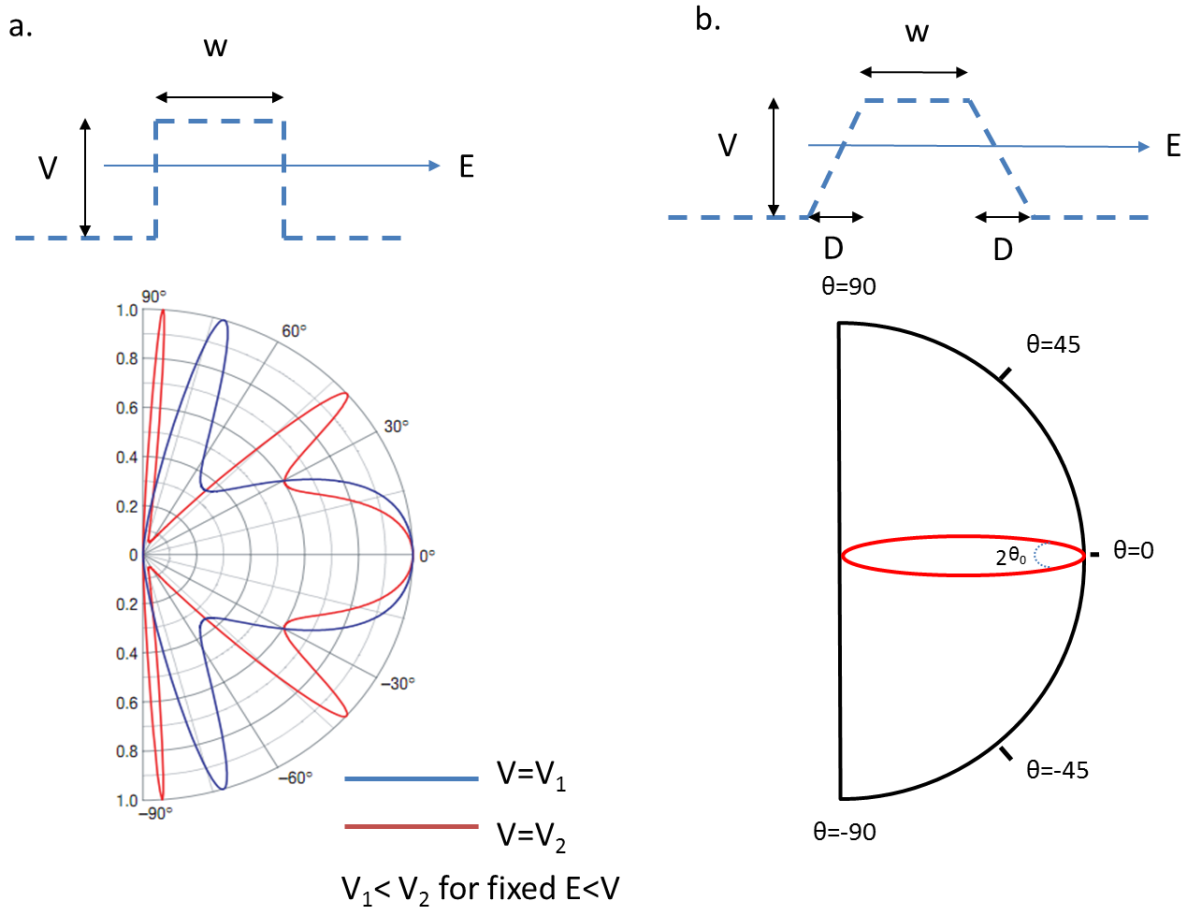

Figure 5.3: **Transmission as a function of incident angle θ for a bipolar graphene heterojunction a. Sharp rectangular barrier b. Smooth rectangular barrier.** Figure for (a) was adapted from [25].

5.3. Experimental Studies of Klein tunneling in graphene heterostructures – a short overview of previous work

To study Klein tunneling, previous work have focused on fabricating graphene heterostructures with ballistic *pn* junctions i.e., mean free path $l_m > D$. The heterostructures were created by using local gate across a graphene device separated by a high dielectric medium. The part of the graphene underneath the gate can be tuned to a different carrier density (*p'* or *n'*) with respect to the carrier density of the regions on either side of the gate (*n* or *p* respectively) creating the required bipolar heterostructures- *pn'p or np'n*. In-order to meet the ballistic requirement, thin layers with high dielectric constants (to reduce D) and/or dielectric materials that do not affect the quality of the graphene (for longer l_m) were chosen. The common dielectrics used were PMMA, atomic layer deposited Al_2O_3, HSQ, HfO_2 and thermal evaporated SiO_2 [97-101]. Contactless (air) top gates were also used to prevent graphene from any contamination or damage from the dielectric [102, 103]. But although in most of these devices the *pn* junctions were ballistic, the graphene channels were not, as they were fabricated on SiO_2 substrates. Even within the barrier the transport was not phase coherent ($l_m < w$). So a comparison of resistance of the unipolar ($R_{pp'p}$) and bipolar ($R_{pn'p}$) cannot provide sufficient evidence for Klein tunneling. Hence evidence for Klein tunneling required extracting the resistance of the *pn* junctions from the resistance of the entire device. This was done by estimating $R_{pp'p}$ - $R_{pn'p}$ with $\left|p'\right| = \left|n'\right|$ along with the fact of electron hole symmetric resistance in graphene, $R(\left|p'\right|) = R(\left|n'\right|)$ (see [98] for details). Other evidence using diffusive junctions were also indirect and required position dependent resistance modeling to extract resistances of a unipolar and bipolar junction[97].

A more direct evidence for Klein tunneling was provided by Young et al., in [104]. They achieved this by fabrication of heterostructures with narrow local gate and thin and high gate dielectric ($\epsilon \sim 12$) and demonstrated phase coherent electrons within the barrier. The transmission /reflection is exponentially suppressed at oblique angles due to the smooth potential created by the local gate. But within the barrier electrons at oblique incidence are reflected back and forth on the walls of the barrier. This creates Fabry Perot like interferences and results in oscillations in the

conductance of the junction. Theoretically, Shytov *et al.* [105] showed that, applying small magnetic fields, the angle of incidence can be bent to facilitate normal reflection-less Klein tunneling through the barrier. This will be witnessed as a shift in the phase of the interference pattern within the barrier. Following this idea and carefully analyzing the corresponding shifts of the conductance oscillations in weak fields, Young *et al*., provided a direct evidence for Klein tunneling. It is important to note that this method only required the charge carriers within the barrier to be coherent.

But a more robust evidence for Klein tunneling and other phase coherent phenomena in graphene heterostructures require entirely ballistic channels. In such ballistic structures a comparison of the conductance of the device in the unipolar and bipolar regime can provide a straightforward evidence for Klein tunneling. Moreover in these devices, graphene within the barrier as well as the graphene channels between the contacts and local gate will serve as cavities for Fabry Perot oscillations. This can provide more possibilities to test the Klein and Sauter effect. Extending previous work[99] to explore (fractional) QH physics especially near the CNP in combination with the *pn* junction will also require entirely ballistic heterostructures. And eventually for applications retaining quantum coherence phenomena at high temperatures, high mobility long mean free path devices will be important. Suspending graphene is a good means to achieve low carrier densities. But a local gate on suspended graphene will have to be either contactless - over the graphene or substrate supported and defined underneath graphene. In the coming sections, I will discuss the work on the fabrication of contactless local gated suspended graphene devices. Graphene on hexagonal boron nitride (h-BN) devices provide an alternative to suspended graphene heterostructures and they are indeed much more stable and are not limited by size. In section 5.4.2 I will describe the fabrication of graphene/h-BN devices that use local gated architectures to spatially manipulate electrons using the Klein collimation effect.

5.4. Fabrication of ballistic graphene heterostructures

5.4.1. Fabrication of suspended graphene bipolar junctions with contactless gates

In chapter 2 the process for making ballistic samples by suspending graphene was discussed. For that purpose a two resist method was used since the superconductor materials were reactive buffered HF and KOH - commonly used etchants for removing SiO_2 to suspend graphene. Here a combination of the two methods is used – the two resist method for creating the contactless air top gate and the wet etching using buffered HF acid to suspend graphene. The procedure is as follows:

A. The sample design and EBL

HOPG graphene is deposited by the dry nitrogen blow press method on clean commercial Si wafer with a 285 nm thick SiO_2 coating. Then the substrate is spin coated with PMMA A3 at 4000 rpm (120 nm). After that ~ 2-3nm of SiO_2 is e-beam deposited and then the MMA EL 11 at 4000 rpm (500nm). Baking temperatures and times are the same as explained Chapter 2. For EBL the design used is shown in figure 5.4 (a). For defining the four terminal contacts (two for current: I+, I- and two for voltage: V+ and V-), the e-beam dose is chosen so that it exposes both resists. To fabricate the bridge like contactless local gate, the dose is carefully selected so that only the MMA layer is exposed on the 100-150 nm narrow region over graphene. Then the dose is gradually increased on either side of graphene, within a distance of 70 nm, till the dose required to expose both the resists is reached. The SiO_2 layer is a sacrificial layer and is used to prevent any over-developing of the PMMA resist. In chapter 2, for the suspended SGS junctions, the graphene is sandwiched between the two resists. Therefore the SiO_2 layer is not required as graphene screens any overexposure by the electron beam. But when using just the two resists, EBL writing of fine features such as the local gate is difficult and a slight overdose or overdeveloping can result in a rough and crooked gate structure as seen in Figure 5.4 (d). Having the SiO_2 layer provides a leeway in choosing the dose. Also, the dose for the contacts is reduced slightly from the value used for larger leads that extend away from the top gate, to minimize overdose due to dose-proximity effect.
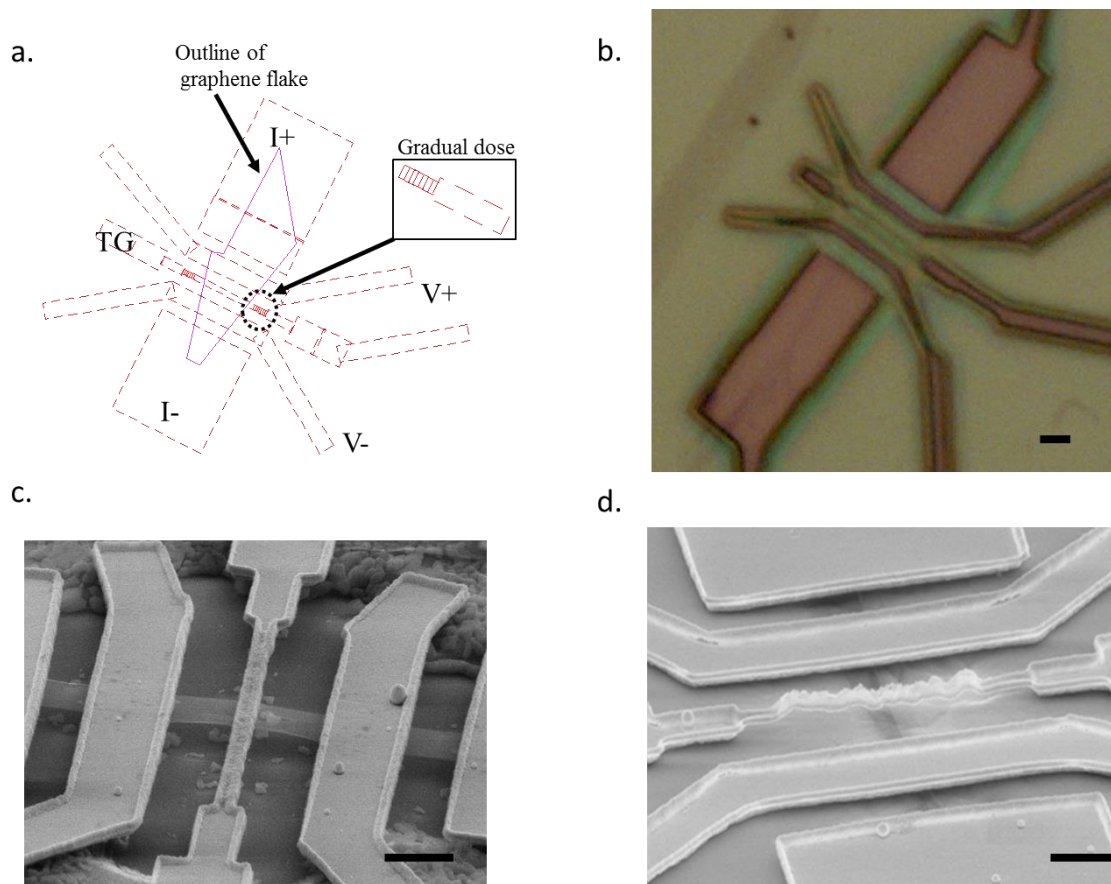
Figure 5.4: Fabrication of suspended graphene with contactless air top gate (TG). a. Design of the pseudo four terminal device **b.** Device after developing. The pink region reveals the SiO_2 /Si substrate. The thin line is in the center between the V+ and V- is MMA which will form the TG. **c.** SEM image of the device. Graphene channel is arched upwards due to electrostatic attraction. **d.** Under written TG, fabricated without using the sacrificial SiO_2 layer between PMMA and MMA. Scale bar is 1μm.

B. Developing procedure

The developing procedure starts with a 35 s rinse in MIBK: IPA (1:3) and then a brief 15s rinse in pure IPA to wash away the MIBK. At this stage only the MMA is developed and the SiO_2 protects the PMMA. Next to remove the SiO_2, the sample is dipped in 7:1 (NH_4OH: HF) buffered HF for 10s and then in deionized water to dilute away the HF. After this, to develop the exposed PMMA, the sample is introduced to a bath of cold deionized water: IPA (1:3) for 45-50s. These parameters are found to work for a top gate dose ~80μC/cm^2 and a maximum contact lead dose of ~230 μC/cm^2.The sample after developing is shown in figure 5.4 (b).

C. Metal contacts

Ti/Pd/Au metals are e-beam evaporated with thickness 1*nm*, 80 *nm* and 40 *nm* respectively to make the contacts. A thin layer ~ 1nm of Ti serves as the adhesive layer. The *1 nm* thin Ti is non-uniform, allowing the next metal on top – Pd to come in contact with graphene in patches and palladium is known to make good contact with graphene at low temperatures[106]. Palladium cannot be used directly as it does not stick to SiO_2.

D. Lift off and procedure for suspending graphene

The lifted off is carried out in warm acetone and then finally the sample is rinsed in IPA. For reducing the risk of collapse of the suspended gate, the same precautions as mentioned in chapter 2 are followed and the sample is taken out to air from warm IPA. To suspend graphene, the substrate needs to be coated with resist again. The resist is patterned with an etch window so that SiO_2 underneath graphene will be etched away. Again, to avoid the collapse of the suspended gate, anisole diluted PMMA (PMMA A 0.5), which is a less viscous resist, is used. A drop of the resist is applied on the substrate without spinning and is baked at 180^0C. Then a window is defined by EBL just on the region of the graphene strip at a dose 700 $\mu C/cm^2$. The sample is then developed in MIBK/IPA and rinsed with IPA. Next the sample is immersed in buffered HF (7:1) for 300 s and then moved into acetone and IPA baths to remove the PMMA mask. As usual, suspended samples are never taken out of the solvents. So finally, the sample is taken out by using a critical point dryer (Tousimis Samdri-795). The warm IPA method is avoided as the graphene channels used are longer 1.5-2µm and the distance from the substrate to the suspended channel is small ~ 100-120 nm, increasing the likelihood of collapse by surface tension.

Challenges

The fabrication scheme above helps to fabricate a sample with an air gate which is closest to suspended graphene (~ 120 nm, equal to the PMMA thickness). Also fabrication only requires a small number of steps. It does not require rotation or tilting of sample during metal deposition [102]. As demonstrated in chapter 3, the carrier density in suspended graphene can be as low as ~10^9 cm^{-2}. So the devices in principle provide a good means to test Klein tunneling with sharp barriers. But since the device comprises two suspended structures and current annealing is always

required to remove residues in graphene, the yield for samples that pass all the necessary requirements is low. Current annealing of single layer graphene is known to be more difficult than bilayer graphene. In some cases, since the top gate is very close, the graphene film gets attracted it by electrostatic attraction creating a top gate leakage (Figure 5.4. (c)). In 2010, Dean et al., demonstrated BN can be used as a substrate to achieve ballistic graphene devices[29]. So this work took a new direction – fabricating graphene/BN devices with air top gates.

5.4.2. Graphene/BN based heterostructures with triangular air top gates for Klein collimation

Suspended graphene, despite having a few advantages, is limited by its size and the small gate range for tuning the carrier density. For experiments in manipulating electrons on the large scale, like Klein collimation and Veselago lensing experiments[28], more complex device architectures and multi-level fabrication processes are required. These are not practical with suspended graphene. Another way to eliminate the charge trapping effects from the substrate is to find a replacement for SiO_2 substrate, one which is atomically flat with no dangling bonds. Hexagonal boron nitride (h-BN) is ideal for this purpose since the lattice structure is almost identical to graphene. The hexagonal lattice comprises of B and N Bernal stacked sub lattices and the lattice mismatch with that of graphene is only 1.7%. Moreover the strong in-plane bonds create a relatively inert substrate, free of charge traps.

Unlike SiO_2 substrates the growth of high quality large scale h-BN substrates has not been realized yet. The h-BN are grown as crystals[12] and they are thin flakes exfoliatable like graphene. Therefore the fabrication processes requires a 'transfer process' that brings in contact two separately exfoliated graphene and BN flakes. In this section I present the transfer process of graphene on BN. The technique also applies for the transfer of BN on graphene, a variety of other 2D material hetero-structures and for the bottom gated suspended graphene structures that is mentioned at the end of this chapter.

---

[12] The h-BN used in this work was grown by Taniguchi and Watanabe from Advanced Materials Laboratory, National Institute for Materials Science, 1-1 Namiki, Tsukuba, 305-0044, Japan.

Procedure for fabricating graphene –BN devices

In-order to create BN- graphene layered devices, in this thesis work, a dry transfer method was developed that was inspired and adapted from work in [107] and [108] . The underlying technique uses a transparent stack of materials with a polymer release layer as a substrate for exfoliated graphene flakes. The transparent polymer stack with the graphene is then micro-manipulated and aligned to a *target* BN piece sitting on a second substrate and made contact. Applying heat to the *target* substrate releases the polymer stack containing the source flakes onto the *target* flakes.

The setup that is used for transfer at the time of writing this thesis is shown in figure 5.7. Several other "transfer machines" were built and tested before this, but they later gave way for this particular setup due its efficiency. Some of the samples reported in this thesis have employed older machines which require slightly different fabrication procedures. But to make the discussion concise only the new method is presented. Except for the machine design, the polymer stack used and the transfer procedure, the central idea behind all the methods is the same.

A. Preparation of flakes and substrates

Here I will use the following terminology– 'TARGET' and 'SOURCE' substrate or flake. Target substrate/flake is the substrate to which the source flake is transferred to. The source substrate is transparent with a polymer layer that contains the *source* flake which is to be pressed onto the *target* flake. The *target* and *source* flakes can be any 2D material. In the work discussed below the flakes are BN and graphene.

TARGET substrate and flakes (SiO_2/Si + h-BN): The *target* substrate used in this work is SiO_2/Si. First it is treated in UV/Ozone for 10 minutes and baked on a hotplate at 400^0 C. Soon after this, freshly exfoliated flakes of h-BN are deposited on the substrate by using the silicone free 'blue tape' (Ultron Systems R 1007). Suitable thin flakes (20-30 nm) are first selected under the microscope. Differential image contrast is used to eliminate buckled steps, cracks and any visible defects and bubbles on the flake. Later an AFM image of the flake is used to map any fine cracks or small bubbles of height (1-15nm) and an area which is flat

with sub nanometer (200-500 pm) roughness is selected. An optical and AFM image (tapping mode) of a very flat piece of h-BN flake of thickness ~12 nm and roughness within 200 pm is shown in figure 5.5 (a) and (b). Once the necessary flake is identified the substrates are stored in vacuum and only taken out right before transfer. (Note: If a graphene/graphite is the source flake on which BN is transferred the same procedure is followed. But the blue tape deposition of large sized Natural graphite, *NGS Naturgraphit*, can produce loosely attached flakes on the substrate. This is not the case for small sized flakes obtained using HOPG. The loose flakes can be removed by sonicating the sample in an acetone bath and cleaning with IPA before performing the AFM measurements).

SOURCE substrate (polymer coated PDMS/Glass slide+ graphene): The *source* substrate is a transparent stack made of glass slide, Polydimethylsiloxane or *PDMS (Sylgard 184* base and elastomer)* and a Duck® HD Clear™ tape. It is prepared as follows.

A transparent glass slide is cleaned using acetone/IPA and in UV ozone. Hardened PDMS is prepared to a 1mm thickness with no air bubbles and is laid carefully on the center of the glass slide. The PDMS glass stack is cleaned again under UV/Ozone for 10 minutes. After this, the tape is carefully placed flat on top of the PDMS piece. Next, two layers of resist (MMA 8.5 EL 8.5) is spin coated to get a thickness of ~ 600nm. The coated resist is baked for 10 minutes at 120^0C. The *Duck®* tape is preferred over the Scotch tape since it has a lower melting temperature. But still, heating above 150^0 C can melt the tape. Since the MMA polymer does not stick well to the PDMS, the *Duck®* tape is used as the transparent buffer. The PDMS layer is a solid-gel and is flexible. So it conforms well to the target substrate during the transfer. All the components here are transparent and target flakes can be seen through this substrate during transfer (Figure 5.6(a)).
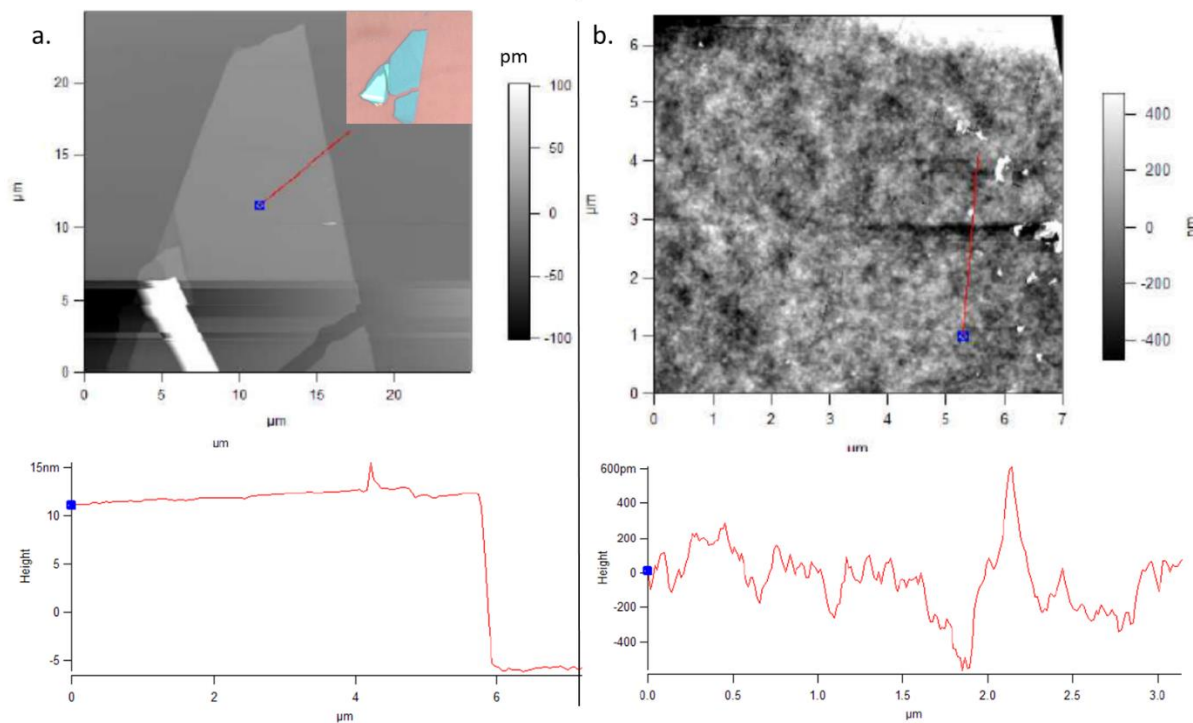
Figure 5.5: AFM image of BN flake on SiO₂ -Target substrate. Height retrace image and height vs distance along the red line starting from the blue dot. **a.** Flake thickness ~12nm (Inset) optical image of the flake. **b.** BN surface roughness on a zoomed in area of the flake.

Figure 5.6: Source substrate preparation. **a.** Glass slide with MMA/tape/PDMS **b.** Graphene on blue tape ready for deposition **c.** peeling off tape after tape is pressed on the MMA/tape/PDMS substrate.

Deposition of graphene on the MMA+PDMS stack can be done in two ways. One is to use the dry nitrogen cold press method discussed in Chapter 2. The other is to use the blue tape. The

tape method is essential for natural graphite as they are in the form of large crystals. The tape is therefore prepared by multiple fresh exfoliations of the graphite crystal on the same tape with no spacing and with minimal overlap between the peeled layers. Once prepared, the source tape will look shiny filled with thin continuous patches of graphite layers. Then a fresh piece of tape is pressed on top of it and slowly peeled to obtain a second copy of fresh cleaved flakes(figure 5.6 (b)). This is directly pressed onto the MMA/PDMS stack using a soft rubber tip with a small force for ~ 1 minute. Then, very slowly, the tape is peeled off (figure 5.6(c)). This is quite tricky and chances are that the MMA layer gets peeled off with the tape. Clean preparation of the PDMS stack, graphite tape and slow peeling is found to increase the chances of getting a large area graphene flake on the MMA layer.

B. The transfer setup

The transfer setup is shown in figure 5.7(a). It consists of a Carl Zeiss optical microscope and a micromanipulator stage underneath. The microscope stage is connected with a transparent plexi- glass of ~ 7mm. The plexi-glass is designed with clamps (figure 5.7(b)) that help to fix the glass slide *source* substrate supporting the transparent tape/PDMS stack. The plexi-glass stage is manipulated using the focus knobs (Z movement) and the X-Y stage knobs of the microscope. The XYZ- micromanipulator underneath the microscope is for the *target* substrate. This manipulator is attached with an aluminum block. The block is machined carefully so that the top surface is very flat. On top of the aluminum block a heater stage is installed (figure 5.7(c)). The heater stage contains a Tantalum metal foil carved with a meander design. It is spot welded with wires and connected to an external voltage power supply. The heater is thermally isolated from the micromanipulator by a glass piece and is securely enclosed using an aluminum frame and capped with a flat 3mm thick Aluminum piece (figure 5.7(d)). This serves as the stage for the target substrate. A thin sapphire film is also placed in the aluminum frame between the stage and the heater coil to enable good thermal contact. A hole of 1mm in diameter is machined on the target stage and a pathway is provided to a mechanical pump to create a suction necessary to fix the target substrate on the stage during the transfer. A calibrated thermocouple is fixed on the top of the stage to determine the temperature of the target substrate.
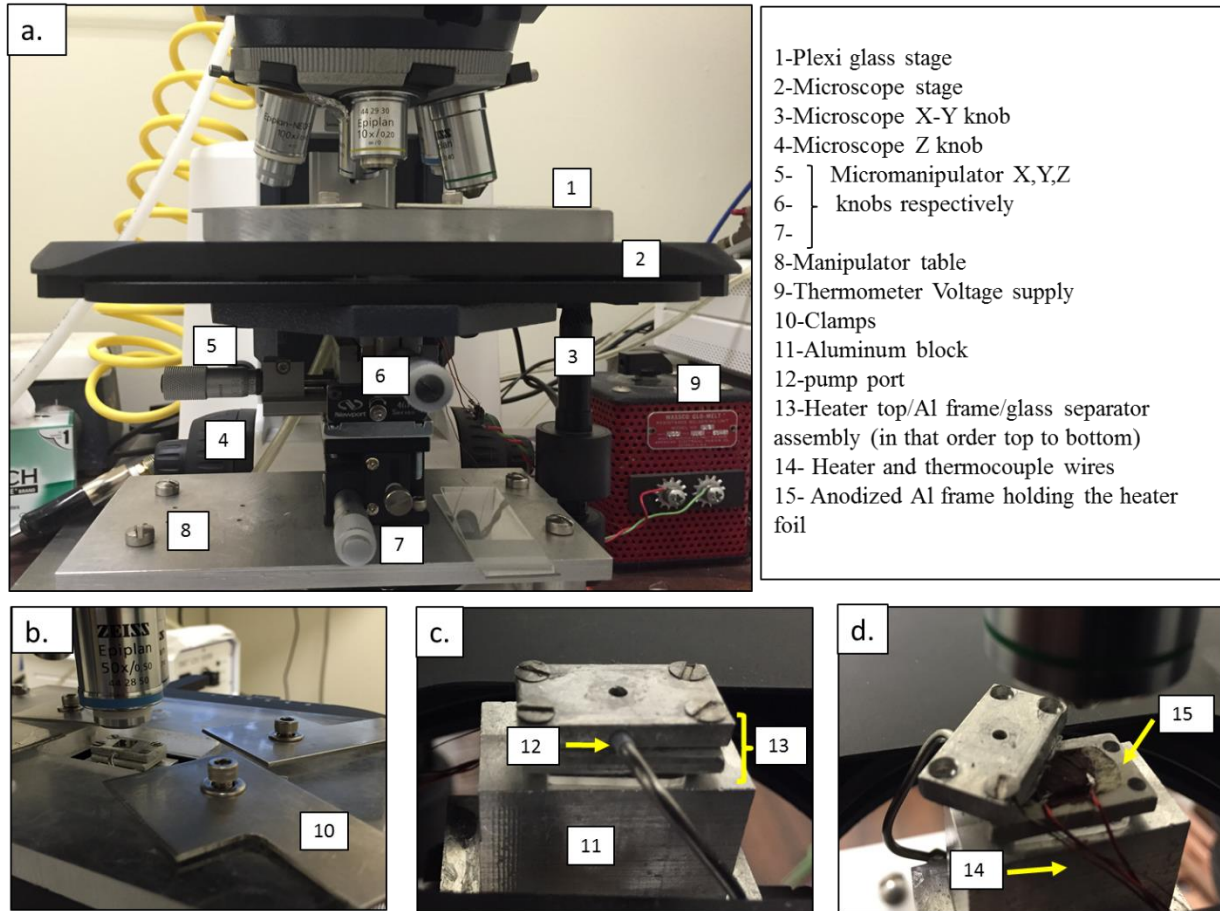
Figure 5.7: **2D materials transfer setup a.** Overall view of the transfer setup with the Newport 420 micromanipulator under Zeiss Axio A1 optical microscope **b.** Stage of the source substrate with clamps to hold the glass slide. **c.** Heater stage and assembly for target substrate **d.** Heater assembly dismantled to show some of the inner components (Upper right corner shows the key for the numerical labeling of the major components of the setup).

C. Transfer procedure

Once a suitable flake is identified by using differential image contrast and color extraction software the target Si/SiO$_2$ substrate is loaded on the heater substrate and held in place by suction (figure 5.8(a)). The source glass slide-substrate is then loaded on the plexi-glass platform located on the microscope stage (with the MMA/PDMS facing down) and clamped firmly. Next both the flake positions are identified and outlined on the computer screen. Then using the micromanipulator knobs both flakes are independently brought to focus and aligned on top of each other using the X-Y knobs. This alignment should be verified by bringing the source and target substrate close to each other but without touching (to eliminate shifts due to refraction). Next weights are added to the plexi-glass platform to hold down its unhinged side during the transfer. Once everything is set and the alignments are verified, constantly observing through the microscope, the graphene flake is slowly pressed down on the h-BN flake. The temperature of the stage is then slowly increased to 120^0C. The polymer layer slowly wets the SiO$_2$ substrate. Once the substrate is completely and uniformly covered with the MMA polymer, the heater is completely turned off and the glass slide is lifted up. In some cases, if the suction is not strong enough, the target substrate gets stuck to the tape/PDMS and is lifted up with the glass slide (figure 5.8(d)). To separate the SiO$_2$ substrate, the connected source+ target substrate is placed on a hot plate at 120^0C. It is then is carefully carved out and separated using a razor blade. Eventually the substrate gets detached with the polymer layer completely transferred onto the target substrate.
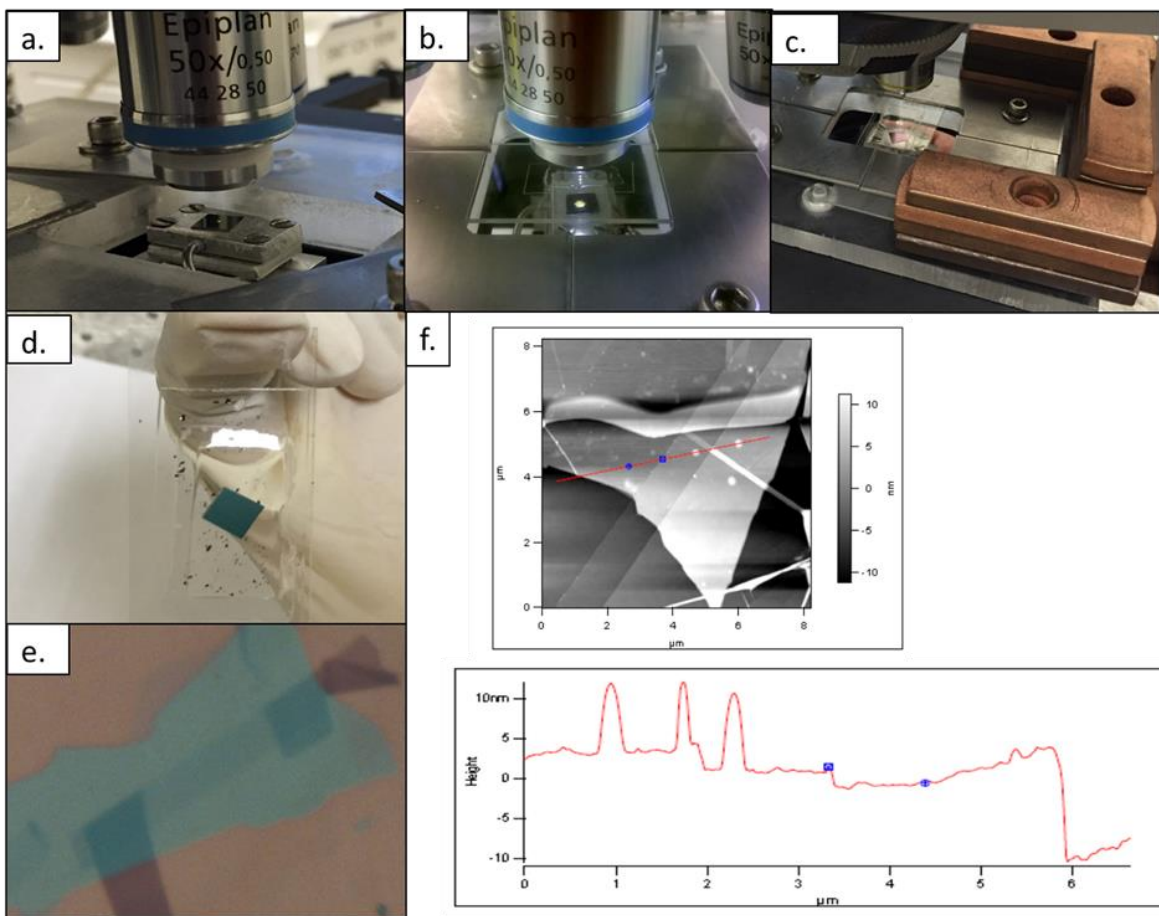
Figure 5.8: Transfer procedure a. positioning of the target substrate on heater stage **b.** aligning of the source substrate (clamped glass slide) with graphene/MMA/tape/PDMS to the h-BN target substrate on the heater stage. **c.** Transfer of graphene on h-BN flake. The copper pieces are weights to hold down the plexi-glass stage during transfer. **d.** After transfer: SiO_2 substrate stuck to the MMA on the tape/PDMS. **e.** Optical image of a completed transfer. **f.** AFM image and height plot of a transferred mono-bilayer graphene on h-BN. Air and impurity bubbles, ~10nm in height, trapped between graphene and BN are also seen. The region indicated between the blue dots indicate a monolayer graphene ~ 1 nm.

D. Post transfer

After transfer the MMA is dissolved in multiple acetone baths for 20 minutes and then checked with optical microscope and AFM (figure 5.8(e) and (f) respectively). After this the sample is thermally annealed for 3-5 hours in a Thermo Scientific CVD furnace at 350^0C in a 1 inch quartz tube with Ar and H_2 (3:1) by volume and again checked under AFM. An area which is

flat and free of trapped bubbles is chosen for sample design and the rest is etched away by using a plasma etcher.

E. Plasma etching

For plasma etching the h-BN/Graphene sample is spin coated with 200 nm of PMMA resist and the region to be etched away is exposed using EBL to create an etch mask. After developing the sample is exposed to RIE Oxygen (flow rate is 5 standard cubic centimeter per minute) in a RF plasma etcher at a power of 19W for 1min. The etch rate for the above parameters is ~ 1 layer graphene/15 s.

F. Metal deposition for contacts on graphene on BN

Sample leads are defined by EBL and developed in acetone and cold water: IPA (1:3). E-beam evaporated titanium (5nm) and gold (35nm) form the contacts. After this again the sample is annealed, as before, in Ar/H_2 gas for 3 hours.

5.5. Experiment for demonstrating Klein collimation

With size limitation no longer a limiting factor in ballistic graphene/BN devices, by designing heterostructures using local gates of different geometries, it is possible to use Klein collimation to spatially guide ballistic electrons in 2D. A schematic of one such device used in this work is shown in figure 5.9 (a). The device fabrication and the key idea is explained below.

A single layer graphene flake transferred on h-BN (~12nm) is plasma etched to a T shape and each of the three branches of the 'T' is placed with Ti/Au contacts such that two of the branches are equal in length. The width (1µm) is the same for all branches. A second EBL (Figure 5.9 (b) left) is used to fabricate a local right angled triangular contactless top gate (TG) which 'entirely' hovers over just the branches of equal length. The triangular top gate is supported by three legs with an arch like structure. This is achieved by fine control of the dose with the double resist method. The fabrication combines all techniques and methods as explained in the previous sections. The hypotenuse of the triangle faces lead 1 while the right angled sides are suspended perpendicular to the other two equal-length branches with the leads 2 and 3. The angle of the vertex between 2 and 3 is ~ 30^0. The 'global' back gate (BG) is the Si substrate with SiO_2/BN dielectric.

By appropriately tuning the BG and TG a *pn, nn or pp* junction can be created. Since normal incident electrons on a *pn* interface are filtered through by Klein tunneling, when current is injected through lead 1, more current is expected to flow into drain lead 3 than through drain lead 2 as illustrated in the figure 5.9 (a). The SEM image of the device -top view and tilted view is shown in figure 5.9 (c) and (d) respectively.
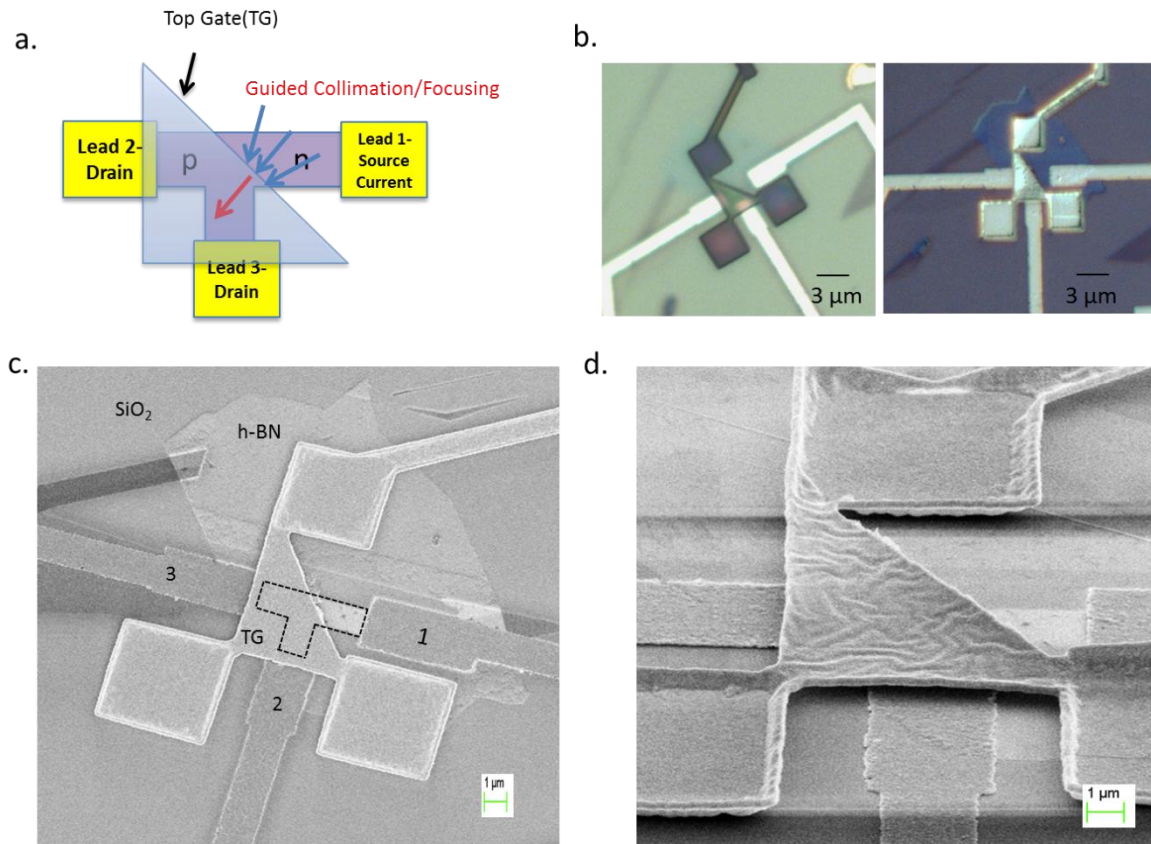

Figure 5.9: Device for testing Klein collimation a. An illustration depicting the idea- current (blue arrows) being collimated into lead 3 (red arrow) through the triangular TG. **b.** Optical image of the device after (left) EBL definition of the gate. The TG region is only covered with PMMA while the green outside region is PMMA and MMA.(right) device after metal deposition. **c.** SEM image of the device. The T shaped graphene is outlined by dotted line. **d.** SEM image, tilted view showing the suspended TG over graphene.

The sample is measured in a He Dewar at 4.2 K with an insert equipped with RC filters and room temperature pi filters. Two terminal gating curves of two sections of the T channel

labelled as *R-Long* with leads 1 ,3 (with 3- grounded and 2-free) and *R-L* with leads 1,2(with 2-grounded and 3-free) are measured separately and is shown in figure 5.10 (a). .Although the two sections are of equal length there is a difference in the resistance. This might be due to differences in the contact resistance or charge scatterers in the two sections. The mobility of each section is around 30,000 cm^2/Vs and l_m ~90nm. Based on the resist thickness, the air-separation between TG and the graphene~ 150 nm. However, the simulation using COMSOL in figure 5.10(b) shows that D~ 150nm which is longer than l_m. So the *pn* junction is diffusive to observe the desired collimation effect.
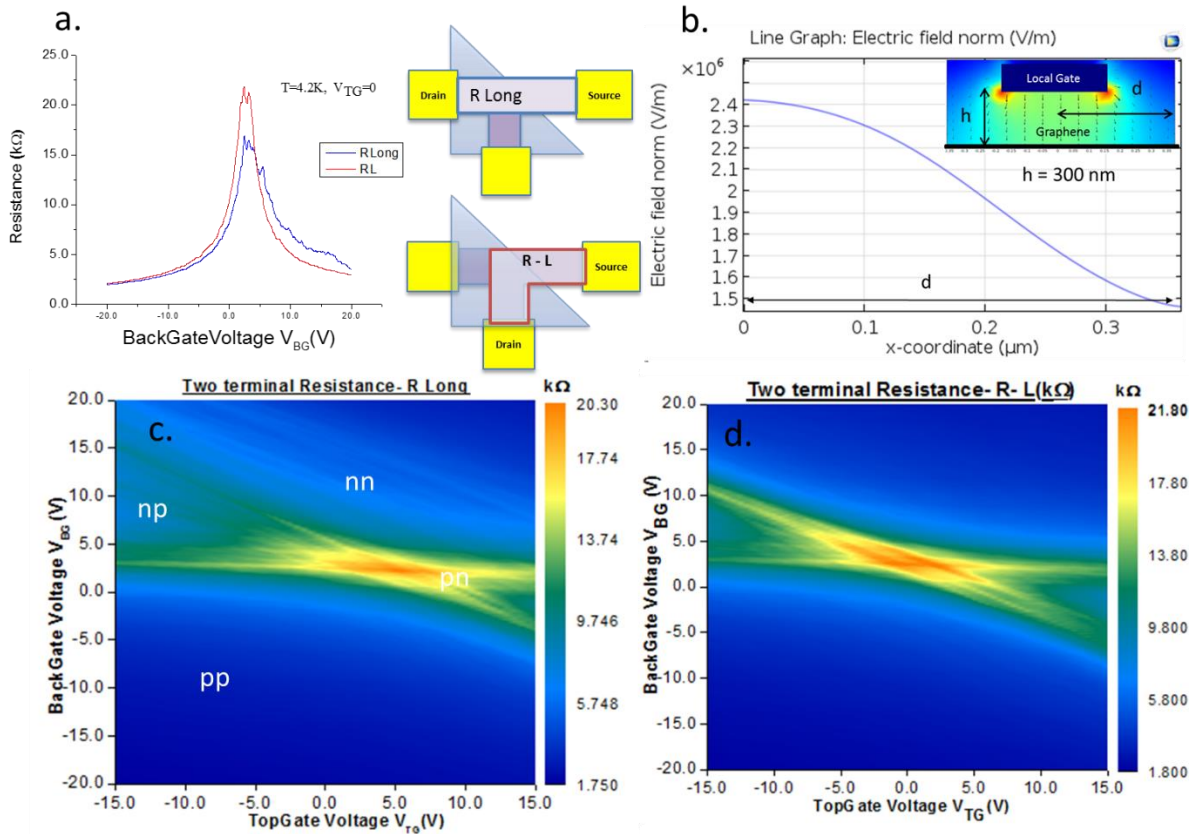
Figure 5. 10: Device characteristics a. Gating curves – two terminal resistance vs V_{BG} and V_{TG} =0 at 4.2K of the two sections of the graphene channel R-Long and R-L shown on the right. **b.** COMSOL simulation depicting the electric field spatial profile for V_{TG} =2V. **c, d.** Two terminal resistance as a function of top and back gate voltages for R-Long and R-L respectively. The four quadrants indicating carrier type outside and underneath the TG are labeled in (b).

The measurements of R-Long and R-L vs top gate voltage (V_{TG}) and back gate voltage (V_{BG}) are shown in figure 5.10 (c) and (d). The ridges on the 2D plot trace out the Dirac peaks and form the outlines of the quadrant representing *nn,np,pn* and *pp*. From the slope of the diagonal ridge, the ratio of the TG capacitance to the BG capacitance $\frac{C_{TG}}{C_{BG}} = 0.603$ for R-Long and 0.533 for R-L. The suspended triangular TG is not perfectly flat and can account for these unequal values. Similarly, V_{TG} at the intersection point of the ridges, corresponding to *p=n=0*, is also different: $V_{TG}= 5V$ for R-Long and $V_{TG}= 0V$ for R-L.

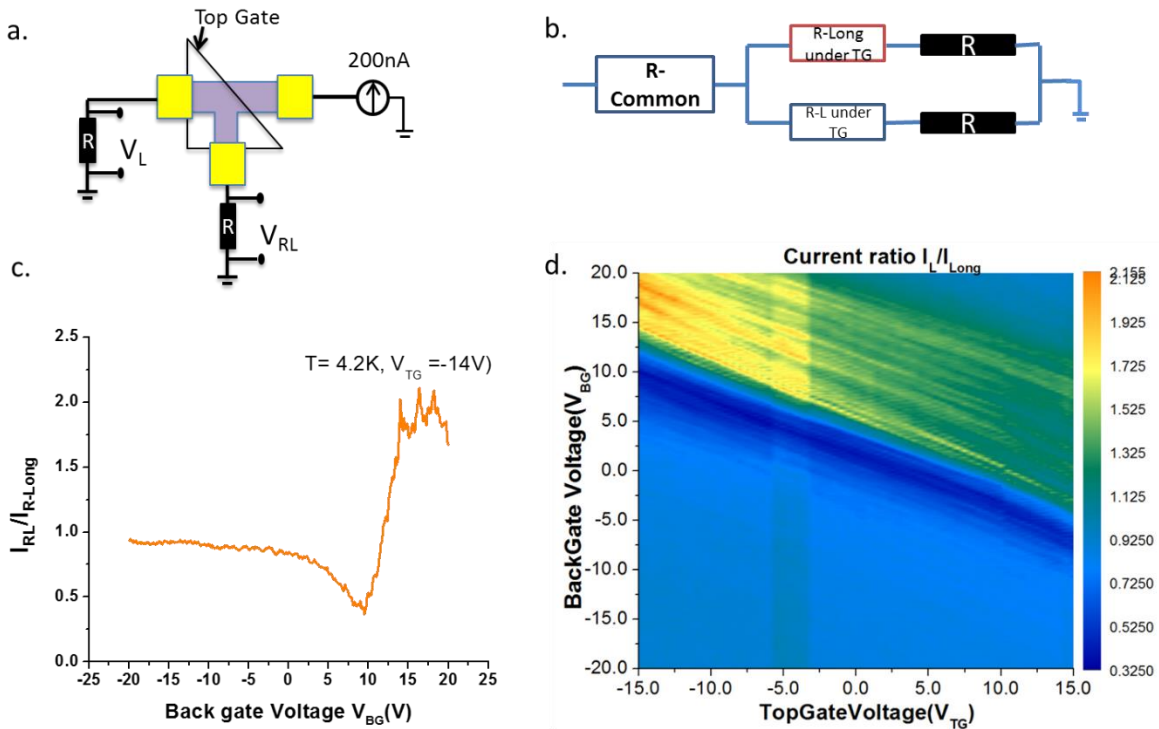**Figure 5. 11: Measurements for current splitting and Klein collimation: a.** Illustration of the measurement setup. **b.** A simple circuit model for the experiment setup shown in (a). **c.** the current ratio I_L/I_{Long} for $V_{TG} = -14V$ where both arms of the T are in the bipolar regime **c.** 2D plot of I_L/I_{Long} as a function of both V_{TG} and V_{BG}.
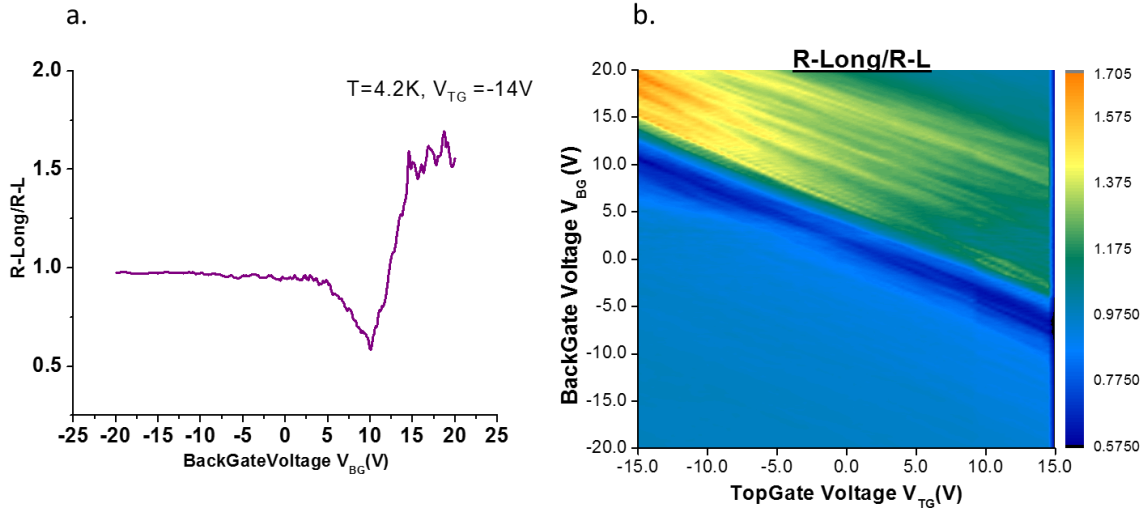
Figure 5. 12: Ratio of resistance of the two sections "Long" and "L" (R-Long/R-L) from measurements in figure 5.10 a. for $V_{TG} = -14V$ where both arms of the T are in the bipolar regime. **b.** 2D plot as a function of (V_{TG}, V_{BG}).

The measurement setup to test for the splitting of current is illustrated in figure 5.11(a) and a simple circuit model for the setup is shown in figure 5.11 (c). The current is injected to lead 1 and leads 2 and 3 are connected in series, with a resistance $R = 1.5k\Omega$. In this case terminals 2 and 3 are both grounded. By tuning V_{TG} and V_{BG}, the voltage drop across R is measured and hence the current in each branch is known. A noticeable difference is expected in the current ratios in the bipolar (*pn)* quadrant if collimation takes place. The ratio of I_L/I_{Long} vs. V_{BG} for $V_{TG}=-14V$, which is in this bipolar quadrant, is shown in figure 5.11(c) and a 2D plot of the ratio as a function of both V_{BG} and V_{TG} is shown in figure 5.11 (d). These plots do not show any sign of current being collimated and only reflect the asymmetry of the unipolar regimes *pp* and *nn*. To verify this further, the ratio of independently measured R-Long and R-L was computed from data shown in figure 5.10. The result is shown in Figure 5.12 (a) for the same fixed $V_{TG}=-14V$ and the 2D plot in figure 5.12 (b). Irrespective of the gate voltages, both plots are almost identical. This suggests that there is no discernible splitting of the current due to Klein tunneling.

The results of the experiment is due to the diffusive nature of the charge carriers in the junction and the device. The circuit model considered although very simple is sufficient to explain

the observations. More accurate analysis should consider the geometry of the sections R-L and R-Long and use the method similar to [97] for extracting the junction resistance .

5.6. Other approaches to fabrication and future work

With improved fabrication techniques, other approaches to study this phenomena were initiated. One way is to use a multilayer BN/Graphene stack and use thin flat graphite flakes as gates. For a heterojunction the graphite gate is split with a separation between the gates ~ 20 nm. For a sharper potential, thin h-BN flake 5-12nm in thickness is used as the gate dielectric (Figure 5.13(c)).

Ionic liquid has been used in studying transport properties in graphene, especially in the high carrier density regime. The liquid can form an electric double layer of about 1nm in thickness at the liquid-graphene interface creating a high large gate capacitance [109, 110]. If the liquid can be confined to create a local gate a sharp potential barrier can be made. This idea motivated fabrication of devices as shown in figure 5.13 (a) and (b).
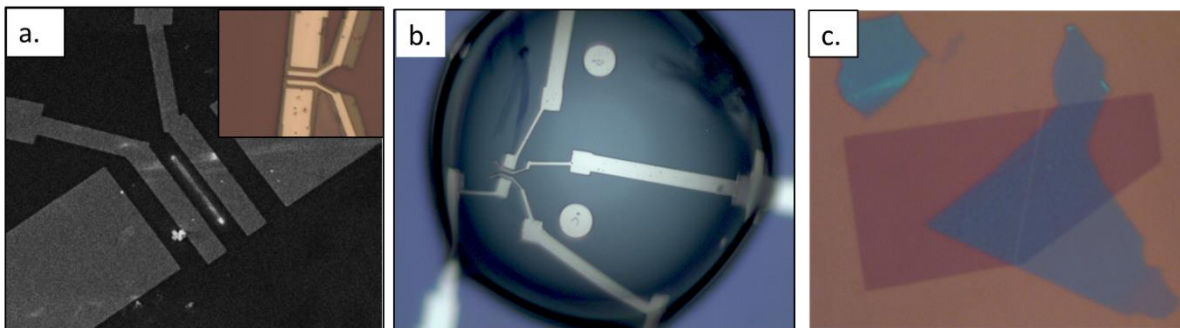
Figure 5. 13 : Other possible fabrication approaches for graphene heterostructures - using ionic liquid and split gates a. SEM image of the device with SiO_2 coating defined with a slit opening ~ 140 nm (the bright line between the voltage leads) in the center of graphene channel.(Inset) optical image of the device. The light yellowish feature is the SiO_2 coating. **b.** Ionic liquid on the device on (a). **c.** Graphite split gate with a 12 nm thick h-BN on top. Split opening ~ 20 nm.

The device is made by coating a four terminal device graphene on SiO_2/Si substrate by a thin insulating layer of SiO_2 (~100nm) except at a slit opening 20 nm wide that runs crosses the center of the channel. Then a small drop of ionic liquid (1-Ethyl-3-methylimidazolium bis(trifluoromethylsulfonyl)imide, 99% [EMIIm] by STREM chemicals) is applied near the graphene area so that it slips into the slit. A gate voltage is applied using a gold wire inserted in the drop. The electric double layer is formed - one near the gate wire and the other directly on the graphene/liquid interface within the slit. The resultant high electric field in a small region provides a sharp barrier for Klein tunneling. A few limitations of this method are as follows. The gate ramp should be done at room temperature as the charge in the ionic liquid becomes frozen at low temperatures. Also the ionic liquid spreads outside the slit and on top of the deposited SiO_2. So a weaker field will also change the carrier density of the graphene sheet outside the slit. Even if the electric field strength is stronger within the slit, the range for independent tuning of the local carrier density is slightly limited.

Using the transfer techniques and the double resist method fabrication described in section 5.4, suspended graphene heterostructures can also be fabricated by a bottom gate instead of the contactless top gate. The bottom local gate is predefined on the substrate before transfer. The SiO_2/Si serve as the global back gate. The sample can also be made with superconducting contacts. Figure shows a pseudo 4-terminal suspended graphene heterostructure with NbN contacts. These devices can be used to study, not only Klein tunneling phenomena, but also for studying superconducting or Josephson effects coupled to Nano mechanical resonators [111].
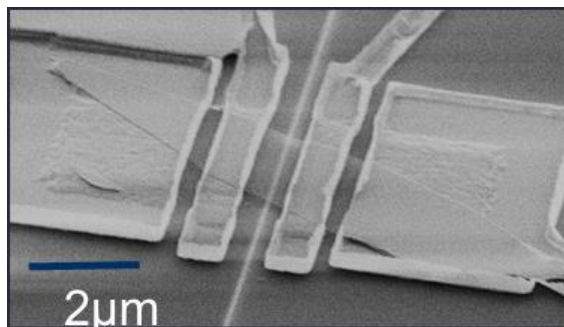

Figure 5. 14: Pseudo four terminal suspended graphene with superconducting NbN contacts over a ~70 nm thin local back gate.

More improvements in the above fabrication methods are likely in the future especially with the advent of new transfer methods for 2D materials such as the 'pickup technique' in [50] and the ability to make high quality 1-D contacts on graphene. Once fabrication of high quality large scale devices with l_m~ size of the sample becomes efficient, an important issue that has to be addressed in measurements is the effect of scattering from finite boundaries of the graphene strip and diffusive contacts on the trajectory of the ballistic electrons. Addressing these issues is crucial for demonstrating the Veselago lensing effect[28]. Use of point contacts for the source and drain and potential barriers at the boundaries of the graphene sheet are some of the things that could be tried out in future experiments.

Bibliography

[1] K.S. Novoselov, A.K. Geim, S.V. Morozov, D. Jiang, Y. Zhang, S.V. Dubonos, I.V. Grigorieva, A.A. Firsov, Electric field effect in atomically thin carbon films, Science (New York, N.Y.), 306 (2004) 666-669.

[2] K.S. Novoselov, A.K. Geim, S.V. Morozov, D. Jiang, M.I. Katsnelson, I.V. Grigorieva, S.V. Dubonos, A.A. Firsov, Two-dimensional gas of massless Dirac fermions in graphene, Nature, 438 (2005) 197-200.

[3] F. Bonaccorso, Z. Sun, T. Hasan, A.C. Ferrari, Graphene photonics and optoelectronics, Nat Photonics, 4 (2010) 611-622.

[4] R. Raccichini, A. Varzi, S. Passerini, B. Scrosati, The role of graphene for electrochemical energy storage, Nature Materials, 14 (2015) 271-279.

[5] W.C. Ren, H.M. Cheng, The global growth of graphene, Nature Nanotechnology, 9 (2014) 726-730.

[6] K. Yang, S.A. Zhang, G.X. Zhang, X.M. Sun, S.T. Lee, Z.A. Liu, Graphene in Mice: Ultrahigh In Vivo Tumor Uptake and Efficient Photothermal Therapy, Nano Letters, 10 (2010) 3318-3323.

[7] N. Mohanty, V. Berry, Graphene-Based Single-Bacterium Resolution Biodevice and DNA Transistor: Interfacing Graphene Derivatives with Nanoscale and Microscale Biocomponents, Nano Letters, 8 (2008) 4469-4476.

[8] K. Roy, M. Padmanabhan, S. Goswami, T.P. Sai, G. Ramalingam, S. Raghavan, A. Ghosh, Graphene-MoS2 hybrid structures for multifunctional photoresponsive memory devices, Nature Nanotechnology, 8 (2013) 826-830.

[9] W.J. Zhang, C.P. Chuu, J.K. Huang, C.H. Chen, M.L. Tsai, Y.H. Chang, C.T. Liang, Y.Z. Chen, Y.L. Chueh, J.H. He, M.Y. Chou, L.J. Li, Ultrahigh-Gain Photodetectors Based on Atomically Thin Graphene-MoS2 Heterostructures, Sci Rep-Uk, 4 (2014).

[10] T. Georgiou, R. Jalil, B.D. Belle, L. Britnell, R.V. Gorbachev, S.V. Morozov, Y.J. Kim, A. Gholinia, S.J. Haigh, O. Makarovsky, L. Eaves, L.A. Ponomarenko, A.K. Geim, K.S. Novoselov, A. Mishchenko, Vertical field-effect transistor based on graphene-WS2 heterostructures for flexible and transparent electronics, Nature Nanotechnology, 8 (2013) 100-103.

[11] K.I. Bolotin, K.J. Sikes, Z. Jiang, M. Klima, G. Fudenberg, J. Hone, P. Kim, H.L. Stormer, Ultrahigh electron mobility in suspended graphene, Solid State Communications, 146 (2008) 351-355.

[12] X. Du, I. Skachko, A. Barker, E.Y. Andrei, Approaching ballistic transport in suspended graphene, Nature Nanotechnology, 3 (2008) 491-495.

[13] C. Beenakker, Specular Andreev Reflection in Graphene, Physical Review Letters, 97 (2006) 067007-067007.

[14] A.R. Akhmerov, C.W.J. Beenakker, Pseudodiffusive conduction at the Dirac point of a normal-superconductor junction in graphene, Physical Review B, 75 (2007) 045426.

[15] J.C. Cuevas, A.L. Yeyati, Subharmonic gap structure in short ballistic graphene junctions, Physical Review B, 74 (2006) 180501(R).

[16] D.J. Clarke, J. Alicea, K. Shtengel, Exotic non-Abelian anyons from conventional fractional quantum Hall states, Nat Commun, 4 (2013) 1348.

[17] A.R. Akhmerov, C.W.J. Beenakker, Detection of valley polarization in graphene by a superconducting contact, Physical Review Letters, 98 (2007) 157003.

[18] F. Miao, S. Wijeratne, Y. Zhang, U.C. Coskun, W. Bao, C.N. Lau, Phase-coherent transport in graphene quantum billiards, Science, 317 (2007) 1530-1533.

[19] H.B. Heersche, P. Jarillo-Herrero, J.B. Oostinga, L.M.K. Vandersypen, A.F. Morpurgo, Bipolar supercurrent in graphene, Nature, 446 (2007) 56-59.

[20] X. Du, I. Skachko, E.Y. Andrei, Josephson current and multiple Andreev reflections in graphene SNS junctions, Physical Review B, 77 (2008) 184507.

[21] H.B. Heersche, P. Jarillo-Herrero, J.B. Oostinga, L.M.K. Vandersypen, A.F. Morpurgo, Induced superconductivity in graphene, Solid State Communications, 143 (2007) 72-76.

[22] H. Hoppe, U. Zulicke, G. Schon, Andreev reflection in strong magnetic fields, Physical Review Letters, 84 (2000) 1804-1807.

[23] V.E. Calado, S. Goswami, G. Nanda, M. Diez, A.R. Akhmerov, K. Watanabe, T. Taniguchi, T.M. Klapwijk, L.M.K. Vandersypen, Ballistic Josephson junctions in edge-contacted graphene, in: arXiv:1501.06817.

[24] M. Ben Shalom, M.J. Zhu, V.I. Fal'ko, A. Mishchenko, A.V. Kretinin, K.S. Novoselov, C.R. Woods, K. Watanabe, T. Taniguchi, A.K. Geim, J.R. Prance, Proximity superconductivity in ballistic graphene, from Fabry-Perot oscillations to random Andreev states in magnetic field, in: arXiv:1504.03286.

[25] M.I. Katsnelson, K.S. Novoselov, A.K. Geim, Chiral tunnelling and the Klein paradox in graphene, Nature Physics, 2 (2006) 620-625.

[26] O. Klein, The reflection of electrons at a potential jump to the relative dynamics of Dirac, Z Phys, 53 (1929) 157-165.

[27] V.G. Veselago, E.E. Narimanov, The left hand of brightness: past, present and future of negative index materials, Nature Materials, 5 (2006) 759-762.

[28] V.V. Cheianov, V. Fal'ko, B.L. Altshuler, The focusing of electron flow and a Veselago lens in graphene p-n junctions, Science, 315 (2007) 1252-1255.

[29] C.R. Dean, A.F. Young, I. Meric, C. Lee, L. Wang, S. Sorgenfrei, K. Watanabe, T. Taniguchi, P. Kim, K.L. Shepard, J. Hone, Boron nitride substrates for high-quality graphene electronics, Nature Nanotechnology, 5 (2010) 722-726.

[30] A.H. Castro Neto, N.M.R. Peres, K.S. Novoselov, A.K. Geim, F. Guinea, The electronic properties of graphene, Reviews of Modern Physics, 81 (2009) 109-162.

[31] S. Das Sarma, S. Adam, E.H. Hwang, E. Rossi, Electronic transport in two-dimensional graphene, Reviews of Modern Physics, 83 (2011) 407-470.

[32] C.W.J. Beenakker, Colloquium: Andreev reflection and Klein tunneling in graphene, Reviews of Modern Physics, 80 (2008) 1337-1354.

[33] T.M. Klapwijk, Proximity effect from an Andreev perspective, J Supercond, 17 (2004) 593-611.

[34] Graphene Brillouin Zone and Electronic Energy Dispersion" from the Wolfram Demonstrations Project
http://demonstrations.wolfram.com/GrapheneBrillouinZoneAndElectronicEnergyDispersion/.

[35] P.A.M. Dirac, The quantum theory of the electron, P R Soc Lond a-Conta, 117 (1928) 610-624.

[36] S.V. Morozov, K.S. Novoselov, M.I. Katsnelson, F. Schedin, L.A. Ponomarenko, D. Jiang, A.K. Geim, Strong suppression of weak localization in graphene, Physical Review Letters, 97 (2006) 016801.

[37] X.S. Wu, X.B. Li, Z.M. Song, C. Berger, W.A. de Heer, Weak antilocalization in epitaxial graphene: Evidence for chiral electrons, Physical Review Letters, 98 (2007) 136801.

[38] F.V. Tikhonenko, A.A. Kozikov, A.K. Savchenko, R.V. Gorbachev, Transition between Electron Localization and Antilocalization in Graphene, Physical Review Letters, 103 (2009) 226801.

[39] T. Low, S. Hong, J. Appenzeller, S. Datta, M.S. Lundstrom, Conductance Asymmetry of Graphene p-n Junction, Ieee T Electron Dev, 56 (2009) 1292-1299.

[40] J. Martin, N. Akerman, G. Ulbricht, T. Lohmann, J.H. Smet, K. Von Klitzing, A. Yacoby, Observation of electron-hole puddles in graphene using a scanning single-electron transistor, Nature Physics, 4 (2008) 144-148.

[41] Y.B. Zhang, V.W. Brar, C. Girit, A. Zettl, M.F. Crommie, Origin of spatial charge inhomogeneity in graphene, Nature Physics, 5 (2009) 722-726.

[42] T. Ando, Screening effect and impurity scattering in monolayer graphene, J Phys Soc Jpn, 75 (2006) 074716

[43] K. Nomura, A.H. MacDonald, Quantum Hall ferromagnetism in graphene, Physical Review Letters, 96 (2006) 256602.

[44] E.H. Hwang, S. Adam, S. Das Sarma, Carrier transport in two-dimensional graphene layers, Physical Review Letters, 98 (2007) 186806.

[45] K.S. Novoselov, Z. Jiang, Y. Zhang, S.V. Morozov, H.L. Stormer, U. Zeitler, J.C. Maan, G.S. Boebinger, P. Kim, A.K. Geim, Room-temperature quantum hall effect in graphene, Science, 315 (2007) 1379-1379.

[46] Y.B. Zhang, Y.W. Tan, H.L. Stormer, P. Kim, Experimental observation of the quantum Hall effect and Berry's phase in graphene, Nature, 438 (2005) 201-204.

[47] F. Guinea, M.I. Katsnelson, M.A.H. Vozmediano, Midgap states and charge inhomogeneities in corrugated graphene, Physical Review B, 77 (2008) 075422.

[48] A. Deshpande, W. Bao, F. Miao, C.N. Lau, B.J. LeRoy, Spatially resolved spectroscopy of monolayer graphene on SiO2, Physical Review B, 79 (2009) 205411.

[49] Y.J. Kang, J. Kang, K.J. Chang, Electronic structure of graphene and doping effect on SiO(2), Physical Review B, 78 (2008) 115404.

[50] L. Wang, I. Meric, P.Y. Huang, Q. Gao, Y. Gao, H. Tran, T. Taniguchi, K. Watanabe, L.M. Campos, D.a. Muller, J. Guo, P. Kim, J. Hone, K.L. Shepard, C.R. Dean, One-dimensional electrical contact to a two-dimensional material, Science (New York, N.Y.), 342 (2013) 614-617.

[51] V.P. Gusynin, S.G. Sharapov, Unconventional integer quantum Hall effect in graphene, Physical Review Letters, 95 (2005) 146801.

[52] X. Du, I. Skachko, F. Duerr, A. Luican, E.Y. Andrei, Fractional quantum Hall effect and insulating phase of Dirac electrons in graphene, Nature, 462 (2009) 192-195.

[53] K.I. Bolotin, F. Ghahari, M.D. Shulman, H.L. Stormer, P. Kim, Observation of the fractional quantum Hall effect in graphene, Nature, 462 (2009) 196-199.

[54] E.Y. Andrei, G.H. Li, X. Du, Electronic properties of graphene: a perspective from scanning tunneling microscopy and magnetotransport, Rep Prog Phys, 75 (2012) 056501.

[55] P.-G.d. Gennes, Superconductivity of metals and alloys, Addison-Wesley, Redwood City, CA, 1989.

[56] G.E. Blonder, M. Tinkham, T.M. Klapwijk, Transition from Metallic to Tunneling Regimes in Superconducting Micro-Constrictions - Excess Current, Charge Imbalance, and Super-Current Conversion, Physical Review B, 25 (1982) 4515-4532.

[57] K. Flensberg, J.B. Hansen, M. Octavio, Subharmonic Energy-Gap Structure in Superconducting Weak Links, Physical Review B, 38 (1988) 8707-8711.

[58] C.W.J. Beenakker, Andreev reflection and Klein tunneling in graphene, (2007) 1-20.

[59] N.N. Iosad, B.D. Jackson, S.N. Polyakov, P.N. Dmitriev, T.M. Klapwijk, Reactive magnetron sputter-deposition of NbN and (Nb,Ti)N films related to sputtering source characterization and optimization, J Vac Sci Technol A, 19 (2001) 1840-1845.

[60] J. Moser, A. Barreiro, A. Bachtold, Current-induced cleaning of graphene, Applied Physics Letters, 91 (2007) 163513

[61] M.I. Katsnelson, Zitterbewegung, chirality, and minimal conductivity in graphene, Eur Phys J B, 51 (2006) 157-160.

[62] S.R. Zandbergen, M.J.A. de Dood, Experimental Observation of Strong Edge Effects on the Pseudodiffusive Transport of Light in Photonic Graphene, Physical Review Letters, 104 (2010) 043903.

[63] X.D. Zhang, Observing zitterbewegung for photons near the dirac point of a two-dimensional photonic crystal, Physical Review Letters, 100 (2008) 113903.

[64] J. Tworzydlo, B. Trauzettel, M. Titov, A. Rycerz, C.W.J. Beenakker, Sub-Poissonian shot noise in graphene, Physical Review Letters, 96 (2006) 246802.

[65] M. Titov, C.W.J. Beenakker, Josephson effect in ballistic graphene, Physical Review B, 74 (2006) 041401(R).

[66] E. Scheer, P. Joyez, D. Esteve, C. Urbina, M.H. Devoret, Conduction channel transmissions of atomic-size aluminum contacts, Physical Review Letters, 78 (1997) 3535-3538.

[67] L. DiCarlo, J.R. Williams, Y.M. Zhang, D.T. McClure, C.M. Marcus, Shot noise in graphene, Physical Review Letters, 100 (2008) 156801.

[68] R. Danneau, F. Wu, M.F. Craciun, S. Russo, M.Y. Tomi, J. Salmilehto, A.F. Morpurgo, P.J. Hakonen, Shot noise in ballistic graphene, Physical Review Letters, 100 (2008) 196802.

[69] L. Wang, I. Meric, P.Y. Huang, Q. Gao, Y. Gao, H. Tran, T. Taniguchi, K. Watanabe, L.M. Campos, D.a. Muller, J. Guo, P. Kim, J. Hone, K.L. Shepard, C.R. Dean, One-dimensional electrical contact to a two-dimensional material, Science (New York, N.Y.), 342 (2013) 614-617.

[70] N. Mizuno, B. Nielsen, X. Du, Ballistic-like supercurrent in suspended graphene Josephson weak links, Nat Commun, 4 (2013) 2716.

[71] V. Mourik, K. Zuo, S.M. Frolov, S.R. Plissard, E.P.A.M. Bakkers, L.P. Kouwenhoven, Signatures of Majorana Fermions in Hybrid Superconductor-Semiconductor Nanowire Devices, Science, 336 (2012) 1003-1007.

[72] A. Das, Y. Ronen, Y. Most, Y. Oreg, M. Heiblum, H. Shtrikman, Zero-bias peaks and splitting in an Al-InAs nanowire topological superconductor as a signature of Majorana fermions, Nature Physics, 8 (2012) 887-895.

[73] A. Bardas, D.V. Averin, Electron transport in mesoscopic disordered superconductor-normal-metal-superconductor junctions, Physical Review B, 56 (1997) R8518(R).

[74] D. Averin, A. Bardas, Ac Josephson Effect in a Single Quantum Channel, Physical Review Letters, 75 (1995) 1831-1834.

[75] P. Blake, R. Yang, S.V. Morozov, F. Schedin, L.A. Ponomarenko, A.A. Zhukov, R.R. Nair, I.V. Grigorieva, K.S. Novoselov, A.K. Geim, Influence of metal contacts and charge inhomogeneity on transport properties of graphene near the neutrality point, Solid State Communications, 149 (2009) 1068-1071.

[76] W.R. Hannes, M. Jonson, M. Titov, Electron-hole asymmetry in two-terminal graphene devices, Physical Review B, 84 (2011) 045414.

[77] V. Mourik, K. Zuo, S.M. Frolov, S.R. Plissard, E.P.A.M. Bakkers, L.P. Kouwenhoven, Signatures of Majorana Fermions in Hybrid Superconductor-Semiconductor Nanowire Devices, in, 2012, pp. 1003-1007.

[78] P. Rickhaus, M. Weiss, L. Marot, C. Schonenberger, Quantum Hall Effect in Graphene with Superconducting Electrodes, Nano Letters, 12 (2012) 1942-1945.

[79] Z. Wan, A. Kazakov, M.J. Manfra, L.N. Pfeiffer, K.W. West, L.P. Rokhinson, Induced superconductivity in high-mobility two-dimensional electron gas in gallium arsenide heterostructures, Nat Commun, 6 (2015) 7426.

[80] M. Ben Shalom, M.J. Zhu, V.I. Fal'ko, A. Mishchenko, A.V. Kretinin, K.S. Novoselov, C.R. Woods, K. Watanabe, T. Taniguchi, A.K. Geim, J.R. Prance, Proximity superconductivity in ballistic graphene, from Fabry-Perot oscillations to random Andreev states in magnetic field, in: arXiv:1504.03286, 2015, pp. 3286.

[81] G. Tkachov, V.I. Fal'ko, Magnetic field influence on the proximity effect in semiconductor-superconductor hybrid structures and their thermal conductance, Physical Review B, 69 (2004) 092503.

[82] G. Tkachov, K. Richter, Andreev magnetotransport in low-dimensional proximity structures: Spin-dependent conductance enhancement, Physical Review B, 71 (2005) 094517

[83] F. Rohlfing, G. Tkachov, F. Otto, K. Richter, D. Weiss, G. Borghs, C. Strunk, Doppler shift in Andreev reflection from a moving superconducting condensate in Nb/InAs Josephson junctions, Physical Review B, 80 (2009) 220507

[84] G. Stan, S.B. Field, J.M. Martinis, Critical field for complete vortex expulsion from narrow superconducting strips, Physical Review Letters, 92 (2004) 097003.

[85] M. Popinciuc, V.E. Calado, X.L. Liu, A.R. Akhmerov, T.M. Klapwijk, L.M.K. Vandersypen, Zero-bias conductance peak and Josephson effect in graphene-NbTiN junctions, Physical Review B, 85 (2012) 205404

[86] P.E. Goa, H. Hauglin, M. Baziljevich, E. Il'yashenko, P.L. Gammel, T.H. Johansen, Real-time magneto-optical imaging of vortices in superconducting NbSe2, Supercond Sci Tech, 14 (2001) 729-731.

[87] A.A.F. Olsen, H. Hauglin, T.H. Johansen, P.E. Goa, D. Shantsev, Single vortices observed as they enter NbSe2, Physica C-Superconductivity and Its Applications, 408 (2004) 537-538.

[88] C.P. Bean, Magnetization of High-Field Superconductors, Reviews of Modern Physics, 36 (1964) 31.

[89] W. Chang, S.M. Albrecht, T.S. Jespersen, F. Kuemmeth, P. Krogstrup, J. Nygard, C.M. Marcus, Hard gap in epitaxial semiconductor-superconductor nanowires, Nature Nanotechnology, 10 (2015) 232-236.

[90] C.D. Anderson, The positive electron, Phys Rev, 43 (1933) 491-494.

[91] A. Calogeracos, N. Dombey, History and physics of the Klein paradox, Contemp Phys, 40 (1999) 313-321.

[92] F. Sauter, The behavior of an electron in a homogeneous electric field to the relativistic theory of Dirac, Z Phys, 69 (1931) 742-764.

[93] D.N. Page, Hawking radiation and black hole thermodynamics, New J Phys, 7 (2005) 203

[94] R. Ruffini, G. Vereshchagin, S.S. Xue, Electron-positron pairs in physics and astrophysics: From heavy nuclei to black holes, Phys Rep, 487 (2010) 1-140.

[95] V.V. Cheianov, V.I. Fal'ko, Selective transmission of Dirac electrons and ballistic magnetoresistance of n-p junctions in graphene, Physical Review B, 74 (2006) 041403

[96] M.M. Fogler, D.S. Novikov, L.I. Glazman, B.I. Shklovskii, Effect of disorder on a graphene p-n junction, Physical Review B, 77 (2008) 075420.

[97] B. Huard, J.A. Sulpizio, N. Stander, K. Todd, B. Yang, D. Goldhaber-Gordon, Transport measurements across a tunable potential barrier in graphene, Physical Review Letters, 98 (2007) 236803.

[98] N. Stander, B. Huard, D. Goldhaber-Gordon, Evidence for Klein Tunneling in Graphene p-n Junctions, Physical Review Letters, 102 (2009) 026807.

[99] J.R. Williams, L. DiCarlo, C.M. Marcus, Quantum hall effect in a gate-controlled p-n junction of graphene, Science, 317 (2007) 638-641.

[100] J.R. Williams, C.M. Marcus, Snake States along Graphene p-n Junctions, Physical Review Letters, 107 (2011) 046602.

[101] B. Ozyilmaz, P. Jarillo-Herrero, D. Efetov, D.A. Abanin, L.S. Levitov, P. Kim, Electronic transport and quantum hall effect in bipolar graphene p-n-p junctions, Physical Review Letters, 99 (2007) 166804.

[102] G. Liu, J. Velasco, W.Z. Bao, C.N. Lau, Fabrication of graphene p-n-p junctions with contactless top gates, Applied Physics Letters, 92 (2008) 203103.

[103] R.V. Gorbachev, A.S. Mayorov, A.K. Savchenko, D.W. Horsell, F. Guinea, Conductance of p-n-p structures with "Air-Bridge" top gates, Nano Letters, 8 (2008) 1995-1999.

[104] A.F. Young, P. Kim, Quantum interference and Klein tunnelling in graphene heterojunctions, Nature Physics, 5 (2009) 222-226.

[105] A.V. Shytov, M.S. Rudner, L.S. Levitov, Klein Backscattering and Fabry-Perot Interference in Graphene Heterojunctions, Physical Review Letters, 101 (2008) 156804

[106] F.N. Xia, V. Perebeinos, Y.M. Lin, Y.Q. Wu, P. Avouris, The origins and limits of metal-graphene junction resistance, Nature Nanotechnology, 6 (2011) 179-184.

[107] T. Taychatanapat, K. Watanabe, T. Taniguchi, P. Jarillo-Herrero, Quantum Hall effect and Landau-level crossing of Dirac fermions in trilayer graphene, Nature Physics, 7 (2011) 621-625.

[108] B. Hunt, J.D. Sanchez-Yamagishi, a.F. Young, M. Yankowitz, B.J. LeRoy, K. Watanabe, T. Taniguchi, P. Moon, M. Koshino, P. Jarillo-Herrero, R.C. Ashoori, Massive Dirac fermions and Hofstadter butterfly in a van der Waals heterostructure, Science (New York, N.Y.), 340 (2013) 1427-1430.

[109] D.K. Efetov, P. Kim, Controlling Electron-Phonon Interactions in Graphene at Ultrahigh Carrier Densities, Physical Review Letters, 105 (2010) 256805.

[110] J.T. Ye, M.F. Craciun, M. Koshino, S. Russo, S. Inoue, H.T. Yuan, H. Shimotani, A.F. Morpurgo, Y. Iwasa, Accessing the transport properties of graphene and its multilayers at high carrier density, Proceedings of the National Academy of Sciences of the United States of America, 108 (2011) 13002-13006.

[111] B.H. Schneider, S. Etaki, H.S.J. van der Zant, G.A. Steele, Coupling carbon nanotube mechanics to a superconducting circuit, Sci Rep-Uk, 2 (2012) 599.